INAUGURAL DISSERTATION

zur

Erlangung der Doktorwüde

der

Naturwissenschaftlich–Mathematishen

Gesamtfakultät

der

Ruprecht–Karls–Universität

Heidelberg

Vorgelegt von

Master of Science, Hsiang–Wen Hsu

Aus: Taipei, Taiwan

Tag der mündlichen Prüfung: 23.04.2010

Thema

Dynamics of Jovian and Saturnian Stream Particles

Gutachter: Prof. (apl) Dr. Mario Trieloff

Prof. Dr. Mihály Horányi

Abstract

Stream particles are nanometer-sized dust particles ejected with speeds greater than $100\,\mathrm{km\,s^{-1}}$ from the Jovian and Saturnian system. Due to their tiny size, the dynamics of the charged grains is dominated by electromagnetic forces. The strong correlation between the stream particle flux and the strength of the interplanetary magnetic field (IMF) was observed first by the dust detectors on the Ulysses and Galileo spacecrafts.

The Cosmic Dust Analyser (CDA) onboard the Cassini spacecraft offers the unique opportunity achieve a deeper understanding of the stream particle phenomenon due to the detector's improved sensitivity and its capability to determine the particles' composition. Furthermore, CDA is so far the only detector which observed stream particles from both source planets. The direct comparison between the properties of grains from different source planets provide deep insights into the physics of the dustmagnetosphere interaction. Because the observations of Jovian stream particles by three spacecrafts covers a very long time span, also the long term evolution of the stream particle flux can be studied.

This study finds that the Jovian stream flux in the interplanetary space monitored by CDA during Cassinis flyby at Jupiter in 2000 to 2001 follows a similar trend as the stream particle flux in the inner Jovian system simultaneously observed by the Galileo detector. By employing a plasma model based on the observed ultraviolet emission of Io's plasma torus, it is shown that the charging conditions in the vicinity of Io are consistent with the enhancement of the stream particle production rate derived from Galileo measurements. This finding is indicative of a complex dustmoon-magnetosphere interaction, which has not yet been understood.

An important focus of this work are the Saturnian stream particles discovered by the Cassini dust detector. The dynamical evolution of the particles in the interplanetary space as well as in Saturn's magnetosphere is investigated in depth. During Cassini's approach to Jupiter in 2004 the interplanetary magnetic field showed a recurrent twosector structure associated with Corotation Interaction Regions (CIRs). CDA observations during this period clearly show a drastic change of the particles' dynamical properties

during their passage from solar wind rarefaction regions into compressed, high magnetic field strength solar wind regions. This implies that the dust stream phenomenon stems from "local" stream particle-IMF interactions.

By means of backward tracing simulations using Cassini insitu solar wind data it is shown that Saturnian stream particles have sizes ranging between 2 to 8 nm and are escaping from the Saturnian system at speeds between 50 and $200\,\mathrm{km\,s^{-1}}$. The newly developed ejection model, which includes stochastic charging and employes the latest Cassini plasma data, matches the dynamical properties derived from backward tracing simulations. This allows us to identify the source region of the particles in the inner Saturnian system.

A analysis of CDA mass spectra shows that the grain composition of the source region (water ice in E ring particles) is different from the composition of Saturnian stream particles, which have a drastically enhanced siliceous compound. The pronounced difference between the secondary electron emission yield and the sputtering efficiency of water ice and siliceous material suggests that plasma sputtering not only governs the lifetime of the E ring particles but also provides an compositional selection mechanism responsible for the observed compositional discrepancy between icy E ring grains and Saturnian stream particles. The high sputtering yield of water ice suggest that siliceous impurities released via sputtering from the dynamically evolved E ring particles are the most probable source of Saturnian stream particles. This work also indicates that the radiolysis of icy E ring grains may be responsible for the observed atomic and molecular oxygen ion features in Saturn's magnetosphere.

Zusammenfassung

Stromteilchen sind nanometer-groe Festkörperteilchen, welche mit Geschwindigkeiten > 100 $\mathrm{km\,s^{-1}}$ aus dem Jupiter- und Saturnsystem entweichen. Aufgrund ihrer winzigen Gre wird ihre Dynamik durch elektromagnetische Kräfte beherrscht. Die starke Korrelation zwischen dem Stromteilchenflu und der Stärke des interplanetaren Feldes wurde zuerst von den Staubdetektoren der Ulysses- und Galileo-Misionen beocbachtet.

Der Staubdetektor CDA der Cassini-Sonde bietet aufgrund seiner hohen Empfindlichkeit als auch wegen seiner Fähigkeit, die Zusammensetzung der Staubteilchen zu bestimmen, die einzigartige Möglichkeit, daß Stromteilchenphänomen grundsätzlich zu verstehen. Darüber hinaus ist der CDA der einzige Detektor, welcher Stromteilchen von beiden bisher bekannten planetaren Quellen beobachtet hat. Der direkte Vergleich zwischen den Eigenschaften von Stromteilchen verschiedener Herkunft ermglicht einen tiefen Einblick in die Physik der Staub-Magneotsphären-Wechselwirkung. Da die Beobachtungen von Jupiter-Stromteilchen durch die 3 Detektoren einen sehr langen Zeitraum abdecken, kann auerdem die Langzeitentwicklung des Stromteilchenflusses analysiert werden.

Diese Arbeit zeigt, daß der von CDA im interplanetaren Raum gemessene Fluß von Jupiter-Stromteilchen einen ähnlichen Trend als der von Galileo gleichzeitig im inneren Jupitersystem gemessene Fluß folgt. Es wird mittels eines auf der UV-Emmision des Io-Torus beruhenden Plasmamodells gezeigt, daß die Aufladungsbedingungen in der Nähe Io's mit der Zunahme der aus Galileo-Daten abgeleiteten Stromteilchenproduktion konsistent ist. Dieses Ergebnis weist auf eine bisher unverstandene komplexe Wechselwirkung zwischen Io, den Staubteilchen und der Magnetosphäre hin.

Ein bedeutender Fokus dieser Arbeit sind die durch Cassini entdeckten Saturn-Stromteilchen. Deren dynamische Entwicklung sowohl im interplanetaren Raum als auch innerhalb der Saturn-Magnetosphäre wird detailliert untersucht. Das interplanetare Magnetfeld zeigte während Cassinis Annäherung an den Saturn im Jahre 2004 eine ausgeprägte, mit sogenannten "Corotation Interaction Regions" verbundene 2-Sektor-Struktur. CDA-Beobachtungen während dieses Zeitraums zeigten eine deutliche Veränderung der dynamischen Eigenschaften der Stromteilchen, wenn diese aus einer "rarefaction region" in Gebiete komprimierten Sonnenwindes eindrangen. Dies bedeutet, daß das Stromteilchenphänomen auf lokaleWechselwirkungen zwischen dem interplanetaren Magnetfeld und dem Staub zur-

ckzuführen ist.

Mittels zeitlich inverser (backward tracing), auf Cassini-Sonnenwindaten beruhender Simulationen wird gezeigt, daß Stromteilchen Größen zwischen 2 und 8 nm und Geschwindigkeiten zwischen 50 und $200\,\mathrm{km\,s^{-1}}$ aufweisen. Das neuentwickelte Beschleunigungsmodell, welches Effekte der stochastischen Aufladung berücksichtigt und auf neuesten Cassini-Plasma-daten beruht, reproduziert die aus den zeitlich inversen Simulationen abgeleiteten dynamischen Eigenschaften der Stromteilchen. Dieses Ergebnis ist die Grundlage für die Identifizierung der Stromteilchenquelle im inneren Saturnsystem.

In einer Analyse von CDA Massenspektren wird gezeigt, dass die Partikelzusammensetzung in der Quellregion (Wassereis im E ring) sich von der Zusammensetzung der Saturn Stromteilchen unterscheidet, welche eine drastisch erhoehte silikatische Komponente aufweisen. Die stark unterschiedlichen Sputtereffizienzen und Sekundärelektronenergiebigkeiten von Wassereis und Silikaten indizieren, daß das Plasmasputtering nicht die Lebenszeit der E-Ring-Teilchen bestimmt, sondern auch ein materialselektiver Prozeß ist, welcher für die beobachtete unterschiedliche Zusammensetzung von Ring- und Stromteilchen verantwortlich ist. Die hohe Sputtereffizienz von Wassereis unterstützt die Annahme, daß Saturn-Stromteilchen die durch Plasmaerosion freigesetzten silikatischen Verunreinigungen in den Wassereisteilchen sind. Abschlieend zeigt diese Arbeit, daß die Radiolyse der Wassereisteilchen eine mögliche Erklärung der beobachteten Verteilung von atomaren und molekularen Sauerstoffionen im Saturnsystem ist.

Declaration

I herewith declare that I have produced this paper without the prohibited assistance of third parties and without making use of aids other than those specified; notions taken over directly or indirectly from other sources have been identified as such. This paper has not previously been presented in identical or similar form to any other German or foreign examination board.

<div align="right">

Hsiang–Wen Hsu
12/03/2010
Heidelberg

</div>

Contents

List of Figures

List of Tables

LIST OF TABLES

1

Summary

1.1 Cosmic Dust

Cosmic dust consists of microscopic solid particles floating in space. The terminology of cosmic dust has loose definitions regarding the size range, the structure, and the chemical composition. The size of cosmic dust particles could be as small as a molecular cluster (few nm) or as big as the sand grains you can find at the beach (0.1mm). It could have a complex structure such as a siliceous core with an icy mantle or be simple as a pure water ice grain. Even with naked eyes, various cosmic dust populations can be observed on Earth (figure 1.1).

Being the solid component, the cosmic dust particles behave differently in contrast to the neutral gas and plasma in space environment. Carrying a relatively large momentum, the dynamics of dust particles is distinct from the ambient gas and plasma which results in differential motion and induces different spatial distribution and further interactions between each other. Moreover, the heavy dust particles may also be seen as extensive mass reservoirs and serve as sources of gas/plasma or mediate the energy exchange in the system.

Different categories of cosmic dust can be distinguished according to their locations, such as circumplanetary dust, interplanetary dust, and interstellar dust. Due to different environment conditions, the influences of cosmic dust take place on different temporal and spatial scales. Interstellar dust particles could form from the atmosphere of evolved stars and wander in interstellar space for millions of years while the sputtering lifetime of dust grains in Saturn's magnetosphere is in the order of decades. These temporal and spatial scales decide which processes dominate the shaping mechanism of the size distribution, composition, and dynamical properties of cosmic dust grains and the way they interact with the environment.
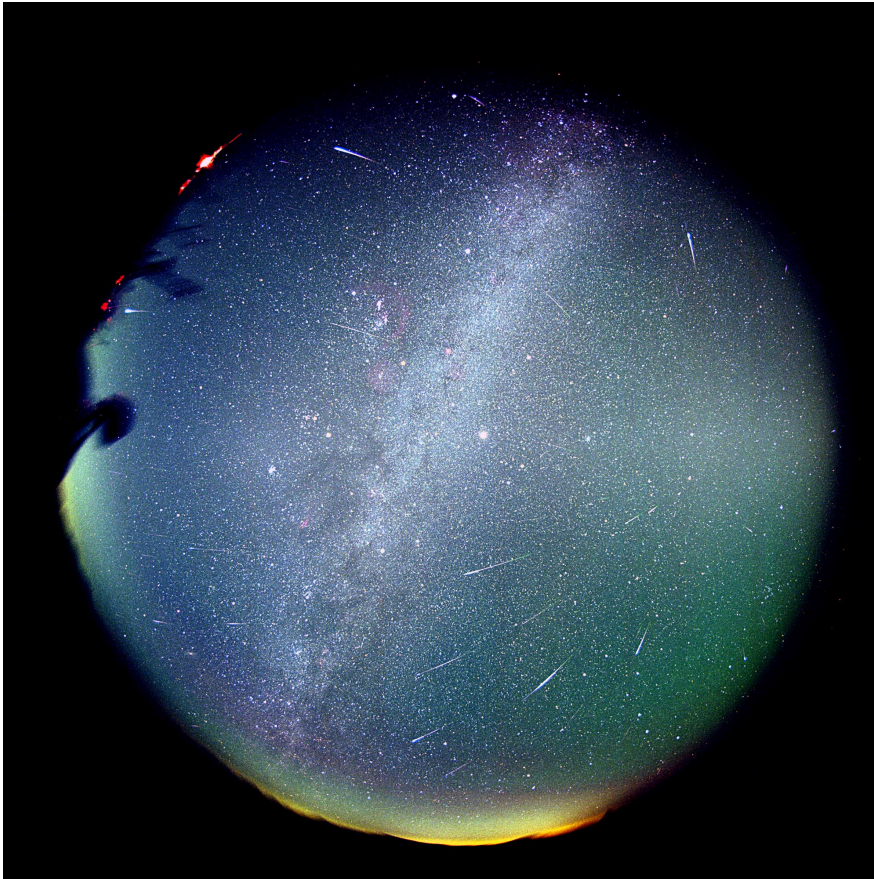
Figure 1.1: Various kinds of cosmic dust can be seen on Earth. - A fish–eye photograph is taken during the famous leonids meteor shower at November 19, 2001 in Taiwan. Various cosmic dust populations were recorded in this image. First, bright tracks of meteors radiating from the constellation Leo were caused by millimeter sized particles which are entering the Earths atmosphere during passage of the dust stream that originates from Comet Tempel-Tuttle.. Second, dark belts across the splendid milky way are dense interstellar dust clouds located in the plane of our Galaxy. At last, a faint fuzzy belt orthogonal to the milky way toward the right of the image is the zodiac light, which is the sunlight reflected by interplanetary dust particles in the inner solar system. Credit & Copyright: Chen, Huang–Ming.

1.1.1   Observation Techniques

Cosmic dust can be detected via in–situ or remote sensing methods. In–situ measurements are performed by dust detectors on board spacecrafts flown to various solar system objects, while remote sensing techniques measure the electromagnetic radiation emitted or scattered from dust particles in distant environments. In addition, dust particles can be collected and sent back to the laboratory for detailed analysis.

Depending on the space environment, several in–situ methods such as penetration detector (Humes *et al.*, 1980, Pioneer 11), optical detection (Colangeli *et al.*, 2007, Rosetta mission), acoustic signal (Takechi *et al.*, 2009, BepiColombo mission), and impact ionization can be employed for dust measurements. Among all, the impact ionization method provides the best mass sensitivity for dust impact speeds larger than $1 \, \mathrm{km \, s^{-1}}$. Dust detectors on board Ulysses, Galileo, and Cassini spacecrafts belong to this type. Figure 1.2 from (Mann *et al.*, 2004) shows the applicable mass/size range of various dust detection methods.
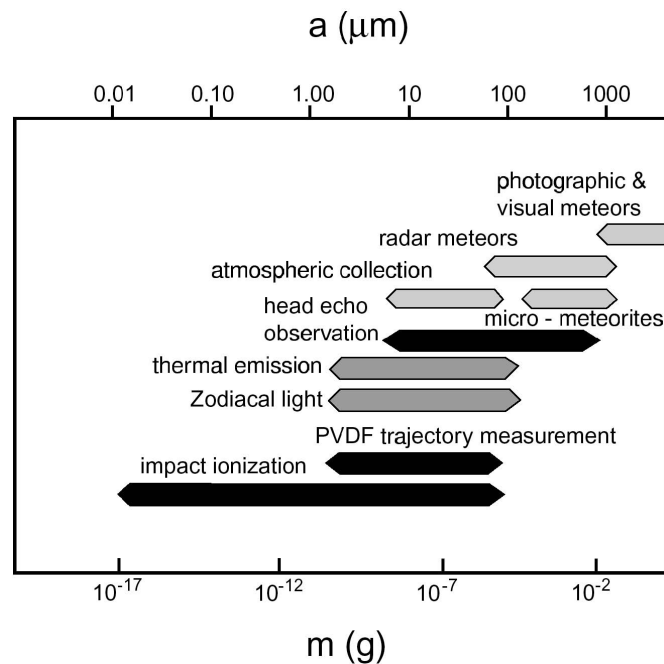
Figure 1.2: Dust detection methods and the applicable size/mass range. - This figure from Mann *et al.* (2004) shows the approximate mass and corresponding size range of cosmic dust particles suited for various in–situ and remote sensing dust detection methods.

For astronomical objects located far away, measuring the electromagnetic radiation from dust particles provides important information to astrophysics and cosmo-

chemistry research. Dust grains do not only absorb, reflect, and scatter optical light from nearby stars but also radiate in the infrared or even in the microwave wavelength range (Dikarev *et al.*, 2009). Observations of protoplanetary discs embedded deep in molecular clouds help to understand star and planet formation processes, whereas infrared measurements of starburst galaxies reveal the grand picture of galaxy evolution.

1.1.2   Concept of Dust Astronomy

Due to the high mobility, dust particles can be transported over large distances. In this respect, they act similar to photons which carry information from the site of formation. With proper methods the message sealed in dust grains can be extracted and provide unique insights into their sources and transportation processes. This constitutes the "Dust Astronomy" concept proposed by Eberhard Grün (Grün *et al.*, 2001), which can be realized with in–situ dust measurements and theoretical modeling. Certainly this concept is not necessarily confined to interstellar dust (ISD) studies and can also be applied to planetary science research. Following this idea, this work focuses on stream–particle observations as well as the implication of the interactions between dust grains and the planetary magnetosphere.

1.2   Stream Particles

The definition of stream particles is based on their dynamical properties: fast and tiny. Their velocities are generally greater than 100 $\mathrm{km\,s^{-1}}$ and may even reach the solar wind speed. The mass of stream particles is estimated to be about 10^{-21} kg (Zook *et al.*, 1996), which is equivalent to spheric grains with radius of few nanometers. So far, both Jovian and Saturnian systems are found to be the source of stream particles. Amongst all known cosmic dust categories in the solar system, stream particles are the most extreme population.

1.2.1   Discovery and History

The discovery of Jovian stream particles was an unexpected finding by the Ulysses spacecraft during its first Jupiter flyby in 1992 (Grün *et al.*, 1993). At a distance of about 1 AU (1 AU is the average Sun–Earth distance, which is about 150,000,000 km) away from Jupiter, the dust detector on board Ulysses spacecraft started to register bursts of sub–micron particle impacts from the direction close to Jupiter line–of–sight. After the close approach, till the last "dust stream" detected at the Ulysses–Jupiter distance of 2 AU, in total 11 impact bursts were registered during this period (Baguhl *et al.*, 1993). Moreover, these impact bursts showed a 28±3 day periodicity, which

closely matches the solar rotation period.
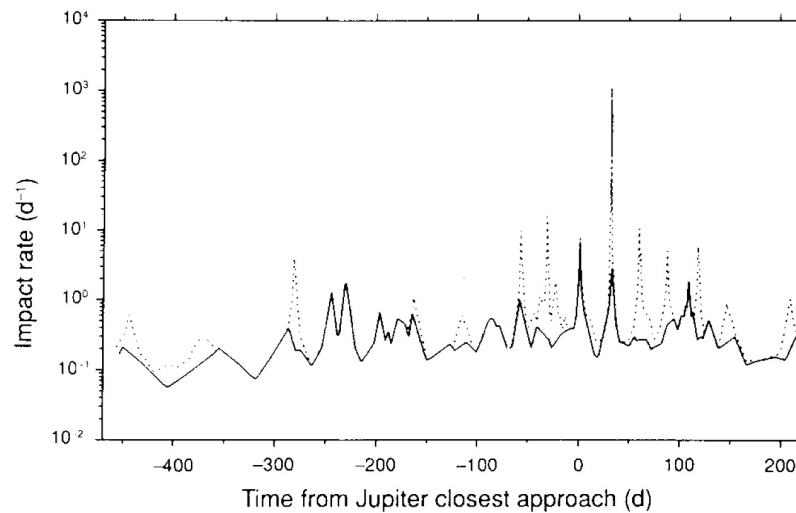
Figure 1.3: The stream–particle observation during the first Ulysses Jupiter flyby. - The figure from Grün *et al.* (1993) shows the impact flux over a two year interval. The flux of larger particles is marked by the solid line. The dotted line is the flux of all recorded impacts. Note that the periodic dotted line peaks around Jupiter closest approach (CA) which occurred on 8 February, 1992.

Based on the work by Morfill *et al.* (1980), Horányi *et al.* (1993) demonstrated that with proper size the positively charged dust particles can acquire enough energy from the outward pointing co-rotation electric field ($\mathbf{E}_c$) and escape from Jupiter with high velocity. Hamilton & Burns (1993) noticed that the dynamics of these submicron dust particles was strongly influenced by the interplanetary magnetic field (IMF). The authors proposed that after ejection from the magnetosphere, stream particles form a dust sheet which is then warped by the IMF. Impact bursts would be detected by a spacecraft whose trajectory crosses the warped dust sheet, which is coupled to the IMF modulation originating from the rotating Sun, and therefore result in periodic stream–particle activities.

However, the extreme properties of stream particles were not really explained until the work by Zook *et al.* (1996). By means of numerical simulations these authors convincingly showed that only grains of about 10 nm with speeds exceeding $100\,\mathrm{km\,s^{-1}}$ are compatible with the Ulysses observations. These studies explained most of the observed features and laid the foundation for the stream–particle dynamics studies. However, the source of these nanometer sized particles was still ambiguous.

After Ulysses measurements outlined the stream particle dynamics in interplanetary space, carrying the twin dust detector, Galileo spacecraft arrived at Jupiter in 1996 and provided further details within the Jovian magnetosphere. The continuous dust measurements during the seven–year Galileo mission not only allowed to study the time variability of stream particles' activity (see section 1.5.1), but also to perform a frequency analysis. Figure 1.4 from Grün *et al.* (1998) shows a 5 and 10 hour feature in stream–particle measurements and indicated a strong modulation of the streamparticle activity by the Jovian magnetic field. Moreover, the orbital period of the volcanic active moon Io was identified in the Galileo dataset and strongly suggested that Io is the main source of Jovian stream particles (Graps *et al.*, 2000, figure 1.5).
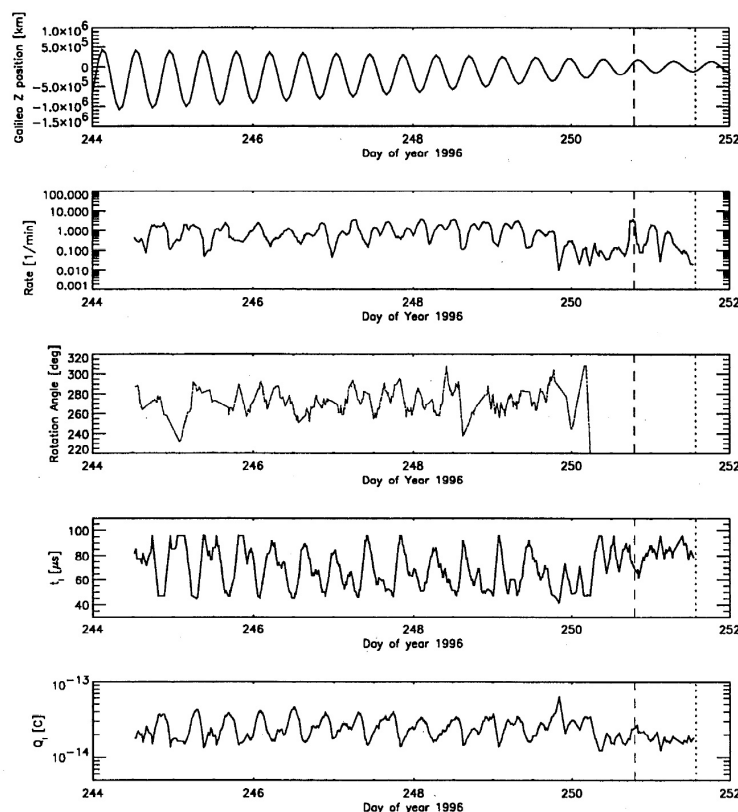
Figure 1.4: Galileo stream–particle measurements during orbit G2. - The figure from Grün *et al.* (1998) shows periodic stream–particle activity in the magnetosphere. With a $\sim 10°$ offset between Jupiter's magnetic and rotation axes, the spacecraft located in the equatorial plane experiences the field fluctuation every half Jupiter rotation (about 10 hours). As shown in the plot, the flux, impact charge yield, and the signal rise time of stream particles were all coupled to the Galileo magnetic latitude. Besides the 5 and 10 hours feature, the amplitudes of these quantities also evolved with time.

Periodogram: Galileo dust detector 1996–1997
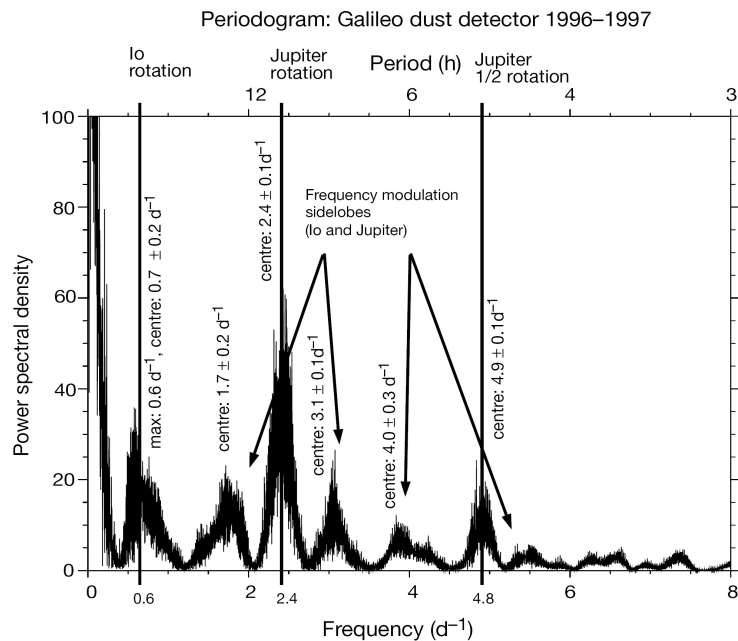
Figure 1.5: Io revealed from Galileo stream–particle measurements. - The figure from Graps *et al.* (2000) shows the Lomb–Scargle periodogram for the first two years of Galileo data. Three high peaks from left to right correspond to Io's orbital period, the rotation period of Jupiter, and half of rotation period of Jupiter. Harmonics of these frequencies are also visible. The highest peak near the origin is due to the orbital geometry of Galileo spacecraft.

After three years of interplanetary journey, the Cassini spacecraft (see section 1.4) flew by at Jupiter at a closest approach distance of approximately 0.065 AU (137 Jupiter radii, $1\,R_J = 71,492\,km$). The Cosmic Dust Analyser (CDA) on board Cassini (Srama *et al.*, 2004, and section 1.4.2) is an impact ionization dust detector, similar to the dust instruments on Ulysses and Galileo, but additionally equipped with a time-of-flight mass spectrometer. The analysis of Jovian stream particles' mass spectra suggested that the grains are mostly composed of sodium chloride (NaCl) formed by condensation within Io's volcanic plumes (Postberg *et al.*, 2006, see also section 1.2.4).

The existence of Saturnian stream particles was first predicted by Horányi (2000) based on the plasma model derived from the Voyager data. The discovery of Saturnian stream particles during Cassinis Saturn approach in 2004 (Kempf *et al.*, 2005a) confirmed the idea of the Saturnian system being the source of fast nanometer sized dust particles. Half a year before the orbit insertion, CDA started to register stream

particle impacts at a distance of about 0.56 AU (1,400 Saturn radii, 1 R_S = 60,330 km) from Saturn (Kempf *et al.*, 2005a). The particle flux increased as the distance to Saturn decreased, which was taken as an indication that these particles originated from Saturn.

While the compositional information provides direct evidence of Io being the major source of Jovian stream particles, most mass spectra from Saturnian stream particles were faint and hard to interpret. Moreover, the dominant mass lines in the spectra are either from the target (Rh^+) or target contaminations (H^+, C^+) (Postberg *et al.*, 2009a). By adding spectra of similar strength and with similar features, Kempf *et al.* (2005b) found that most spectra were of silicate type (74%). This was a surprise because the dense main rings and the tenuous E ring together with the embedded icy moons are mostly composed of pure water ice (Hillier *et al.*, 2007; Pilcher *et al.*, 1970). Therefore, the authors suggested that Saturnian stream particles should resemble the silicate cores embedded in icy particles and released through collisional processes.

1.2.2 Dynamics

One of the intriguing features of dust dynamics is its complexity. Various forces need to be taken into consideration and the ratio between them, i.e., the relative importance, depends on the ambient environment as well as dust particles' properties. Taking micron sized particles in Saturn's E ring as an example (figure 1.6), the dynamical influences from the gravity, the electromagnetic force, and the radiation pressure force are roughly comparable in strength but acting towards different directions. Moreover, thinking of the long–term evolution, weak drag forces resulting from the magnetospheric co–rotation plasma flow also needs to be taken into account (Beckmann, 2008; Horányi *et al.*, 2008).

Due to the nanometer scale of stream particles, their dynamics is dominated by the electromagnetic field. On top of that, charging processes play a very important role in the dynamical evolution path of these nanodust particles because the grain charge is directly related to the amplitude of the Lorentz force. In general, the stream–particle dynamics can be divided into two domains: propagation of stream particles in the interplanetary space and the ejection process inside the planetary magnetosphere.

As the name 'stream particle' originates from the "dust stream" phenomenon observed in interplanetary space, it is indicative of strong IMF influence on their dynamical properties. The main acceleration exerted on stream particles comes from the IMF carried by the solar wind plasma moving outward from the Sun. Due to the relative velocity between the solar wind and stream particles, an co–moving electric field is induced and can be written as: $\mathbf{E}_{co} = -\mathbf{V_{sw}} \times \mathbf{B}$, where $\mathbf{V_{sw}}$ and $\mathbf{B}$ are vectors of solar wind velocity and interplanetary magnetic field. Because of $\mathbf{E}_{co}$, dust parti-

cles in interplanetary space predominantly experience an acceleration perpendicular to the solar wind flow direction. Assuming an electrostatic potential of +5 V, Zook *et al.* (1996) showed that the Lorentz force dominates gravity by more than three orders of magnitude for Jovian stream particles in interplanetary space. Moreover, within compressed solar wind regions, the IMF strength could increase by a factor of ten compared to rarefaction solar wind regions. As will be shown in section 3.4.3, the acceleration a stream particle experiences during solar wind compression is comparable to its primary momentum it obtains during the ejection process in the planetary magnetosphere. Therefore, in order to quantify the ejection conditions, the modification of stream–particle dynamics by the IMF must be considered first for the observations in interplanetary space.
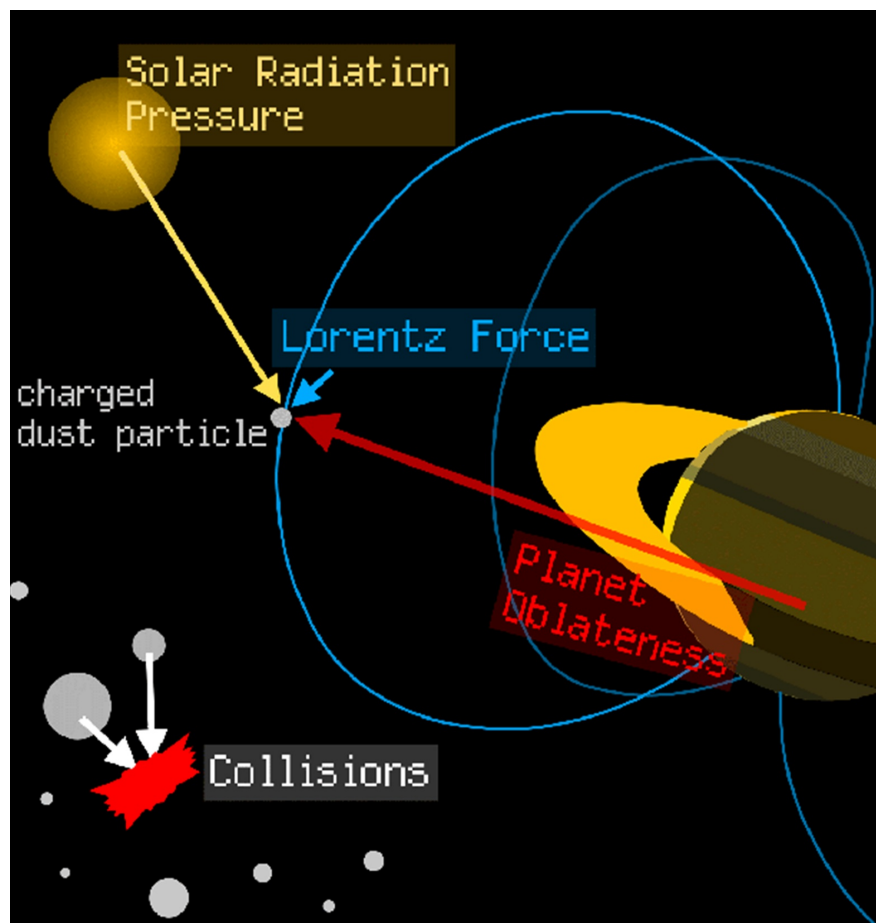
Figure 1.6: The equation of motion of charged dust particles in a schematic view. - Take Saturnian E ring dust particles as an example. Different forces acting on charged dust particles with similar strengths but towards different directions.

In Jupiter and Saturn's magnetosphere, outside of the synchronous orbit positively charged dust particles can receive energy from the outward pointing co–rotation electric field ($\mathbf{E}_c$) to overcome the gravity from the planet and escape. The equation of energy conservation can be written as:

$$\frac{1}{2}m_d v_{ex}^2 = -\frac{GM_P m_d}{2r_0} + \int_{r_0}^{r_{ms}} \cdot Q_d \cdot \mathbf{E}_c \, dr \qquad (1.1)$$

where G is the gravitational constant, M_P is the mass of the planet. The first term at the right–hand side is the total energy of a dust particle with initial Keplerian motion. The second term is the energy that particles acquire from the co–rotation electric field. The E field can be expressed as $\mathbf{E}_c = -\mathbf{V_{co}} \times \mathbf{B}$, where $\mathbf{V_{co}} = -r \times \Omega$ is the corotation velocity, Ω is the planet rotation frequency, and $\mathbf{B}$ is the planetary magnetic field. The r is the distance to the planet, r_{ms} is the boundary of the magnetosphere, and r_0 is the radial distance where a particle starts to be accelerated by $\mathbf{E}_c$.

Assuming a dipole magnetic field with ridge corotation and constant grain charges, from Eq. 1.1 the ejection speed of particles located in the magnetic equatorial region can be expressed as:

$$v_{ex}^2 = 2GM_P r_0^{-1}(L^* - \frac{1}{2}) \qquad (1.2)$$

where $L^* = L(1 - r_0/r_{ms})$ and

$$L = \frac{Q_d}{m_d} \frac{\Omega \mathbf{B}}{GM_P}$$

is the ratio between gravity and the electromagnetic force.

On one hand, for particles with L^* less than $\frac{1}{2}$ the gravity prevails over $\mathbf{E}_c$ and traps these particles in the system. On the other hand, particles with large charge–to–mass ratio behave similar to plasma and are bound to the magnetic field (the *Alfvén criterion*). These criteria give the upper and lower size limits of stream particles:

$$s_{max}^2 = \frac{6\varepsilon_0 \phi_d}{\rho_d} \frac{\Omega \mathbf{B}}{GM_P}(1 - \frac{r_0}{r_{ms}}) \qquad (1.3)$$

$$s_{min}^2 = \frac{B\varepsilon_0 \phi_d}{\rho_d \Omega} \left[\sqrt{\frac{GM_P}{\Omega^2 r^3}} - 1 \right]^{-1} \qquad (1.4)$$

As the plasma environment changes with the distance to the planet, the surface potential of dust grains varies accordingly. Values given above with simplified scheme which demonstrates the physical insights, however can only be taken as first–order estimates. To provide better constraints on stream particles' dynamical properties, charging processes must be considered.

1.2.3 Charging Processes

Unlike in the interplanetary space where the plasma density is low and the grain charging is governed by the photo–electron current induced by solar UV photons, in planetary magnetospheres the plasma density is much higher and therefore the most important charging current owes to thermal electron population. Moreover, the plasma composition as well as plasma temperature may vary over the magnetosphere due to active sources and complex plasma chemistry and magnetospheric dynamics, which results in grain charge variation and consequently affects the dynamical evolution of charged dust grains (not only stream particles) in the magnetosphere.

The time evolution of electric charges (Q_d) carried on a dust grain in a plasma environment is:

$$\frac{dQ_d}{dt} = J_e + J_i + J_\nu + J_{sec}$$

The J_e and J_i are the electron and ion collection currents, i.e, the flux of electron and ion that a dust grain captures from the ambient plasma. The J_ν and J_{sec} are the photo–electron and secondary electron emission currents, which describe the flux of photo–electron / secondary electron induced by solar UV photons / energetic electrons. The electron current is a negative current while the others are positive. The currents depend on various conditions, such as plasma characteristics (the composition, the number density, the temperature, and the energy distribution of plasma), the solar UV photon flux (effect on J_ν), and dust grain properties (the surface potential ϕ, the material properties, the dust grain–plasma relative speed, etc.). Figure 1.7 schematic sketch of dust charging in a space environment.

The dust charging calculation in this work basically follows the "Orbit Motion Limit" (OML) theory (Mott-Smith & Langmuir, 1926) which is valid under condition of $s_d \ll \lambda_D \ll D_d$ where the s_d, λ_D, and D_d are the grain radius, the plasma Debye length, and the inter–grain distance respectively. This theory bases on conservations of energy and angular momentum and assumes a homogenous plasma to calculate the trajectory of plasma particles with respect to the 'floating probe'. The OML criteria are fulfilled in most space environments and OML is the widelyused theory for calculating the spacecraft charging as well as the dust grain charge. The charging currents are described in the following.

J_e and J_i are simply the flux of plasma particles (electron or ion) collected by a dust grain per unit time. These two currents depend on the properties of the ambient plasma and electrostatic potential of a dust grain. Assuming a Maxwellian plasma which is stationary to the dust particle, the electron and ion collection currents can be described as:

$$J_{e,i} = J_{e,i}^0 \times \begin{cases} 1 - \chi_{e,i}, & \text{if } \chi_{e,i} < 0 \\ e^{-\chi_{e,i}}, & \text{if } \chi_{e,i} \geq 0 \end{cases} \tag{1.5}$$

where $J_{e,i}^0 = \mp 4\pi s_d^2 e_0 n_{e,i} (kT_{e,i}/2\pi m_{e,i})^{1/2}$, and $\chi_{e,i} = \mp e_0 \phi_d / kT_{e,i}$. $k = 1.38 \times 10^{-23} \text{JK}^{-1}$ is

Boltzmann's constant. The $n_{e,i}$, $T_{e,i}$, and $m_{e,i}$ are the density, temperature, and mass of the electron and ion. The e_0 is the elementary charge.
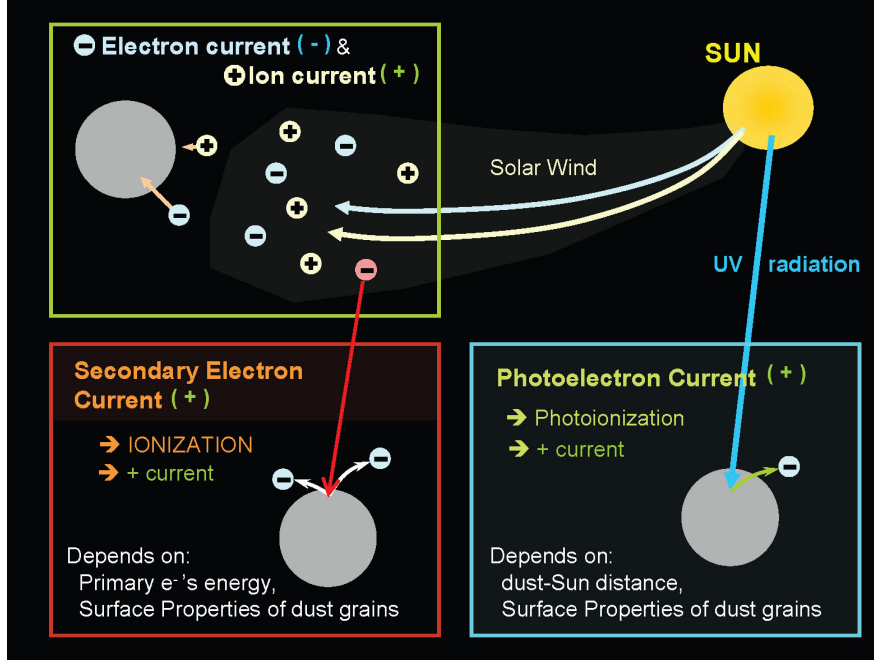
Figure 1.7: The charging equation in a schematic view. - Different charging currents on dust particles in the space environment.

Eq. (1.5) shows the attracting ($\chi_{e,i} \leq 0$) and repellent ($\chi_{e,i} \geq 0$) case of a collection current. A dust grain with higher potential will collect less plasma particles with the same electric sign. For example, only electrons with energy greater than $1\,\mathrm{eV}$ are able to overcome the repellent field from a dust grain with $-1\,\mathrm{V}$ potential and to be collected on to it. In most space environments, J_e is larger than J_i because of the mass difference between electrons and ions.

J_ν is the photo–electron emission current, i.e., the flux of escaping photo–electrons that is induced by the solar UV photons, and is given by

$$J_\nu = J_\nu^0 \times \begin{cases} 1, & \text{if } \chi_\nu \leq 0 \\ e^{-\chi_\nu}, & \text{if } \chi_\nu > 0 \end{cases} \tag{1.6}$$

where $J_\nu^0 = \pi s_d^2 e_0 \kappa_\nu f_d$ and $\chi_\nu = -e_0 \phi_d / kT_\nu$. κ_ν is the photo–electric coefficient, here I adopt $\kappa_\nu = 0.1$, which is typical for a non–conductor. $f_d = 2.5 \times 10^{10} d^{-2}\,\mathrm{cm^{-2}sec^{-1}}$ is the solar UV photon flux scaled to the dust–sun distance, d, in unit of AU. $kT_\nu = 3\,\mathrm{eV}$ is

the mean photo–electron energy. In the Saturnian magnetosphere, the photo–electron current contributes only little for the charge balance. However, it is the dominant current in interplanetary space due to low plasma density.

The secondary electron emission current, J_{sec}, describes the flux of secondary electron emission induced by high energy plasma particles. At Saturn, the secondary electrons are mostly produced by high energy electrons. The current is given by

$$J_{\nu} = J_s^0 \times \begin{cases} F_{5,B}(E_m/4kT_e)(1-\chi_s)e^{\chi_s}, & \text{if } \chi_s < 0 \\ F_{5,0}(E_m/4kT_e), & \text{if } \chi_s \geq 0 \end{cases} \tag{1.7}$$

where $J_s^0 = 3.7\delta_M J_e^0 e^{\chi_e}$ and $\chi_s = -e_0\phi_d/kT_s$. δ_M is the maximum secondary yield with optimum energy of E_m of the incident electrons. $kT_s = 3\,\text{eV}$ is the mean secondary electron energy. $F_{n,m}(x) = x^2 \int_m^\infty y^n e^{-(xy^2+y)}\,dy$ and $B = (-\chi_e/(E_m/4kT_e))^{1/2}$.

As plasma observations suggest that the plasma's energy distribution can strongly deviate from equilibrium, the application of the generalized Lorentz distribution for describing the energy distribution of plasma electrons and related currents is discussed in section 5.3.2.

1.2.4 Chemical Composition

As briefly described in section 1.2.1, the CDA has measured the composition of stream particles originating both giant planet systems. The results are surprisingly interesting because the composition of stream particles are found to be different from the neutral gas / plasma in both systems. In the Jovian magnetosphere, contrary to the NaCl stream particles (Postberg *et al.*, 2006), sulfur and oxygen dissociated from the SO_2 are the dominant plasma ion populations. For stream particles from the water ice–rich Saturnian system, siliceous material dominates water ice in the most Saturnian stream particle mass spectra (Kempf *et al.*, 2005b).

The compositional discrepancy between stream particles and the ambient plasma / neutral gas provides insights to their formation process. For the Jovian case, Schaefer & Fegley (2005) had shown that the sodium chloride, the major stream–particle composition, is the most abundant condensate at the gas temperature $\leq 1000\text{K}$ (figure 1.8). In contrast, the condensation temperature of SO_2 is about 115K depending on the atmospheric pressure. Due to the high condensation temperature of sodium chloride, it forms at high altitude as the volcanic gas cools down adiabatically. The gas column height of Prometheus–type (Geissler & McMillan, 2008) and Pele–type plumes are either comparable to or higher than the height of Io's ionosphere (Hinson *et al.*, 1998). Hence, the high condensation temperature provides larger chance for sodium chloride particles to enter the magnetosphere, where the electron temperature is much higher than in the ionosphere (4 to 5 eV compare to 0.1 eV). Considering

the limited charging effect due to high dust density, Ip (1996) showed that the mass injection rate of 10nm size particles is about 0.1 to 1kg, which agrees with the Galileo measurements (Krüger *et al.*, 2003).
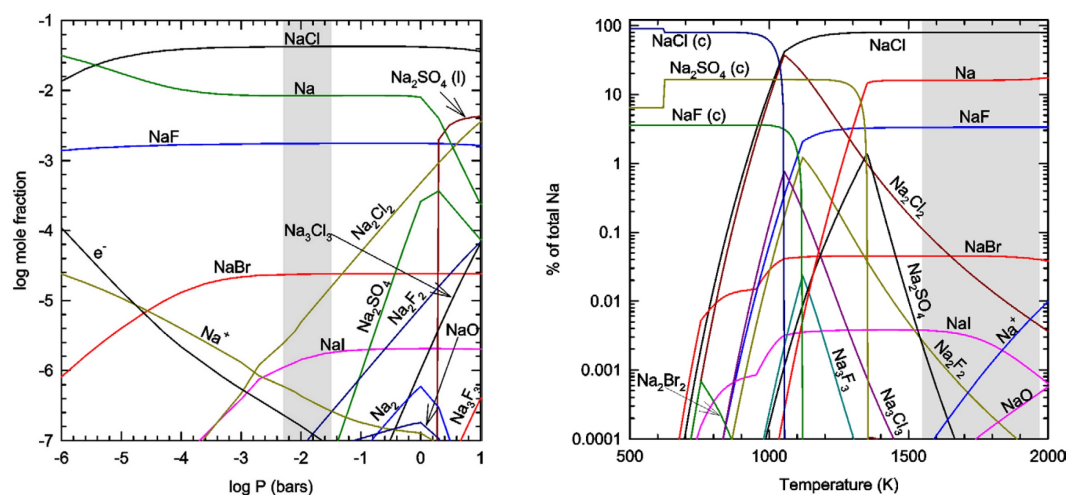
Figure 1.8: Equilibrium chemistry of the Pele plume. - The figure from Schaefer & Fegley (2005) shows the equilibrium chemistry of sodium as function of total pressure (left) and temperature (right). The temperature at left panel is fixed at 1760K, the total pressure at right panel is about 0.01 bar. Sodium chloride condensation curve is marked as "NaCl(c)" in the right panel.

For the Saturnian case, the difference of the sputtering rate between water ice and siliceous material has been found to be responsible for the compositional discrepancy. In Saturn's magnetosphere, the E ring particles' life time is mainly controlled by the sputtering of thermal plasma ions (Jurac *et al.*, 2001, figure 1.9). Figure 1.10 shows the sputtering rate of water ice by oxygen ions and protons in energy range of thermal ions in Saturn's magnetosphere (note that the unit of abscissa is eV/amu). Based on the latest Cassini plasma measurements, the authors confirmed the E ring particle age estimated by Jurac *et al.* (2001).

Figure 1.11 shows the sputtering yield of water ice and siliceous materials by helium ions. For ion energies ranging between 10 to 100 eV (the energy range of thermal ions in Saturn's E ring, see figure 5.8), the sputtering yield of water ice is more than an order of magnitude higher than silicates (though the ion species responsible for the sputtering is not He^+, the tendency should be at least qualitatively the same). Presuming that E ring grains ejected by the Enceladus' plume into the E ring contain tiny amounts of siliceous nanoscale inclusions, the icy material is constantly sputtered

by magnetospheric plasma whereas the embedded siliceous cores keep intact and eventually are released from the ice matrix and forming stream particles. More detail related to the compositional selection process of Saturnian stream particles will be discussed in section 5.5.
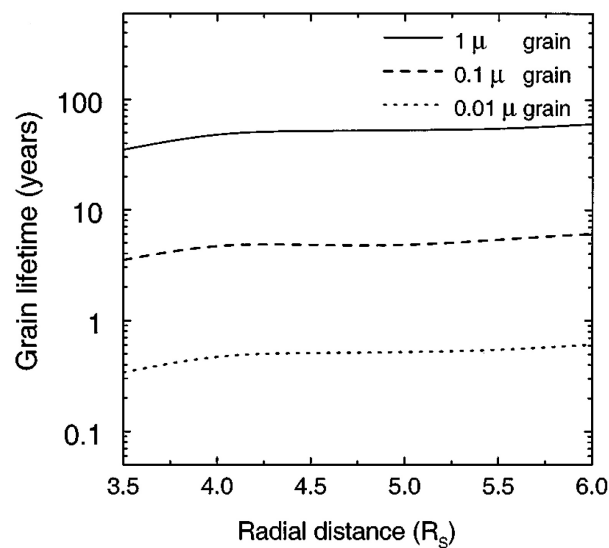
Figure 1.9: The sputtering lifetime of E ring dust particles. - The figure from Jurac *et al.* (2001) shows the estimates of the sputtering lifetime of different size E ring particles.

1.2.5   Stream Particle Terminology

Since the first detection of stream particles, our knowledge regarding their dynamical and compositional properties have been largely increased within last two decades. However, the terminology of "stream particle" still retains its original form at the time of discovery. Originally the term "dust stream" referred to the impact burst period observed by the dust detectors on Ulysses and Galileo (Grün *et al.*, 1993, 1996). In contrary to CDA beneficial from the H^+ mass line triggering mechanism which enhanced the stream–particle detection sensitivity, these detectors were not sensitive enough to register the much fainter impacts between two successive bursts the instrument teams naturally assumed that the spacecraft passed through intense collimated "dust streams".
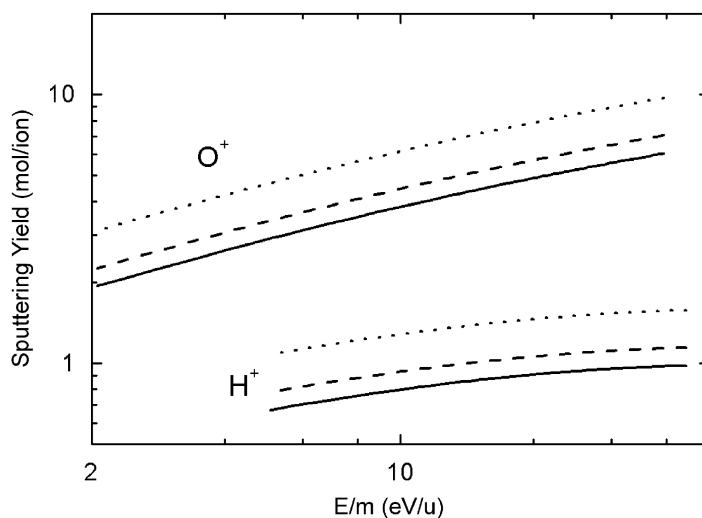
Figure 1.10: The sputtering yield of water ice by H$^+$ and O$^+$. - The figure from Johnson *et al.* (2008) shows the sputtering yield of water ice by H$^+$ and O$^+$ at normal incidence with different ice temperature: solid – 80K, dashed – 100K, and dotted – 120K. The ion energy is expressed in unit of eV/amu.
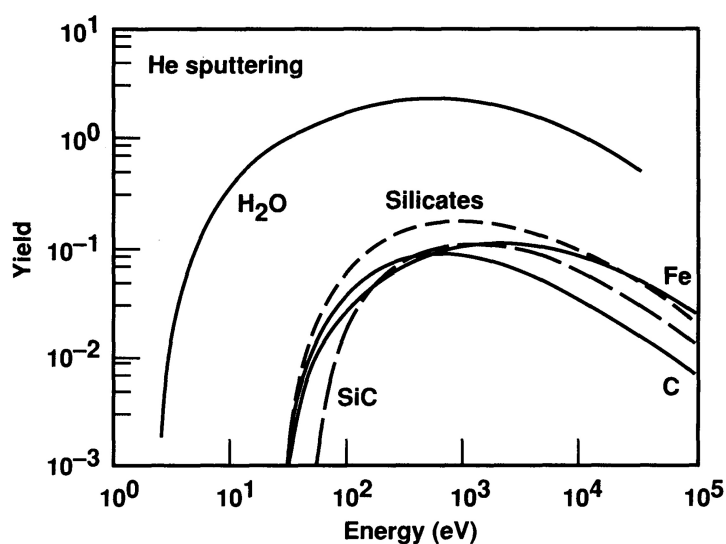
Figure 1.11: The sputtering yield difference between water ice and silicates. - The figure from Tielens *et al.* (1994) shows the sputtering yields of He$^+$ on various materials.

Table 1.1: The basic properties of Jupiter and Saturn.

	Jupiter	Saturn
mass (10^{26} kg)	18.986	5.6846
equatorial radius (km)	71,492	60,268
reference radius (km)	71,492	60,330
heliospheric distance (AU)	5.2	9.5
orbital period (year)	4.332	29.457
rotation period (hour)	9.925	10.57
axial tilt ($^\circ$)	3.13	26.73
surface magnetic field strength (Gauss)	4.24	0.22
tilt angle of magnetic dipole axis ($^\circ$)	9.6	< 1

As will also be discussed further in section 3.1, in this work I refer stream particles to fast ($> 100\,\mathrm{km\,s^{-1}}$) and tiny (few nm) dust particles from Jovian and Saturnian systems. Instead of using the misleading "dust streams", the phrase 'impact bursts' is recommended for clarity.

1.3   Jovian and Saturnian Systems

Jupiter and Saturn are both giant gaseous planets with extensive ring and satellite systems. Even after decades of studies, their internal structure, atmosphere, satellites and dust rings still hold wealthy scientific surprises waiting for further explorations. Comparing similarities and dissimilarities between these two systems help to clarify the fundamental processes behind the observed phenomena. Table 1.1 lists their basic properties.

1.3.1   Jupiter and Io

Jupiter is the largest planet in our solar system. Its mass is about 317.8 $M_\oplus$ (Earth mass) and its equatorial radius is about 10.5 $R_\oplus$ (Earth radius). Moreover, Jupiter also hosts the most massive satellite systems. The Galilean satellites and the Great Red Spot, a storm system persistent for few hundred years, are shown in figure 1.12. The densities of these four planetary sized moons (table 1.2 shows a interesting fact that the density of Galilean satellites decreases with distance to Jupiter. The density variation is indicative of the compositional gradient. The moons' composition changes from inner rock (Io) to outer rock–ice mixture (Ganymede and Callisto) which may reflect

17

Table 1.2: Properties of Galilean satellites.

Satellite	Distance to Jupiter (R_J)	Radius (km)	Mass (10^{22} kg)	Density (g cm^{-3})	Orbital Period (day)
Io	5.9	1822	8.9	3.528	1.77
Europa	9.4	1561	4.8	3.01	3.55
Ganymede	15.0	2631	14.8	1.936	7.15
Callisto	26.4	2411	10.8	1.834	16.69

the temperature gradient at the formation of the system.

Due to the orbital resonance between Io, Europa, and Ganymede, the eccentricity of Io's orbit is maintained and results in the tidal heating which serves as the main source of its internal heat and geological activities. The Ionian volcanism has several important consequences for Io itself as well as the whole Jovian system. First, various volcanic activities such as plume eruptions, lava flows, and paterae (caldera–like depressions) formations shape the Io surface with complex structures and colorful appearance. Secondly, Io has a tenuous atmosphere (mainly SO_2) provided by the gas emitted from Io's volcanoes as well as the surface sublimation. The image taken while Io was in eclipse showed the Io aurora emission due to the interaction between its atmosphere and magnetospheric plasma (Geissler *et al.*, 1999, figure 1.13).

Furthermore, every second Io releases about 1 ton of gas (mostly SO_2 and dissociation products) into the Jovian magnetosphere (Bagenal, 2007). These neutral gas is soon ionized, forms the Io Plasma Torus (IPT), and makes Io the major source of plasma in the magnetosphere. Similar to the Rayleigh–Taylor instability of fluids, the newly formed cooler plasma undergoes a fluxtube interchange process with the outer hot but less dense fluxtubes and is transported outward. Due to the conservation of angular momentum, the plasma lose its angular speed during the outward transport. A large scale current system, associated with the main oval auroral emission, is then developed and couples the ionosphere and magnetosphere in order to maintain the co–rotation.

Besides the plasma, as described in section 1.2.4, Io is also the source of Jovian stream particles, which links stream particle studies to Io volcanism. Shown in figure 1.14 are multi–wavelength images of Io taken by the New Horizons spacecraft during its Jupiter encounter in 2007. Close to the north pole of Io, an enormous plume emanated from the volcano Tvashtar was observed with altitude of 330 km. Besides, other weaker volcanic spots were observed in the infrared wavelength (lower right of figure 1.14).
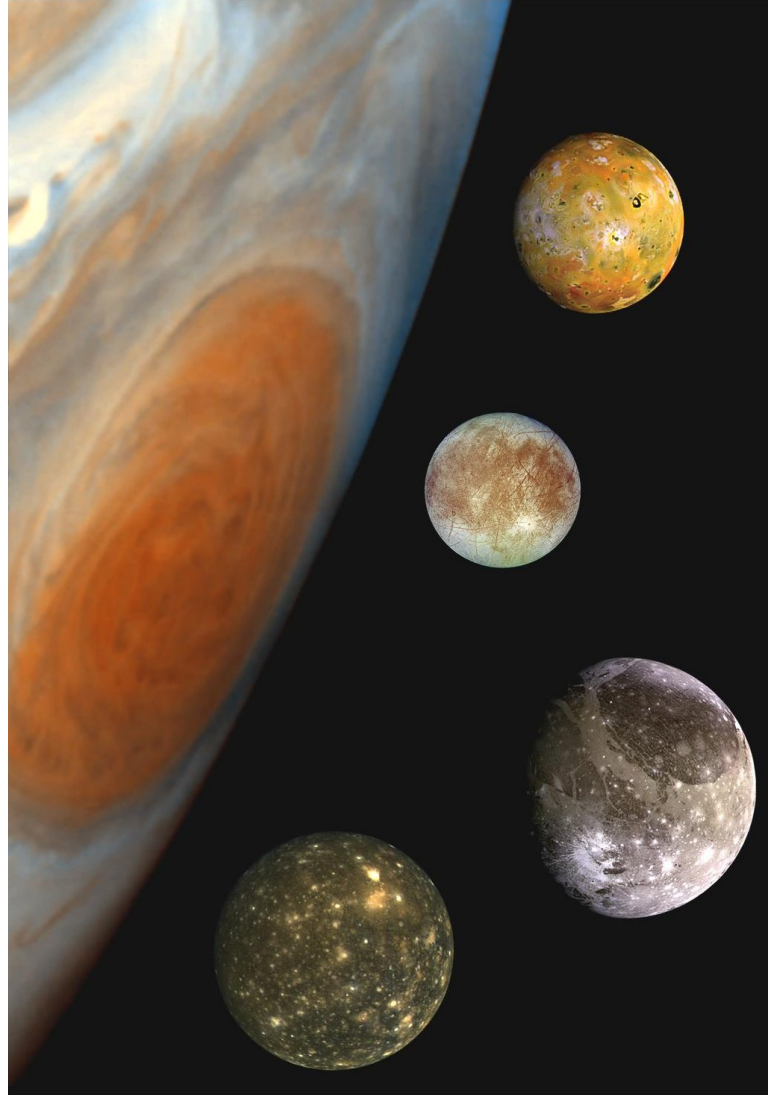
Figure 1.12: Family Portrait of Jupiter's Great Red Spot and the Galilean Satellites. - This composed picture from Galileo spacecraft images shows the edge of Jupiter with the Great Red Spot and four Galilean satellites. The Great Red Spot is a storm system persistent for few hundred years. At the right side, from top to bottom are the four Galilean moons arranged according to their orbital distance to Jupiter. Io has the strongest volcanic activities in the solar system. Its vivid appearance is painted by the sulfurous compounds provided by its volcanism. Europa is about the size of Earth's Moon but with a almost crater–free icy surface. Together with the magnetic field disturbance measured by Galileo spacecraft, it is proposed that a sub–surface ocean is located under the 10 km thick ice crust. Ganymede is the largest satellite in the solar system and is the only one known to have its own magnetosphere. Callisto is located further away and is not involved in the orbital resonance of three inner moons. Its surface is heavily cratered and shows no signs of on–going geological activities. Source: NASA Planetary PhotoJournal
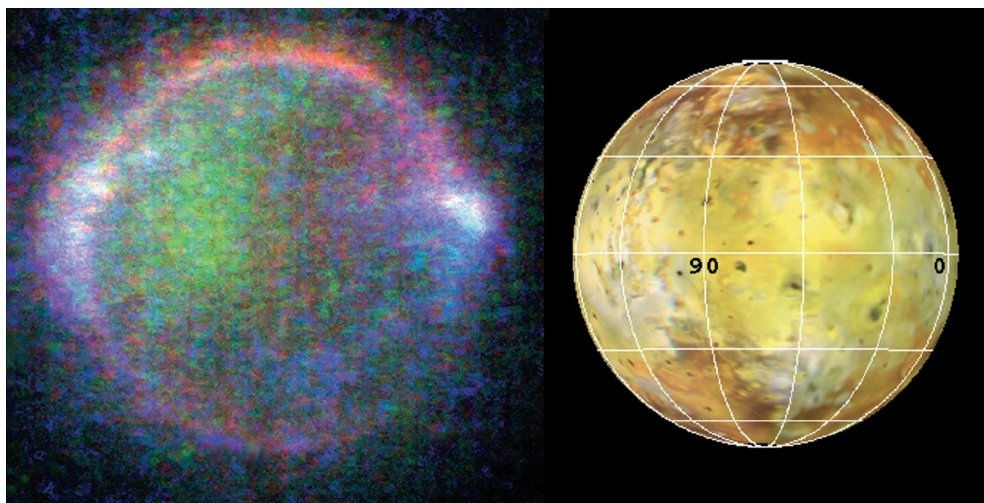
Figure 1.13: Galileo image of Io in eclipse. - (Right) Illuminated Io disc with similar perspective as the left image. (Left) The image is from Galileo SSI Io eclipse observation in 1998. The bright blue spots located at sub– and anti–Jupiter point (longitude 0° and 180°) were emissions from volcanic plumes (Geissler *et al.*, 1999).

Regardless if considered from a observational perspective or from the stream particle formation point of view, the ionian volcanic plume eruption is a tremendous phenomenon. There are two types of plumes on Io: Prometheus–type and Pele–type. Prometheus–type plumes are relatively small but steadily erupting volcanic plumes. They are composed of an optically thick dust column (mean height: 82 ± 17km), which is responsible for the surface change, and also a higher gas component (mean height: 258 ± 87km). The particle size of the optically thick dust component is about 100nm. Moreover, a halo made of fine dust grains with size smaller than 10nm was suggested for volcano Thor. This fine grained dust component may comprise $> 90\%$ of plume dust mass and is comparable to the mass of the plume gas (Geissler & McMillan, 2008).

Pele–type plumes are much higher (> 300 km) in altitude but seem to be short–lived. The plume emanating from Tvashtar observed by New Horizons is also of a Pele–type (Spencer *et al.*, 2007, figure 1.14). They do not exhibit an optically thick dust column and are difficult to be observed in visible wavelengths. In shorter wavelength they generally show a shield–shaped structure, which suggests that the dust particles are tiny and condensed directly from the gas.

The process of how nanometer sized particles are fed into IPT and ejected with the Io orbital period encoded in stream particle flux has not yet been studied in detail.

Based on CDA measurements during Cassini's Jupiter flyby during 2000 / 2001, in section 1.5.1 I provide an interesting result that links Galileo dust measurements, CDA measurements, and the ultraviolet emission from IPT observed by Cassini Ultraviolet Imaging Spectrograph (UVIS) and helps to understand the connection between Ionian volcanic activities, IPT variations, and the stream–particle ejection.

Figure 1.14: Io Through Different Eyes. - The left image shows fine details on Io's sunlit crescent and in the partially sunlit plume from the Tvashtar volcano, and reveals the bright nighttime glow of the hot lavas at the source of the Tvashtar plume. The top right image shows the contrasting colors of the red lava and blue plume at Tvashtar, and the sulfur and sulfur dioxide deposits on Io's sunlit surface. The lower right image shows that the glow of the Tvashtar volcano is even more intense at infrared wavelengths and reveals the infrared glow of at least 10 fainter volcanic hot spots on the moon's nightside. The brightest of these, Amirani / Maui, which is visible to the lower right of Tvashtar, is less than 4% as bright as Tvashtar. All of these are long-lived hot spots that have been observed previously by the Galileo orbiter. Source: CICLOPS

1.3.2   Saturn and Enceladus

Located further outward from the Sun, Saturn is the second largest planet within the solar system. The Saturnian system is characterized by its tremendous rings, middle–sized icy moons, and together with the second largest moon of the solar system –

Titan. Different from the Jovian system, the composition of Saturn's rings and satellites is mainly water ice (table 1.3). Figure 1.15 schematically shows the geometry of its rings and inner icy moons.

Figure 1.16 and figure 1.17 are visible and infrared mosaic images of Saturn's ring system from the Imaging Science Subsystem (ISS) and Visual and Infrared Mapping Spectrometer (VIMS) on board the Cassini spacecraft. Figure 1.16 is taken at high phase angle (angle between the Sun and the observer) when the spacecraft was in the shadow of Saturn during September 2006. This viewing angle brightened the dusty rings substantially, even the optically thin E ring can be clearly seen in the image. In the contrast–enhanced inserted image of fig. 1.16, few interesting structures can be found: an diffuse dust ring along the trajectories of co–orbital moons, Epimetheus and Janus (mean radii: 57.7 and 89.4km), a confined ring along 4km–wide Pallene, and also few faint spokes above the unilluminated side of the main ring. Besides the ring structure, remote sensing observations can also provide insights into the size distribution and the composition of the dust rings. Figure 1.17 is a pseudo-color image in infrared wavelength. In contrast to the main rings, F and G rings, the E ring is notable by its blue color. The unique color of the E ring had been noticed during early observations and suggested to be due to its narrow particle size distribution (Bauer *et al.*, 1997; de Pater *et al.*, 2004; Nicholson *et al.*, 1996; Showalter *et al.*, 1991, see figure 1.19).

One of the most important findings by the Cassini–Huygens mission is the discovery of the geologically active moon Enceladus. Though the crater–free terrain and complex surface structures on Enceladus had been imaged by Voyager in 1981, it is totally unexpected that a small icy moon can be so active today. Figure 1.18 obtained during an Enceladus flyby on November 21, 2009 shows the leading hemisphere of Enceladus. Old, heavily crated regions can be recognized at the upper right, modified and relaxed crater structures can be found in less old regions at the lower right. Younger terrain at lower left and the youngest south polar region are fulled of ridges and fractures and crater free.

The discovery of the active plume emanating from Enceladus' south polar region occurred during Cassini Enceladus flybys in 2005. Jets composed mostly of water vapor (Hansen *et al.*, 2006; Waite *et al.*, 2006) with dust particles (Spahn *et al.*, 2006) are ejected from long, parallel fractures called "tiger–stripes" (figure 1.20). The amount of gas emitted from Enceladus into Saturn's magnetosphere derived from Cassini UVIS stellar occultation measurements is >150 kg/s, or 5×10^{27} molecule per second (Waite *et al.*, 2006). Enceladus, like Io in the Jovian system, is the dominant neutral and plasma source in Saturn's magnetosphere.

However, different from the Jovian case, the density of the neutral gas exceeds the plasma density by more than an order of magnitude across Saturn's magnetosphere.

Table 1.3: Properties of Saturn's major satellites.

Satellite	Distance to Saturn (R_S)	Radius (km)	Mass (10^{20} kg)	Density (g cm^{-3})	Orbital Period (day)
Mimas	3.05	199	0.38	1.148	0.947
Enceladus	3.95	250	1.08	1.610	1.374
Tethys	4.89	536	6.18	0.974	1.892
Dione	6.26	562	10.96	1.476	2.740
Rhea	8.74	764	23.07	1.233	4.520
Titan	20.26	2575	1345.2	1.880	15.954
Iapetus	59.02	734	18.06	1.083	79.329

Only about 10% of emitted water vapor are turned into plasma by electron impact or photo–ionization (Sittler *et al.*, 2008). Within the dense Enceladus neutral cloud, electron temperature is low ($< 1\,\text{eV}$) and the charge–exchange due to neutral–ion collisions is the dominant mechanism to redistribute neutrals from Enceladus into broader torus between ~ 3 to $7\,R_S$ (Johnson *et al.*, 2006). Further outward from Enceladus, due to the increase of electron temperature, more ions are produced by the electron–impact ionization process. The plasma formed in the inner system then diffuses outward and undergoes a centrifugal instability interchange with the outer hot, tenuous plasma, observed as injection events in a region between 6 to $11\,R_S$ (Rymer *et al.*, 2009). The planetward transported hot electrons follow adiabatic heating and produce further ionization to the neutral torus, while the injected ions may experience charge exchange with the neutral torus which produces energetic neutral atoms (ENAs).
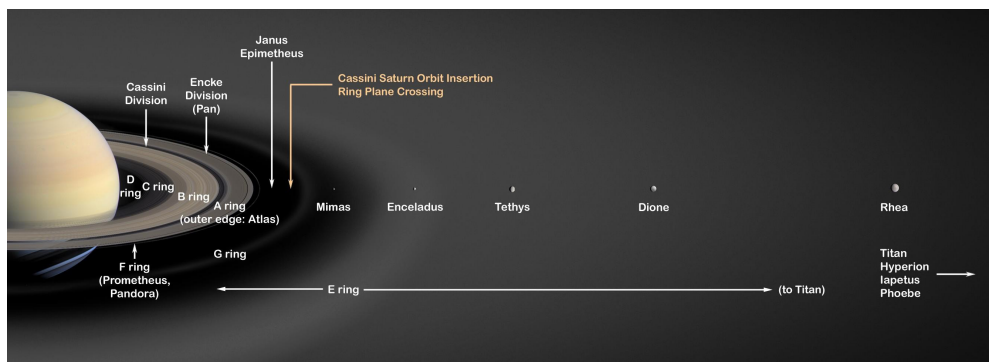
Figure 1.15: Saturn's rings and icy moons. - Source: NASA Planetary PhotoJournal
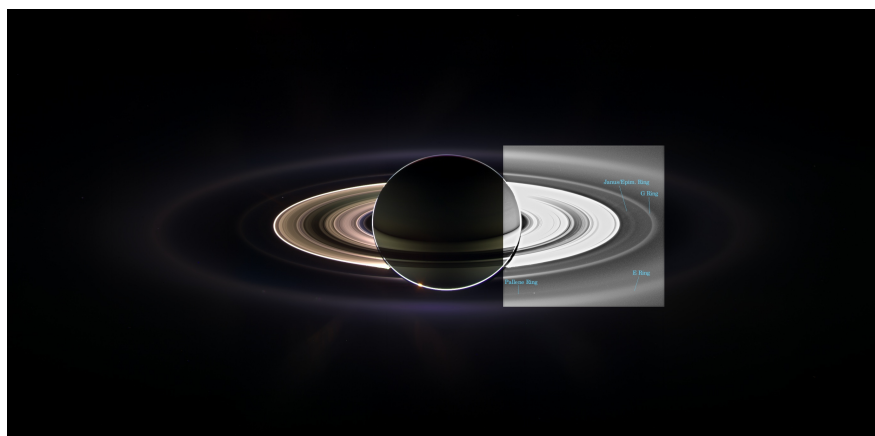
Figure 1.16: Saturn's Rings observed by Cassini ISS. - A high phase angle observation made by the Imaging Science Subsystem of Cassini spacecraft in visible light. The images used for this mosaic were taken when the spacecraft was in the shadow of Saturn. The insert figure shows the part with enhanced contrast in order to demonstrate the faint details. Source: the mosaic – CICLOPS, the contrast enhanced insert – CICLOPS
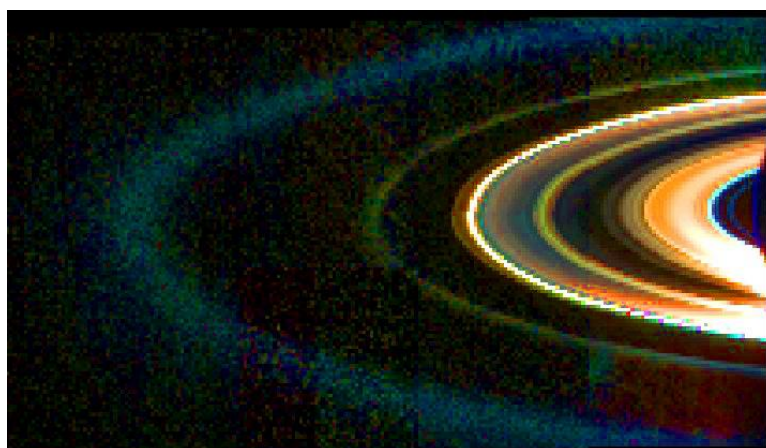
Figure 1.17: Saturn's Rings in Infrared. - This mosaic of Saturn's rings was acquired by Cassini's Visual and Infrared Mapping Spectrometer instrument on Sept. 15, 2006, while the space-craft was in the shadow of the planet looking back towards the rings from a distance of 2.16 million kilometers (1.34 million miles). Data at wavelengths of 1.0 micron, 1.75 micron and 3.6 microns were combined in the blue, green and red channels to make the pseudo-color image shown here. The brightest feature in the mosaic is the F ring, located at the outer edge of the main rings. The F ring is overexposed and appears white in this image. Of the main A, B and C rings; the C ring is the most prominent and reddish in color, becoming saturated close to the sun. The more opaque A and B rings are muddy in color and very dark in this geometry. By contrast, the normally faint D ring, located just interior to the C ring, is quite bright and blue, indicating the presence of very small ring particles. Similarly, a narrow, green ringlet in the Cassini Division, as well as the greenish G ring and blue E ring – located at increasing distances outside the F ring – are predominantly composed of small particles. The faint reddish band immediately outside the F ring is likely to be an artifact caused by the extremely bright F ring. Source: NASA Planetary PhotoJournal
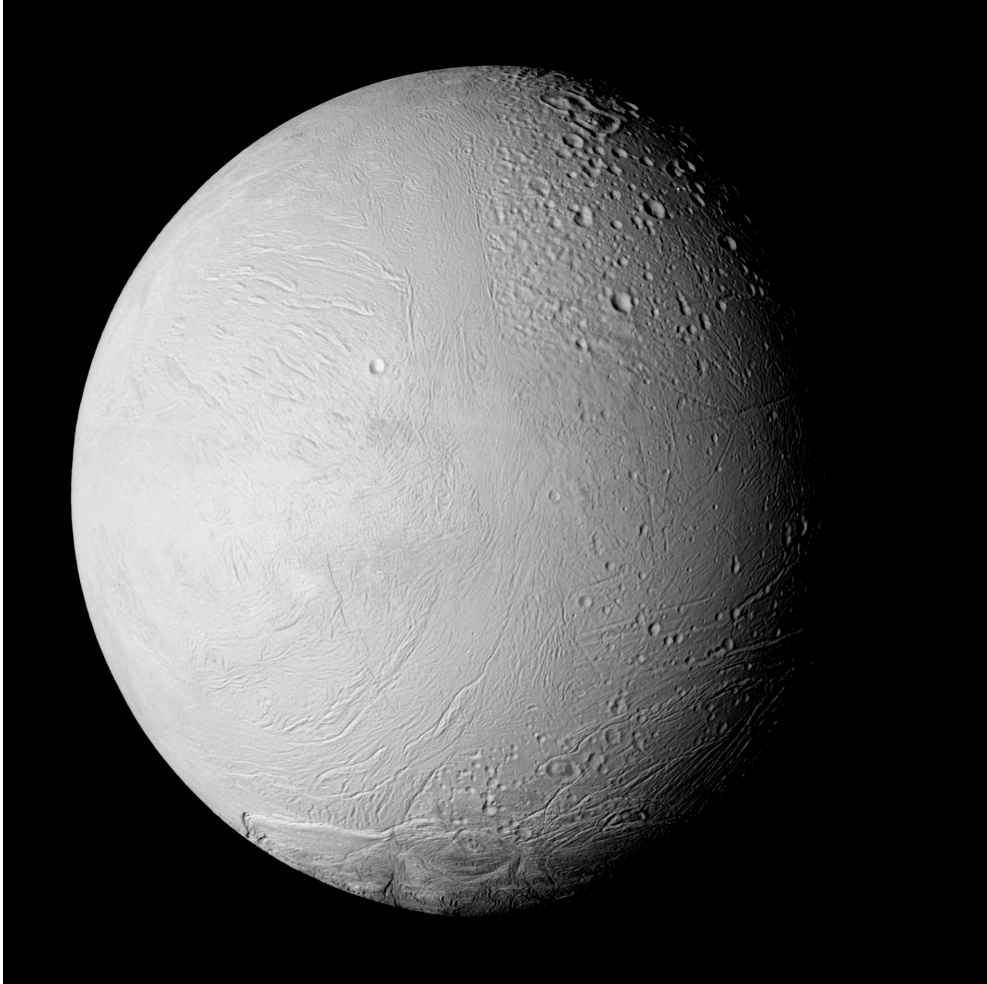
Figure 1.18: The leading hemisphere of Enceladus. - The mosaic image obtained by Cassini ISS in 2009 shows the transition from young south polar region to older terrains to the north. Source: NASA Planetary PhotoJournal

As indicated by Cassini observations, Enceladus' plume is also the dominating source of E ring dust particles. The Cassini dust detector observed during the Cassini's Enceladus flyby on 14 July 2005 that, the dust impact rate occurred 1 minute earlier than the close approach, which indicates a local dust source within the south polar region of Enceladus Spahn *et al.* (2006). Considering icy grains formation by direct condensation of the water vapor in tiger stripe fractures, the plume model by Schmidt *et al.* (2008) convincingly explained the observed gas–dust velocity difference and the

E ring particle size distribution. Furthermore, based on the model, the authors suggested that the source temperature is above 260K and indicative of liquid water as the source of Enceladus' plume.
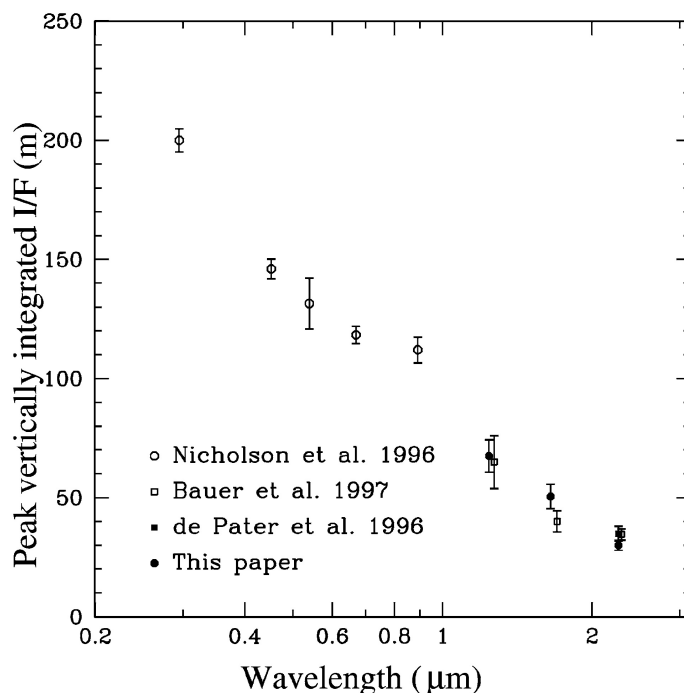
Figure 1.19: The photometric spectrum of Saturn's E ring. - The intensity of E ring from optical to infrared wavelength based on various observations. The blue color of E ring is shown by its low infrared intensity compared to those in the optical wavelength. The figure is from de Pater *et al.* (2004).

While most of E ring particles are found to be composed of water ice (Hillier *et al.*, 2007; Postberg *et al.*, 2008), Postberg *et al.* (2009b) identified a minor population (about 6%) which is rich in NaCl and $NaHCO_3$. The sodium compound found in E ring particles provides a strong evidence of a liquid water plume source, as indicated by the plume model. The composition of sodium–rich particles agrees with those predicted by Zolotov (2007) for a sub–surface ocean in contact with warm rock.

Besides the grain composition, it is also found out that the E ring extends farther away till Titan's orbit (Srama *et al.*, 2006). The dust charge measurements showed a flip in charge polarity close to Rhea's orbit (Kempf *et al.*, 2006). Particles are charged few volts negatively inside Rhea's orbit and turn few volts positively outwards.
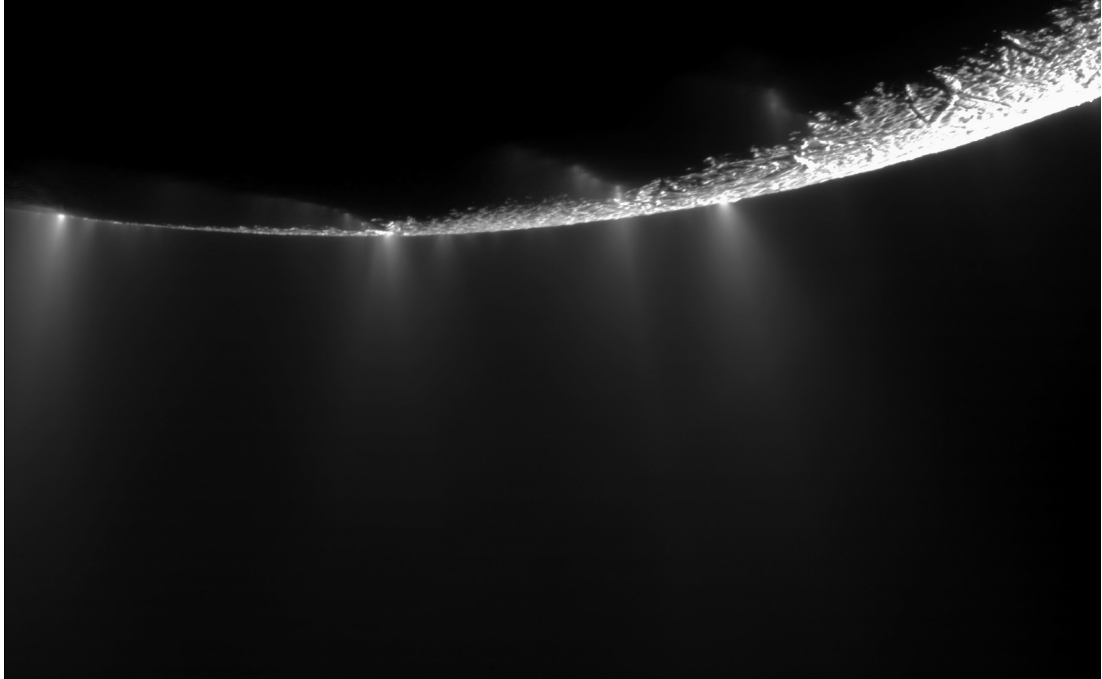
Figure 1.20: Enceladus' plume spotted during the flyby on November, 2009. - Erupting jets along tiger–stripes in south polar region of Enceladus, imaged by Cassini ISS on Nov. 21, 2009. From right to left, jets trace out Alexandria, Cairo, Baghdad, and Damascus sulci (sub–parallel furrows and ridges) named after cities in The Arabian Nights. Source: CICLOPS

1.4   Cassini–Huygens Mission

1.4.1   Overview

Cassini-Huygens is a joint NASA/ESA/ASI mission to study the Saturnian system. It consists of two elements: the Cassini orbiter and the Huygens probe. The orbiter is named after the Italian-French astronomer Giovanni Domenico Cassini. The Huygens probe is named for the Dutch astronomer Christiaan Huygens who discovered the largest moon of Saturn – Titan.

Launched on October 15, 1997, the spacecraft went through a long interplanetary journey in order to perform gravitation assist–flybys (figure 1.21). In December 2000 a flyby at Jupiter provided the spacecraft a final acceleration and leaded it towards Saturn. The Saturn Orbit Insertion (SOI) of the Cassini spacecraft took place on July 1st, 2004. About half a year later, the Huygens probe was separated from the Cassini spacecraft and reached the moon Titan on January 14, 2005.

The main objectives of the Cassini–Huygens mission are the exploration of Titan, the magnetosphere, icy satellites, the ring system, and Saturn itself. The on–board imaging instruments cover wavelength range from the ultraviolet to the infrared and with spectral capability which helps to study the structure as well as to acquire the compositional information of the Saturnian environment. The field and particle instruments are capable to measure the magnetic field, the plasma, the neutral gas, and the dust particles to help increasing our understanding of the interactions between dusty rings, moons, and the magnetosphere.
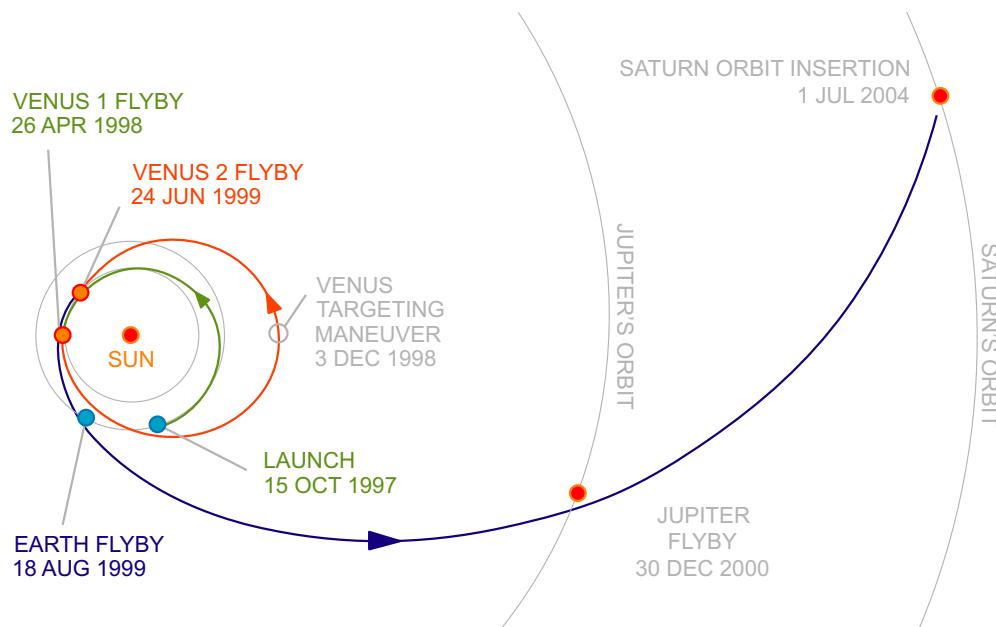
Figure 1.21: The interplanetary trajectory of the Cassini-Huygens spacecraft. - Source: en.wikipedia

1.4.2 Cosmic Dust Analyser

The Cosmic Dust Analyser (CDA) is the dust instrument aboard the Cassini spacecraft (Srama *et al.*, 2004, figure 1.22). CDA consists of two independent subsystems: the High Rate Detector (HRD) and the Dust Analyser (DA). The HRD is designed for monitoring the flux of micron–sized grains in high dust density environment. As it is too insensitive for stream–particle impacts, the HRD measurements are not relevant here. The DA is an impact ionization type dust detector and is capable to measure the velocity, the mass, the charges, and the chemical composition of each single impinging

dust grain. It is composed of following detectors: a charge sensing unit (QP detector) as the entrance grids of the instrument, an Impact Ionisation Detector (IID) similar to Ulysses/Galileo detectors, and a time-of-flight (TOF) mass spectrometer (Mass Analyser, MA). To integrate the TOF mass spectrometer into the DA, the IID target is divided into two concentric hemispherical targets: an inner rhodium target of 16 cm in diameter (Chemical Analyser Target – CAT) and a large outer gold target of 41 cm in diameter (Impact Ionisation Target, IIT). The angular field of view (FOV) of the DA is $\pm 45°$ while the CAT FOV is only $\pm 28°$.

Figure 1.22: The Cosmic Dust Analyser. - Source: CDA team

As a dust particle impinges into the DA aperture, it will first pass through the entrance grids in front of the instrument. However, the charge carried on a stream particle is far less than the detection threshold of the charge sensor (10^{-15} fC). The QP signal is therefore negligible in this work. Afterward, the particle may collide with either the

inner rhodium target (CAT) or the outer gold target (IIT). The collision will transform the particle and the target material at least partially into impact plasma whose amount and expansion time scale provide information about the impactor's mass and impact speed. To achieve this, the plasma generated on the impact target is separated into its constituents by an electric field between the targets and the ion grid. The plasma is then collected by individual electrodes and monitored by attached charge amplifiers (plasma electrons impact target, ions - ion grid). A DA measurement is started either when the impact charge collected in at least one of the electrodes exceeds a pre–set IID threshold or when the strength of a TOF mass line measured at the MA's multiplier in the center of the instrument exceeds the MA threshold. In normal cases, an impact event consists of one target signal (QC for CAT impacts or QT for IIT impacts) and one ion grid signal (QI). Once the dust grain hits on the CAT, the positive ions in the impact plasma will then be accelerated toward the MA and generate a TOF mass spectrum.

1.5 Messages from Stream Particles

1.5.1 Ionian Volcano Activities and its Influence on Jupiter's Magnetosphere

Based on 6 years of Galileo stream particle measurements, Krüger *et al.* (2003) derived the dust production rate and correlated it with Ionian volcanic activities, such as the surface change and plume sighting. Shown in figure 1.23, it seemed that the stream particle emission is correlated to the Pele–type plume activities. In particular, a two to three order of magnitude enhancement of dust production rate took place during orbits G28 and G29, which is about the same time of Cassini's Jupiter flyby.

The UV emission from Io's plasma torus observed by Cassini UVIS during this period showed a significant time variability. Moreover, the UV emission was found to be correlated to the dust production rate derived by Krüger *et al.* (2003). To match the UV observation, a plasma chemistry model had been performed and suggested that the neutral gas produced from Io (presumed to be of volcanic origin) had changed from 1.8 ton/s to 0.7 ton/s during the observation period (Delamere *et al.*, 2004). The variation of plasma properties along with the changing neutral production rate were also calculated (figure 1.24).

Adopting plasma conditions modeled by Delamere *et al.* (2004), the grain charging can be calculated by using equations described in section 1.2.3. With secondary electron emission parameters given by Kanaya *et al.* (1978) for NaCl ($\delta_M = 6.5$, $E_M = 650\,\text{eV}$), the equilibrium potentials at Io's vicinity on day 275 of 2000 and day 14 of 2001 are +1.9 V and -3.6 V, respectively. As mentioned earlier, only particles with positive charges can gain energy from $\mathbf{E}_c$ and escape the system. During the high neutral gas production period (day 220 to 300 in 2000), dust particles in the IPT tended to be charged positively. In contrast, after year 2000 when the "activity" ceased, dust

particles inside the IPT tended to be charged negatively. The variation of charging condition qualitatively agrees with the dust measurement by Galileo (Krüger *et al.*, 2003) as well as CDA observations (see section 4.2). In other words, the change of plasma conditions (especially the electron temperature) probably acted as a switch of stream particle activity. Note that the maximum dust emission rate reached few hundreds kilogram per second, which is comparable to the ion production rate. The subsequent interaction of stream particles and the magnetosphere could be significant. This simple calculation shows a complicated connection between Ionian volcanic activity, neutral production, plasma chemistry, and the stream particle activity. Further studies regarding time variability of stream particle activities are necessary.
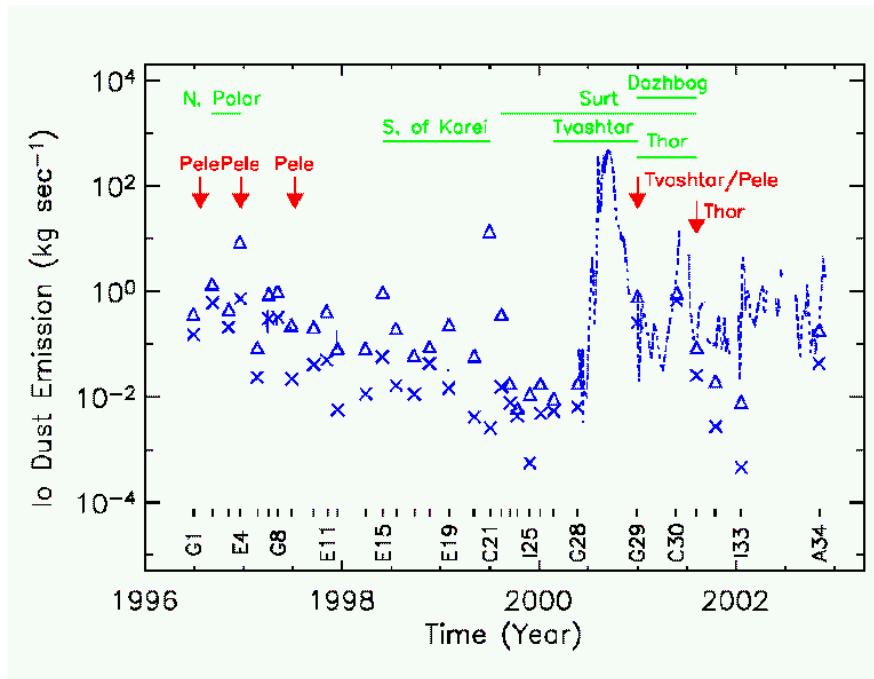
Figure 1.23: Dust emission rate of Io between 1996 and 2003. - Triangles and crosses denote the maxima and minima derived from measurements in the distance range $13 < d < 30\,R_J$, respectively. The dashed line is for the G28 orbit in the range $30 < d < 280\,R_J$, dotted lines show the remaining orbits with $30 < d < 400\,R_J$. Thick horizontal bars indicate periods when large-area surface changes due to giant plume eruptions occurred on Io, arrows indicate individual plume sightings. Source: (Krüger *et al.*, 2003, Galileo Dust Homepage)
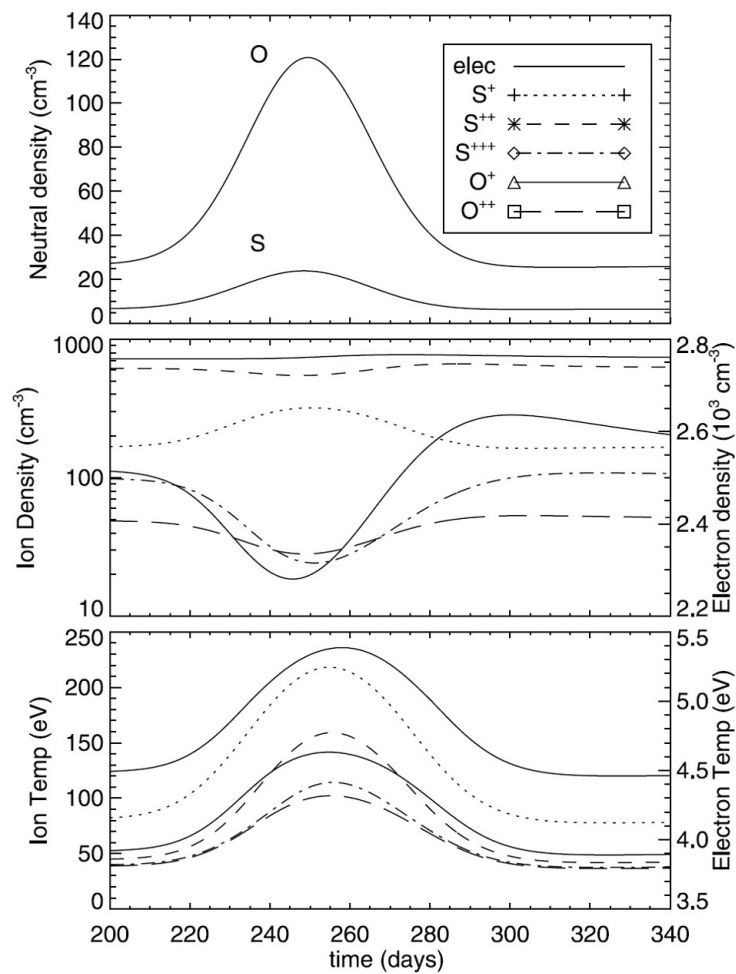
Figure 1.24: Variation of plasma properties of IPT between day 200 and 340 of 2000. - The IPT plasma chemistry model based on Cassini UVIS observation (Delamere *et al.*, 2004).

1.5.2 Radiolysis of Dust Grains and Cosmochemical Implications for Enceladus

One of the interesting fields regarding cosmic dust is the interaction between the plasma and the icy surface. For instance, surface chemistry on the grain surface in the cold, dense molecular cloud had been found to be much more important than the gas phase reactions. In the Saturnian system, moons and ring particles are found to be composed of almost pure water ice and therefore serve as a natural laboratory for studying the icy surface radiolysis.

As proposed by Johnson *et al.* (2008); Jurac *et al.* (2001), it is believed that the lifetime of E ring dust grains is limited by the plasma sputtering. Before the discovery of the active plume of Enceladus, by comparing the neutral gas observations and the amount of sputtered products from E ring particles, Jurac & Richardson (2005) remarkably predicted a "missing" source located at Enceladus' orbit with production rate of 10^{28} molecule per second, which fits to Cassini observations (Waite *et al.*, 2006).

Because of the high production rate of Enceladus, it is hard to distinguish the relatively small neutral gas produced by E ring particles (via sputtering) from the extended Enceladus neutral torus. However, the molecule oxygen is known to form pre–dominantly from the radiolytic decomposition of ice rather than gas phase reactions. Therefore, O_2^+ in the Saturnian magnetosphere can be a tracer of radiolysis of icy surfaces (Mauk *et al.*, 2009).

O_2 can be produced via electronic excitation of water ice by low energy electrons ($< 100\,eV$), UV photons, and fast ions ($\sim MeV$) (Johnson *et al.*, 2005; Sieger *et al.*, 1998). At very low temperature, the reaction triggered by incident particles or photons may not be complete since the radicals can be stored for a long period of time. Using the electron beam with the ice sample, Sieger *et al.* (1998) nicely demonstrated a two–step (precursor–mediated) sputtering process of molecular oxygen production from the icy surface.

Based on Cassini Plasma Spectrometer (CAPS) measurements, the analysis by Martens *et al.* (2008) showed that the abundance ratio between O_2^+ and water group ions is about 0.3% inside $8\,R_S$ and increases significantly between 8 to $10\,R_S$ with a dip around Rhea's orbit (figure 1.25). Considering that the surface area of Rhea is much larger than the surface of E ring grains, the authors suggested that O_2 molecules produced from the surface of Rhea and its tentative ring (Jones *et al.*, 2008) are the source of observed O_2^+.

It had been found in the Jovian system that the icy moons, such as Europa and Ganymede, possess tenuous O_2 atmospheres. After produced by radiolytic processes on the surface, compared to H_2, the relatively heavy O_2 molecules are more difficult to escape from the gravity field. From Shematovich (2006), the energy distribution of

sputtered O_2 is:

$$f(E) \sim \frac{0.015\,\text{eV}}{(E + 0.015\,\text{eV})^2} \tag{1.8}$$

To escape Rhea's gravity, the newly formed O_2 molecule requires $0.067\,\text{eV}$. Based on Eq. 1.8, less then 20% of O_2 can enter the magnetosphere. In contrast, more than 80% of H_2O sputtered from the surface are capable to escape. It is likely that the dilution rather than the absorption proposed by Martens *et al.* (2008) is responsible for the O_2^+/W^+ dip at the vicinity of Rhea. On top of that, beyond $7\,R_S$ the plasma electron in Saturnian magnetosphere is above the O_2 production threshold of $10\pm2\,\text{eV}$ (Orlando & Sieger, 2003) and agrees with the rise of the O_2^+/W^+ ratio. Since the O_2 produced from E ring particles is released freely into the magnetosphere, the O_2^+ observed at this distance may be indicative of local O_2 production from E ring dust grains.
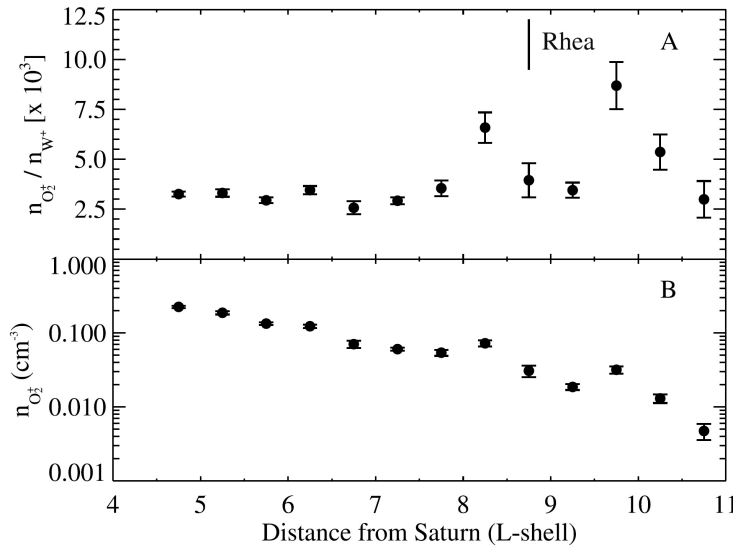
Figure 1.25: Cassini O_2^+ observation result. - The figure from Martens *et al.* (2008) shows (a) the ratio between O_2^+ and water group ions and (b) the density of O_2^+ molecule.

Further away in the middle magnetosphere ($>9\,R_S$), a recent report by Melin *et al.* (2009), based on atomic oxygen emission observation suggested that a slow source of oxygen is needed to explain the observed profile (figure 1.26). As noted earlier, CDA measurements showed that the Saturnian E ring extends from $3\,R_S$ to Titan's orbit at $20\,R_S$ (Srama *et al.*, 2006), which may be sufficient to maintain a weak source via sputtering at the outer magnetosphere of Saturn. Using the measured or modeled E ring density profiles for the sputtering calculation is promising a target of future research.

Regarding the composition of Saturnian stream particles, an updated detail analysis of CDA mass spectra is discussed in section 5.4. In contrast to E ring grains, stream particles have drastically enhanced the siliceous component. Considering the difference in sputtering yield (section 1.2.4 and 5.5), our ejection model suggests that the Saturnian stream particles are dynamically–old E ring particles. In other words, the siliceous material found in the mass spectra of stream particles is probably of Enceladus origin.
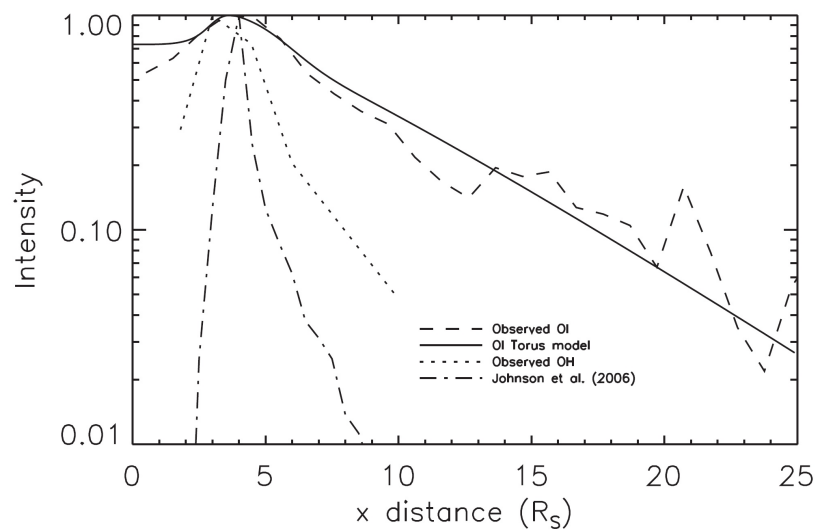
Figure 1.26: Atomic oxygen and hydroxyl profiles derived from HST and Cassini UVIS observations - The figure from Melin *et al.* (2009) shows the difference between observations and modeling (dash–dot) of neutral gas in Saturn's magnetosphere.

However, the lack of metal in stream particles' spectra suggests that the Saturnian stream particles are probably composed of SiO_2 with only a small fraction of metal bearing minerals. It is likely to form metal depleted silica in the low pH solution with mild temperature ($<200°$C) (McAdam *et al.*, 2008). However, the model by Zolotov (2007) shows that the pH value of probable sub–surface ocean of Enceladus is around 8 to 11, which makes this concept less possible.

Early short–lived radioisotopes (SLRI) activities may contribute to the formation of metal–free silica. On one hand, radiolysis of aqueous solutions is an efficient method for the reduction of metal ions (C. M. Doudna, 2003; Dukes & Baragiola, 2010), the radiation from the decay of SLRI not only melted the ice layer but also remove the metal from the siliceous minerals. On the other hand, through the hydrothermal systems

triggered by SLRI (Glein *et al.*, 2008; Matson *et al.*, 2007), reactions such as:

$$3Fe_2SiO_4 + 2H_2O = 2Fe_3O_4 + 3SiO_2 + 2H_2 \tag{1.9}$$

may take place and produce nanoscale SiO_2 particles. Since these particles are so tiny, they can be easily entrained in flow and be distributed to the upper ice crust. In tiger stripes fractures, these tiny impurities may be lifted by the water vapor and serve as condensation cores of icy dust grains.

Summary References

BAGENAL, F. (2007). The magnetosphere of Jupiter: Coupling the equator to the poles. *Journal of Atmospheric and Solar-Terrestrial Physics*, **69**, 387–402. 18

BAGUHL, M., GRÜN, E., LINKERT, G., LINKERT, D. & SIDDIQUE, N. (1993). Identification of small dust impacts in the ULYSSES dust detector data. *Planetary and Space Science*, **41**, 1085–1098. 4, 48

BAUER, J., LISSAUER, J.J. & SIMON, M. (1997). Edge-on observations of Saturn's E and G ring in the near-IR. *Icarus*, **125**, 440–445. 22

BECKMANN, U. (2008). *Dynamik von Sataubteichen in Saturns E–Ring*. Ph.D. thesis, University Heidelberg. 8, 76, 99, 116

C. M. DOUDNA, M.F.B.F.D.B.A.T.T.D.L.D.S.C.A.J.T. (2003). Radiolytic synthesis of bimetallic agpt nanoparticles with a high aspect ratio. *The Journal of Physical Chemistry B*, **107 (13)**, 2966–2970. 35

COLANGELI, L., LOPEZ-MORENO, J.J., PALUMBO, P., RODRIGUEZ, J., COSI, M., CORTE, V.D., ESPOSITO, F., FULLE, M., HERRANZ, M., JERONIMO, J.M., LOPEZ-JIMENEZ, A., EPIFANI, E.M., MORALES, R., MORENO, F., PALOMBA, E. & ROTUNDI, A. (2007). The Grain Impact Analyser and Dust Accumulator (GIADA) Experiment for the Rosetta Mission: Design, Performances and First Results. *Space Science Reviews*, **128**, 803–821. 3

DE PATER, I., MARTIN, S.C. & SHOWALTER, M.R. (2004). Keck near-infrared observations of Saturn's E and G rings during Earth's ring plane crossing in August 1995. *Icarus*, **172**, 446–454. 22, 26

DELAMERE, P.A., STEFFL, A. & BAGENAL, F. (2004). Modeling temporal variability of plasma conditions in the Io torus during the Cassini era. *Journal of Geophysical Research (Space Physics)*, **109**, 10216. 30, 32, 78

DIKAREV, V., PREUSS, O., SOLANKI, S., KRÜGER, H. & KRIVOV, A. (2009). The Local Dust Foregrounds in the Microwave Sky. I. Thermal Emission Spectra. *Astrophys. J.*, **705**, 670–682. 4

SUMMARY REFERENCES

DUKES, C.A. & BARAGIOLA, R.A. (2010). Effect of Water on the Surface Composition of Irradiated Minerals. **41**, 2157. 35

GEISSLER, P.E. & MCMILLAN, M.T. (2008). Galileo observations of volcanic plumes on Io. *Icarus*, **197**, 505–518. 13, 20

GEISSLER, P.E., MCEWEN, A.S., IP, W., BELTON, M.J.S., JOHNSON, T.V., SMYTH, W.H. & INGERSOLL, A.P. (1999). Galileo Imaging of Atmospheric Emissions from Io. *Science*, **285**, 870–874. 18, 20

GLEIN, C.R., ZOLOTOV, M.Y. & SHOCK, E.L. (2008). The oxidation state of hydrothermal systems on early Enceladus. *Icarus*, **197**, 157–163. 36

GRAPS, A., GRÜN, E., SVEDHEM, H., KRÜGER, H., HORÁNYI, M., HECK, A. & LAMMERS, S. (2000). Io as a source of the jovian dust streams. *Nature*, **405**, 48–50. 6, 7, 68, 77

GRÜN, E., ZOOK, H., BAGUHL, M., BALOGH, A., BAME, S., FECHTIG, H., FORSYTH, R., HANNER, M., HORANYI, M., KISSEL, J., LINDBLAD, B.A., LINKERT, D., LINKERT, G., MANN, I., MCDONNEL, J., MORFILL, G., PHILLIPS, J., POLANSKEY, C., SCHWEHM, G., SIDDIQUE, N., STAUBACH, P., SVESTKA, J. & TAYLOR, A. (1993). Discovery of Jovian dust streams and interstellar grains by the Ulysses spacecraft. *Nature*, **362**, 428–430. 4, 5, 15, 47, 48, 63, 64, 67, 77

GRÜN, E., BAGUHL, M., HAMILTON, D., RIEMANN, R., ZOOK, H., DERMOTT, S., FECHTIG, H., GUSTAFSON, B., HANNER, M., HORÁNYI, M., KHURANA, K., KISSEL, J., KIVELSON, M., LINDBLAD, B.A., LINKERT, D., LINKERT, G., MANN, I., MCDONNEL, J., MORFILL, G., POLANSKEY, C., SCHWEHM, G. & SRAMA, R. (1996). Constraints from galileo observations on the origin of jovian dust streams. *Nature*, **381**, 395–398. 15, 48, 63

GRÜN, E., KRÜGER, H., GRAPS, A., HAMILTON, D., HECK, A., LINKERT, G., DERMOTT, S., FECHTIG, H., GUSTAFSON, B., HANNER, M., HORÁNYI, M., KISSEL, J., LINDBLAD, B., LINKERT, D., MANN, I., MCDONNEL, J., MORFILL, G., POLANSKEY, C., SCHWEHM, G. & SRAMA, R. (1998). Galileo observes electromagnetically coupled dust in the jovian magnetosphere. *J. Geophys. Res.*, **103**, 20 011–20 022. 6, 68, 77

GRÜN, E., KEMPF, S., KRÜGER, H., LANDGRAF, M. & SRAMA, R. (2001). Dust astronomy: a new approach to the study of interstellar dust. In B. Warmbein, ed., *Proceedings of the Meteoroids 2001 Conference, 6 - 10 August 2001, Kiruna, Sweden*, ESA SP-495, 651–662, ESA Publications Division, Noordwijk. 4, 76

HAMILTON, D. & BURNS, J. (1993). Ejection of dust from jupiter's gossamer ring. *Nature*, **364**, 695–699. 5, 47, 48, 57, 64, 68, 77

HANSEN, C.J., ESPOSITO, L., STEWART, A.I.F., COLWELL, J., HENDRIX, A., PRYOR, W., SHEMANSKY, D. & WEST, R. (2006). Enceladus' Water Vapor Plume. *Science*, **311**, 1422–1425. 22, 96

HILLIER, J.K., GREEN, S.F., MCBRIDE, N., SCHWANETHAL, J.P., POSTBERG, F., SRAMA, R., KEMPF, S., MORAGAS-KLOSTERMEYER, G., MCDONNELL, J.A.M. & GRÜN, E. (2007). The composition of Saturn's E ring. *Mon. Not. Roy. Astron. Soc.*, **377**, 1588–1596. 8, 26, 49, 79, 109

HINSON, D.P., KLIORE, A.J., FLASAR, F.M., TWICKEN, J.D., SCHINDER, P.J. & HERRERA, R.G. (1998). Galileo radio occultation measurements of Io's ionosphere and plasma wake. *J. Geophys. Res.*, **103**, 29343–29358. 13

HORÁNYI, M. (2000). Dust streams from Jupiter and Saturn. *Phys. of Plasmas*, **7**, 3847–3850. 7, 49, 57, 68, 78, 93

HORÁNYI, M., MORFILL, G. & GRÜN, E. (1993). Mechanism for the acceleration and ejection of dust grains from Jupiter's magnetosphere. *Nature*, **363**, 144–146. 5, 57, 68, 77

HORÁNYI, M., JUHÁSZ, A. & MORFILL, G.E. (2008). Large-scale structure of Saturn's E-ring. *Geophys. Res. Lett.*, **35**, 4203. 8, 76, 116

HUMES, D.H., O'NEAL, R.L., KINARD, W.H. & ALVAREZ, J.M. (1980). Impact of Saturn ring particles on Pioneer 11. *Science*, **207**, 443. 3

IP, W.H. (1996). The dust halo of Io. *Geophys. Res. Lett.*, **23**, 3671–3674. 14

JOHNSON, R.E., COOPER, P.D., QUICKENDEN, T.I., GRIEVES, G.A. & ORLANDO, T.M. (2005). Production of oxygen by electronically induced dissociations in ice. *J. Chem. Phys.*, **123**, 184715. 33

JOHNSON, R.E., SMITH, H.T., TUCKER, O.J., LIU, M., BURGER, M.H., SITTLER, E.C. & TOKAR, R.L. (2006). The Enceladus and OH Tori at Saturn. *Astrophys. J. Lett.*, **644**, L137–L139. 23

JOHNSON, R.E., FAMÁ, M., LIU, M., BARAGIOLA, R.A., SITTLER, E.C. & SMITH, H.T. (2008). Sputtering of ice grains and icy satellites in Saturn's inner magnetosphere. *Planet. Space Sci.*, **56**, 1238–1243. 16, 33, 76, 95, 117

JONES, G.H., ROUSSOS, E., KRUPP, N., BECKMANN, U., COATES, A.J., CRARY, F.J., DANDOURAS, I., DIKAREV, V.V., DOUGHERTY, M.K., GARNIER, P., HANSEN, K.C., HENDRIX, A.R., HOSPODARSKY, G.B., JOHNSON, R.E., KEMPF, S., KHURANA, K.K., KRIMIGIS, S.M., KRÜGER, H., KURTH, W.S., LAGG, A., MCANDREWS, H.J., MITCHELL, D., PARANICAS, C., POSTBERG, F., RUSSELL, C.T., SAUR, J., SPAHN, F., STROBEL, D.F., TOKAR, R.L., WAHLUND, J.E., WILSON, R.J., WOCH, J. & YOUNG, D.T. (2008). The dust halo of saturn's largest icy moon: Evidence of rings at rhea? *Science*, **319**, 1380–1384, subm. 33

JURAC, S. & RICHARDSON, J.D. (2005). A self-consistent model of plasma and neutrals at Saturn: Neutral cloud morphology. *Journal of Geophysical Research (Space Physics)*, **110**, 9220. 33

SUMMARY REFERENCES

JURAC, S., JOHNSON, R.E. & RICHARDSON, J.D. (2001). Saturn's E Ring and Production of the Neutral Torus. *Icarus*, **149**, 384–396. 14, 15, 33, 76, 95, 107, 117

KANAYA, K., ONO, S. & ISHIGAKI, F. (1978). Secondary electron emission from insulators. *Journal of Physics D Applied Physics*, **11**, 2425–2437. 30, 100, 101

KEMPF, S., SRAMA, R., HORÁNYI, M., BURTON, M., HELFERT, S., MORAGAS-KLOSTERMEYER, G., ROY, M. & GRÜN, E. (2005a). High-velocity streams of dust originating from Saturn. *Nature*, **433**, 289–291. 7, 8, 47, 48, 49, 57, 61, 62, 64, 68, 78, 86

KEMPF, S., SRAMA, R., POSTBERG, F., BURTON, M., GREEN, S.F., HELFERT, S., HILLIER, J.K., MCBRIDE, N., MCDONNELL, J.A.M., MORAGAS-KLOSTERMEYER, G., ROY, M. & GRÜN, E. (2005b). Composition of saturnian stream particles. *Science*, **307**, 1274–1276. 8, 13, 49, 52, 68, 79, 83, 95, 101, 109, 111, 114, 115

KEMPF, S., BECKMANN, U., SRAMA, R., HORANYI, M., AUER, S. & GRÜN, E. (2006). The electrostatic potential of E ring particles. *Planet. Space Sci.*, **54**, 999–1006. 26, 95, 96, 97, 99, 100

KRÜGER, H., GEISSLER, P., HORÁNYI, M., GRAPS, A., KEMPF, S., SRAMA, R., MORAGAS-KLOSTERMEYER, G., MOISSL, R., JOHNSON, T. & GRÜN, E. (2003). Jovian dust streams: A monitor of io's volcanic plume activity. *Geophys. Res. Let.*, **30**, 3–1. 14, 30, 31, 78

MANN, I., KIMURA, H., BIESECKER, D.A., TSURUTANI, B.T., GRÜN, E., MCKIBBEN, R.B., LIOU, J., MACQUEEN, R.M., MUKAI, T., GUHATHAKURTA, M. & LAMY, P. (2004). Dust Near The Sun. *Space Science Reviews*, **110**, 269–305. 3

MARTENS, H.R., REISENFELD, D.B., WILLIAMS, J.D., JOHNSON, R.E. & SMITH, H.T. (2008). Observations of molecular oxygen ions in Saturn's inner magnetosphere. *Geophys. Res. Lett.*, **35**, 20103. 33, 34, 117, 118

MATSON, D.L., CASTILLO, J.C., LUNINE, J. & JOHNSON, T.V. (2007). Enceladus' plume: Compositional evidence for a hot interior. *Icarus*, **187**, 569–573. 36

MAUK, B.H., HAMILTON, D.C., HILL, T.W., HOSPODARSKY, G.B., JOHNSON, R.E., PARANICAS, C., ROUSSOS, E., RUSSELL, C.T., SHEMANSKY, D.E., SITTLER, E.C. & THORNE, R.M. (2009). *Fundamental Plasma Processes in Saturn's Magnetosphere*. 33

MCADAM, A.C., ZOLOTOV, M.Y., MIRONENKO, M.V. & SHARP, T.G. (2008). Formation of Martian Silica-rich Deposits Through Rock Alteration: A Theoretical Assessment. **39**, 2371. 35

MELIN, H., SHEMANSKY, D.E. & LIU, X. (2009). The distribution of atomic hydrogen and oxygen in the magnetosphere of Saturn. *Planet. Space Sci.*, **57**, 1743–1753. 34, 35, 96, 117

MORFILL, G.E., GRÜN, E. & JOHNSON, T.V. (1980). Dust in Jupiter's magnetosphere: Physical processes. *Planet. Space Sci.*, **28**, 1087–1100. 5

MOTT-SMITH, H.M. & LANGMUIR, I. (1926). The Theory of Collectors in Gaseous Discharges. *Physical Review*, **28**, 727–763. 11

NICHOLSON, P.D., SHOWALTER, M.R. & DONES, L. (1996). Observations of Saturn's ring-plane crossing in August and November. *Science*, **272**, 509–516. 22

ORLANDO, T. & SIEGER, M.T. (2003). The role of electron-stimulated production of O2 from water ice in the radiation processing of outer solar system surfaces. *Surface Science*, **528**, 1–7. 34, 118

PILCHER, C.B., CHAPMAN, C.R., LEBOFSKY, L.A. & KIEFFER, H.H. (1970). Saturu's Rings: Identification of Water Frost. *Science*, **167**, 1372–1373. 8, 79

POSTBERG, F., KEMPF, S., SRAMA, R., GREEN, S.F., HILLIER, J.K., MCBRIDE, N. & GRÜN, E. (2006). Composition of jovian dust stream particles. *Icarus*, **183**, 122–134. 7, 13, 49, 68, 73, 78, 81, 111

POSTBERG, F., KEMPF, S., HILLIER, J.K., SRAMA, R., GREEN, S.F., MCBRIDE, N. & GRÜN, E. (2008). The E-ring in the vicinity of Enceladus II: Signatures of Enceladus in the elemental composition of E-ring particles. *Icarus*, **193**, 438–454. 26, 49, 95, 115

POSTBERG, F., KEMPF, S., ROST, D., STEPHAN, T., SRAMA, R., TRIELOFF, M., MOCKER, A. & GOERLICH, M. (2009a). Discriminating contamination from particle components in spectra of Cassini's dust detector CDA. *Planet. Space Sci.*, **57**, 1359–1374. 8, 82, 109, 111, 112, 114, 115

POSTBERG, F., KEMPF, S., SCHMIDT, J., BRILLIANTOV, N., BEINSEN, A., ABEL, B., BUCK, U. & SRAMA, R. (2009b). Sodium salts in E-ring ice grains from an ocean below the surface of Enceladus. *Nature*, **459**, 1098–1101. 26, 81, 112

RYMER, A.M., MAUK, B.H., HILL, T.W., ANDRÉ, N., MITCHELL, D.G., PARANICAS, C., YOUNG, D.T., SMITH, H.T., PERSOON, A.M., MENIETTI, J.D., HOSPODARSKY, G.B., COATES, A.J. & DOUGHERTY, M.K. (2009). Cassini evidence for rapid interchange transport at Saturn. *Planet. Space Sci.*, **57**, 1779–1784. 23

SCHAEFER, L. & FEGLEY, B. (2005). Alkali and halogen chemistry in volcanic gases on Io. *Icarus*, **173**, 454–468. 13, 14

SCHMIDT, J., BRILLIANTOV, N., SPAHN, F. & KEMPF, S. (2008). Slow dust in Enceladus' plume from condensation and wall collisions in tiger stripe fractures. *Nature*, **451**, 685–688. 25

SHEMATOVICH, V.I. (2006). Stochastic models of hot planetary and satellite coronas: Atomic oxygen in Europa's corona. *Solar System Research*, **40**, 175–190. 33

SHOWALTER, M.R., CUZZI, J.N. & LARSON, S.M. (1991). Structure and particle properties of Saturn's E ring. *Icarus*, **94**, 451–473. 22, 76

SIEGER, M.T., SIMPSON, W.C. & ORLANDO, T.M. (1998). Production of O_2 on icy satellites by electronic excitation of low-temperature water ice. *Nature*, **394**, 554–556. 33, 117

SITTLER, E.C., ANDRE, N., BLANC, M., BURGER, M., JOHNSON, R.E., COATES, A., RYMER, A., REISENFELD, D., THOMSEN, M.F., PERSOON, A., DOUGHERTY, M., SMITH, H.T., BARAGIOLA, R.A., HARTLE, R.E., CHORNAY, D., SHAPPIRIO, M.D., SIMPSON, D., MCCOMAS, D.J. & YOUNG, D.T. (2008). Ion and neutral sources and sinks within Saturn's inner magnetosphere: Cassini results. *Planet. Space Sci.*, **56**, 3–18. 23, 96

SPAHN, F., SCHMIDT, J., ALBERS, N., HÖRNING, M., MAKUCH, M., SEISS, M., KEMPF, S., SRAMA, R., DIKAREV, V., HELFERT, S., MORAGAS-KLOSTERMEYER, G., KRIVOV, A.V., SREMČEVIĆ, M., TUZZOLINO, A.J., ECONOMOU, T. & GRÜN, E. (2006). Cassini Dust Measurements at Enceladus and Implications for the Origin of the E Ring. *Science*, **311**, 1416–1418. 22, 25

SPENCER, J.R., STERN, S.A., CHENG, A.F., WEAVER, H.A., REUTER, D.C., RETHERFORD, K., LUNSFORD, A., MOORE, J.M., ABRAMOV, O., LOPES, R.M.C., PERRY, J.E., KAMP, L., SHOWALTER, M., JESSUP, K.L., MARCHIS, F., SCHENK, P.M. & DUMAS, C. (2007). Io Volcanism Seen by New Horizons: A Major Eruption of the Tvashtar Volcano. *Science*, **318**, 240–. 20

SRAMA, R., AHRENS, T.J., ALTOBELLI, N., AUER, S., BRADLEY, J.G., BURTON, M., DIKAREV, V.V., ECONOMOU, T., FECHTIG, H., GÖRLICH, M., GRANDE, M., GRAPS, A., GRÜN, E., HAVNES, O., HELFERT, S., HORANYI, M., IGENBERGS, E., JESSBERGER, E.K., JOHNSON, T.V., KEMPF, S., KRIVOV, A.V., KRÜGER, H., MOCKER-AHLREEP, A., MORAGAS-KLOSTERMEYER, G., LAMY, P., LANDGRAF, M., LINKERT, D., LINKERT, G., LURA, F., MCDONNELL, J.A.M., MÖHLMANN, D., MORFILL, G.E., MÜLLER, M., ROY, M., SCHÄFER, G., SCHLOTZHAUER, G., SCHWEHM, G.H., SPAHN, F., STÜBIG, M., SVESTKA, J., TSCHERNJAWSKI, V., TUZZOLINO, A.J., WÄSCH, R. & ZOOK, H.A. (2004). The Cassini Cosmic Dust Analyzer. *Space Science Reviews*, **114**, 465–518. 7, 28, 51, 76

SRAMA, R., KEMPF, S., MORAGAS-KLOSTERMEYER, G., HELFERT, S., AHRENS, T.J., ALTOBELLI, N., AUER, S., BECKMANN, U., BRADLEY, J.G., BURTON, M., DIKAREV, V.V., ECONOMOU, T., FECHTIG, H., GREEN, S.F., GRANDE, M., HAVNES, O., HILLIER, J.K., HORANYI, M., IGENBERGS, E., JESSBERGER, E.K., JOHNSON, T.V., KRÜGER, H., MATT, G., MCBRIDE, N., MOCKER, A., LAMY, P., LINKERT, D., LINKERT, G., LURA, F., MCDONNELL, J.A.M., MÖHLMANN, D., MORFILL, G.E., POSTBERG, F., ROY, M., SCHWEHM, G.H., SPAHN, F., SVESTKA, J., TSCHERNJAWSKI, V., TUZZOLINO, A.J., WÄSCH, R. & GRÜN, E. (2006). In situ dust measurements in the inner Saturnian system. *Planet. Space Sci.*, **54**, 967–987. 26, 34, 76

TAKECHI, S., NOGAMI, K., MIYACHI, T., FUJII, M., HASEBE, N., IWAI, T., SASAKI, S., OHASHI, H., SHIBATA, H., GRÜN, E., SRAMA, R. & OKADA, N. (2009). Laboratory calibration measurements of a piezoelectric lead zirconate titanate cosmic dust detector at low velocities. *Advances in Space Research*, **43**, 905–909. 3

TIELENS, A.G.G.M., MCKEE, C.F., SEAB, C.G. & HOLLENBACH, D.J. (1994). The physics of grain-grain collisions and gas-grain sputtering in interstellar shocks. *Astrophys. J.*, **431**, 321–340. 16, 115

WAITE, J.H., COMBI, M.R., IP, W.H., CRAVENS, T.E., MCNUTT, R.L., KASPRZAK, W., YELLE, R., LUHMANN, J., NIEMANN, H., GELL, D., MAGEE, B., FLETCHER, G., LUNINE, J. & TSENG, W.L. (2006). Cassini Ion and Neutral Mass Spectrometer: Enceladus Plume Composition and Structure. *Science*, **311**, 1419–1422. 22, 33

ZOLOTOV, M.Y. (2007). An oceanic composition on early and today's Enceladus. *Geophys. Res. Lett.*, **34**, 23203. 26, 35

ZOOK, H., GRÜN, E., BAGUHL, M., HAMILTON, D., LINKERT, G., LIOU, J.C., FORSYTH, R. & PHILLIPS, J. (1996). Solar wind magnetic field bending of jovian dust trajectories. *Science*, **274**, 1501–1503. 4, 5, 9, 47, 48, 67, 77, 78, 87, 90

SUMMARY REFERENCES

2

Publication List

Chapter 3 Hsu, H. W., Kempf, S., Jackman, C. M. (2009b). Observation of Saturnian Stream Particles in the Interplanetary Space. *Icarus*, **In Press**.

Chapter 4 Hsu, H. W., Kempf, S., Postberg, F., Srama, R., Jackman, C. M., Moragas-Klostermeyer, G., Helfert, S., and Grün, E. (2009a). Interaction of the Solar Wind and Stream Particles, Results From the Cassini Dust Detector. *AIP conference proceedings; Solar Wind 12*, **In Press**.

Chapter 5 Hsu, H. W., Postberg, F., Kempf, S., Trieloff, M., Burton, M., Roy, M., Srama, R., Moragas-Klostermeyer, G., Saturnian Stream Particles as the Probe of the Dust-Magnetosphere Interaction. (to be submitted).

2. PUBLICATION LIST

3

Observation of Saturnian Stream Particles in the Interplanetary Space

H. W., Hsu, S., Kempf, C. M., Jackman
Icarus (in press)

Abstract

In January 2004 the dust instrument on the Cassini spacecraft detected the first high-velocity grain expelled from Saturn – a so-called stream particle. Prior to Cassini's arrival at Saturn in July 2004 the instrument registered 801 faint impacts, whose impact signals showed the characteristic features of a high-velocity impact by a tiny grain. The impact rates as well as the directionality of the stream particles clearly correlate with the sector structure of the interplanetary magnetic field (IMF). The Cosmic Dust Analyser (CDA) registered stream particles dominantly during periods when the IMF direction was tangential to the solar wind flow and in the prograde direction. This finding provides clear evidence for a continuous outflow of tiny dust grains with similar properties from the Saturnian system. Within the compressed part of co–rotating interaction regions (CIRs) of the IMF, characterized by enhanced magnetic field strength and compressed solar wind plasma, CDA observed impact bursts of faster stream particles. We find that the bursts result from the stream particles being sped up inside the compressed CIR regions. Our analysis of the stream particle dynamics inside rarefaction regions of the IMF implies that Saturnian stream particles have sizes between 2 and 9 nm and exit the Saturnian systems closely aligned with the planet's ring plane with speeds in excess of $70\,\mathrm{km\,s^{-1}}$.

3.1 Introduction

One of the major findings during the approach of the Cassini spacecraft to Saturn was the discovery of high-velocity streams of nano-sized dust originating from the inner Saturnian system (Kempf *et al.*, 2005a). Until then, only the Jovian system was known to be a source of stream particles (Grün *et al.*, 1993). The dust stream phenomenon is of particular interest for several reasons: (i) outside the planetary magnetosphere the stream particle dynamics is governed by the interaction with the solar wind plasma (Hamilton & Burns, 1993); (ii) stream particles are the fastest solid bodies of the solar system known so far (Zook *et al.*, 1996); and (iii) stream particles may transport material from areas that cannot be explored in-situ by space probes (Kempf *et al.*, 2005a).

3. OBSERVATION OF SATURNIAN STREAM PARTICLES IN THE INTERPLANETARY SPACE

When the Ulysses spacecraft flew by Jupiter during 1991-1992, its on-board dust detector registered in total 11 short bursts of dust impacts with a periodicity of 28 ± 3 days (Baguhl $et\ al.$, 1993; Grün $et\ al.$, 1993). This was a remarkable finding since by then only continuous or sporadic dust phenomena were known. The interaction between dust and the $interplanetary\ magnetic\ field$ (IMF) was first considered to explain the observed angular offset between the directions of dust streams and Jupiter (Grün $et\ al.$, 1993). Hamilton & Burns (1993) proposed that the dynamics of stream particles is dominated by the Lorentz force perpendicular to the ecliptic plane due to the tangential IMF component and connected the dust-burst period to the large scale variation of the IMF caused by the solar rotation.

By means of numerical simulations Zook $et\ al.$ (1996) convincingly showed that only grains of about $10\,\mathrm{nm}$ with speeds exceeding $200\,\mathrm{km\,s^{-1}}$ reproduce the observations by the Ulysses detector. In other words, Jovian stream particles propagate into the interplanetary space with speeds comparable to the solar wind plasma. Carrying the twin dust detector, Galileo spacecraft observed even stronger dust bursts during its Jupiter approach (Grün $et\ al.$, 1996). The incident impact angle resembled the tangential IMF component fluctuations. However, no 28 days periodicity was found. Krüger $et\ al.$ (2006) analyzed the dust data during Ulysses' second Jupiter flyby in 2004. The Ulysses spacecraft scanned through jovigraphic latitudes of $+75°$ to $-25°$ on its high inclination trajectory. Two periodicities of dust impacts are found: 26 days at high jovigraphic latitude and 13 days at the Jovian equator. They also found that the impact direction is correlated to the polarity and the strength of the IMF. Flandes & Krüger (2007) compared the same dust data with the Ulysses IMF measurement and suggested a correlation between the stream-particle activities and intervals of high interplanetary magnetic field strength, such as $co–rotating\ interaction\ regions$ (CIRs, more detail in section 3.3.1) or $coronal\ mass\ ejection$ (CMEs). They also showed that the time difference between the peaks of the dust impact rate and the IMF strength is roughly similar to the dust traveling time from Jupiter to the Ulysses spacecraft.

However, the term "dust stream" is misleading. The stream phenomenon is due to a continuous outflow of nanometer-sized dust particles from the inner systems of Jupiter and Saturn. As a continuous dust flux was observed by the Galileo spacecraft and served as a monitor of Io's volcanic activity in the Jovian magnetosphere (Krüger $et\ al.$, 2003), a weak but continuous impact component was observed by the Cassini spacecraft right outside the Saturnian magnetosphere (see Kempf $et\ al.$ (2005a) and section 3.4.2). After leaving the magnetosphere, the charged particles strongly interact with the IMF in the interplanetary space, where the "dust streams" were observed. Originally the term "dust stream" referred to the impact burst period observed by the dust detectors on Ulysses and Galileo (Grün $et\ al.$, 1992c, 1993, 1996). Because these detectors were not sensitive enough to register the much fainter impacts between two successive bursts the instrument teams naturally assumed that the spacecraft passed

through intense collimated dust "streams". In this paper, we will refer to the charged, fast, tiny grains originating from the Jovian and Saturnian systems and whose dynamics is governed by the interaction with the IMF and the solar wind plasma as "stream particles".

Just as the Ulysses and Galileo detectors, the Cosmic Dust Analyser (CDA) on-board Cassini registered episodic dust bursts with a duration between 1 and 10 days during the spacecraft's flyby of Jupiter in 2000. For the first time, the composition of Jovian stream particles could be determined by means of CDA's time-of-flight mass spectrometer. The particles were found to consist mostly of sodium chloride with traces of sulphur (Postberg *et al.*, 2006), which confirms Jupiter's moon Io as their main source.

Horányi (2000) proposed that, similar to Jupiter, Saturn also should be able to eject stream particles from its magnetosphere. To discover the Saturnian stream particles, a CDA campaign was carefully designed dedicated to detect stream particles during Cassini's approach to Saturn. In agreement with model predictions for the interplanetary dust environment between Jupiter and Saturn, the instrument registered almost no dust impacts until the beginning of 2004, as it approached Saturn. At the beginning of 2004 when Cassini was within $1\,200\,\text{R}_\text{S}$ (Saturn's radius $\text{R}_\text{S} = 60\,268\,\text{km}$) of Saturn, the Cassini dust detector CDA registered 801 faint impacts, whose signals showed the characteristic features of a high-velocity impact by a tiny grain. Because the rise time and the amplitude of the signals caused by the Saturnian and the Jovian stream particles are similar, Kempf *et al.* (2005a) concluded that the mass and the impact speed of those particles are at least comparable. A dynamic analysis showed that Cassini registered stream particles with speeds about $100\,\text{km}\,\text{s}^{-1}$ with sizes of a few nanometers. The mass spectra of the Saturnian stream particles indicate that the majority of them are composed of a silicate material (Kempf *et al.*, 2005b), although the Saturnian ring particles mainly consist of water ice (Hillier *et al.*, 2007; Postberg *et al.*, 2008). The most likely explanation for this discrepancy is that the Saturnian stream particles are the tiny impurities embedded in the ring material rather than the ice particles composing Saturn's rings.

The paper is organized as follows. In section 3.2, we describe the instrument operation and briefly introduce the Cassini dust detector. Here, we also discuss the identification of stream particle impacts. The stream particle observations are presented in Section 3.3. Here we also discuss the properties of the IMF during the time interval considered here. The analysis of the stream particle dynamics inside rarefied and compressed regions of the solar wind is presented in Section 3.4. Finally, we briefly summarize our results in Section 3.5.

Unless otherwise stated, we use the international system of units. All times are spacecraft event Universal Time, UT. For the sake of readability, we will often express

3. OBSERVATION OF SATURNIAN STREAM PARTICLES IN THE INTERPLANETARY SPACE

dates in days of year (DOY). The spacecraft location is given in the J2000 inertial reference frame. Magnetic field data are described in the observer-centric, right-handed, RTN frame (Fig. 3.1 c). Here, the radial component R is directed radially outward from the Sun, the tangential component T is the vector product of the solar spin axis and the radial component R. The normal component N completes the right–handed triad. We sometimes employ the Saturn-centric KPS system (Fig. 3.1 a) formed by X (X-Z plane contains the Sun), Y (completes the right-hand set), and Z (parallel to Saturn's pole axis). Finally, the right-handed spacecraft reference frame is defined by the Ion and Neutral Mass Spectrometer (INMS) boresight x, the magnetometer boom mounting axis y, and the High Gain Antenna (HGA) boresight -z (Fig. 3.1 b).
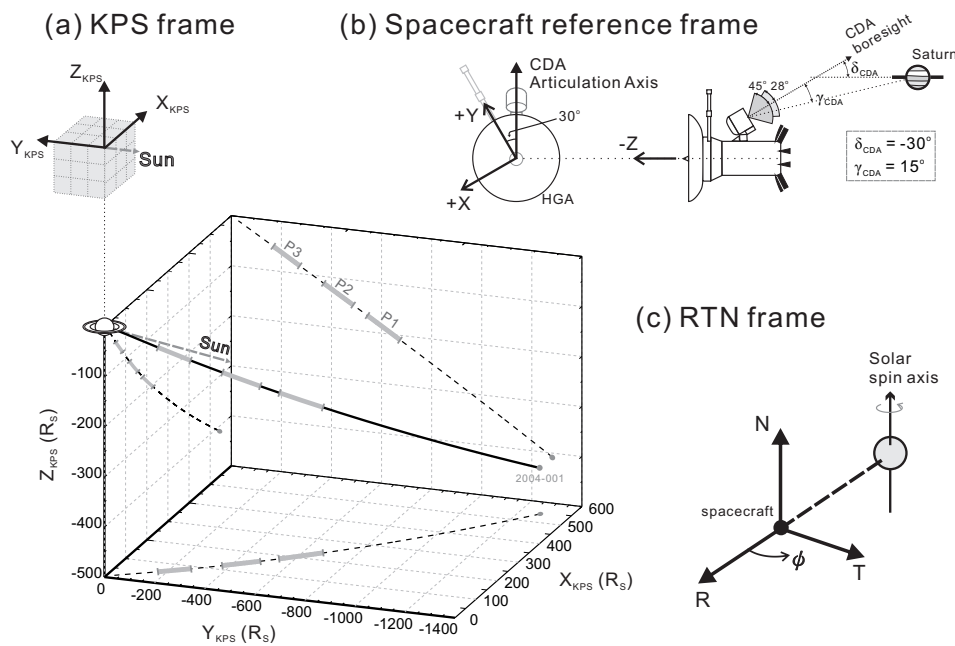
Figure 3.1: Sketch of Cassini's interplanetary trajectory and coordinates systems relevant in this study. - In (a), the spacecraft trajectory is shown in Saturn-centric KPS coordinates with unit of Saturn radii (R_S). *x-y* plane is parallel to the Saturnian ring plane. The Sun lies in +*x-z* plane and its direction is shown by gray-dash arrow. Thick-gray-solid lines and signs (*P1*, *P2*, and *P3*) mark the periods when the IMF azimuthal angle, or ϕ angle was positive, i.e, when the spacecraft traversed the 'toward' sectors (see 3.3.2 and Fig. 3.2). CDA mounting geometry, its field of view, and an example of two angles (δ_{CDA} and γ_{CDA}) are shown in the spacecraft reference frame in (b). (c) shows the the observer-centric RTN frame together with the azimuthal angle ϕ which are used for describing the magnetic field data. See text for more details.

3.2 Mission and instrument operations

Cassini is the fourth spacecraft visiting Saturn. In contrast to its progenitors, Pioneer 11 and the two Voyagers, which only traversed the Saturnian system briefly during their cruise through the solar system, Cassini will orbit the planet at least for six years. Starting on 1 January 2004, 6 months before entering the Saturnian system, the observational conditions were favourable for detecting Saturnian stream particles. Cassini registered the first such particle on day 3 of 2004 (January 3) at a distance of 1427 R_S to Saturn. Until the dust detector was powered off on day 173 of 2004 (June 21), shortly before Cassini's Saturn orbit entry sequence, 801 stream particle impacts were recorded. During this period Cassini was within the solar wind and the stream particle dynamics was governed by the interaction with the IMF.

3.2.1 Cassini dust detector

This paper is based on dust impact data taken by the Cosmic Dust Analyser (CDA) on the Cassini spacecraft which has been described by Srama *et al.* (2004). The CDA consists of two independent instruments: the High Rate Detector (HRD) designed for monitoring impacts of micron–sized grains with high impact rate and the Dust Analyser (DA) for examining individual impactors. The DA is composed of 4 detectors: an Impact Ionisation Detector (IID) similar to the *Ulysses*–type detectors (Grün *et al.*, 1992a,b), a time-of-flight (TOF) mass spectrometer (Mass Analyser – MA), and a charge sensing unit (QP detector) in front of the instrument. To integrate the TOF mass spectrometer into the DA the IID target is divided into an inner rhodium target of 16 cm in diameter (Chemical Analyser Target – CAT) and into a large outer gold target of 41 cm in diameter (Impact Ionisation Target – IIT). The angular field of view (FOV) of the DA is $\pm 45°$ while the CAT FOV is only $\pm 28°$ (Fig. 3.1 b).

A particle striking the hemispherical target of the DA will be at least partially transformed into impact plasma whose amount and expansion time scale provide information about the impactor's mass and impact speed. To achieve this, the plasma generated on the impact target is separated into its constituents by an electric field between the target and the ion grid. The plasma is then collected by individual electrodes and monitored by attached charge amplifiers (plasma electrons - impact target, ions - ion grid). A DA measurement is started either when the impact charge collected in at least one of the electrodes exceeds a pre-set IID threshold or when the strength of a TOF mass line measured at the MA's multiplier in the centre of the instrument exceeds the MA threshold.

51

3.2.2 Identification of stream-particle impacts

Impacts of strength comparable to Jovian stream particles were only registered at large Saturnian distances. In most cases the stream-particle impacts were too faint to trigger an event recording by its impact plasma monitored at the target and the ion grid. In this case the measurement is started by the first mass line of the particle's TOF spectrum (Kempf *et al.*, 2005b). From this follows a couple of important constraints for observations of Saturnian stream particles:

1. The parameters required to estimate the mass (impact charge yield) and the speed (signal rise time) of the striking particle cannot be determined for faint impact signals . Moreover, the dynamic properties of stream particles are well outside the calibrated range. Consequently it is impossible to derive the mass and the speed of Saturnian stream particles from their CDA impact signals.

2. Since only impacts on the CAT result in a mass spectrum, the sensitive area for faint stream particle impacts is reduced by a factor of 9.

3. Due to the faintness of the impact signals, the majority of the stream particles are identified as noise events by CDA's onboard software. As a consequence, such impacts need to be identified by reanalysing the transmitted noise events on the ground.

Between day 1 of 2004 and the start of the CDA power off period on day 173 of 2004 before insertion of Cassini into the Saturnian system, CDA detected a total of 801 stream particle impacts – 382 impacts onto the IIT, 26 impacts onto the acceleration grid of the CA, and 393 impacts onto CAT. All 801 impacts but one are triggered by their hydrogen mass line. Before day 70 CDA only registered impacts on the IIT.

3.2.3 Observational conditions

Cassini is a three-axis stabilized spacecraft, which implies that most observations are performed at a fixed orientation. Because of the large angular field of view of CAT ($\pm 28°$), the impact direction of the stream particles can only roughly be determined during such periods. Even worse, the time variability of the stream directionality cannot be investigated at all with fixed spacecraft orientations. The observational configuration most favourable for monitoring stream particles is when the spacecraft slowly rolls around a fixed axis. During the first 40 days of the approach phase to Saturn, Cassini performed almost continuous rolls around the spacecraft's z and x axes. Afterwards, Cassini rolled every second day during its data transmission to Earth for 8 hours around its z axis at a rate of about 2 revolutions per hour. During these rolls, the detector roughly scanned through the T-N-plane spanned by the tangential (T) and normal (N) direction of the IMF. Cassini's trajectory during its interplanetary cruise almost coincided with the ecliptic plane, which at Saturn's orbital distance is roughly

perpendicular to the T–N plane. Hence, during the approach phase, the CDA observations were sensitive to the normal rather than to the horizontal component of the stream particles' motion with respect to the ecliptic plane.

3.3 Stream-particle detections during Cassini's approach to Saturn

In interplanetary space, the strongest force acting on a tiny charged particle is due to the co-moving electric field $\mathbf{E}_c = -v_{sw}\mathbf{r} \times \mathbf{B}$ induced by the interplanetary magnetic field $\mathbf{B}$ convected by the solar wind plasma streaming radially away from the Sun at speed v_{sw}. At about 9 AU distance to the Sun, the IMF is mostly oriented tangentially to the solar wind flow in the ecliptic plane. This implies that, the direction of $\mathbf{E}_c$ is either northward or southward with respect to the ecliptic plane. This implies that, depending on the IMF sector structure, the direction of $\mathbf{E}_c$ is either northward or southward (with respect to the ecliptic plane), suggesting that the motion of a stream particle is chiefly normal to the ecliptic plane as well. As pointed out above, the conditions for observing vertical changes of the stream particles' directionality were excellent during the spacecraft's data transmission rolls throughout the period considered in this paper.

It is obvious that the particles' directionality derived from CDA observations at a certain spacecraft location cannot provide the complete picture of the stream-particle phenomenon. However, based on Cassini's IMF observations, one can reconstruct, at least partially, the electromagnetic environment traversed by the stream particles on their way to the spacecraft. In this sense, the IMF background acts as the frame of reference for the stream-particle dynamics in interplanetary space. By combining both data sets, we can obtain a more comprehensive picture of the stream-particle propagation.

3.3.1 The interplanetary magnetic field during the approach phase

The approach of Cassini toward Saturn took place during the declining phase of the solar cycle, during which the Sun's dipole is tilted. Such a structure leads to an IMF that is highly structured by compressions and rarefactions associated with Corotating Interaction Regions (CIRs). Jackman *et al.* (2004) studied the structure of the IMF upstream of Saturn over eight solar rotations during Cassini's approach phase, while Jackman *et al.* (2005) continued this analysis to six solar rotations encompassing the Saturn Orbit Insertion (SOI) interval in July 2004. They found a general two-sector structure with compression regions of high field strength and embedded crossings of the *heliospheric current sheet* (HCS) separated by rarefaction regions of lower field strength. Such compressions and rarefactions arise due to the interaction of fast

and slow solar wind streams, and the HCS crossings mark transitions between field regimes pointed 'toward' or 'away' from the Sun. The HCS crossings are represented by $180°$ changes in the azimuthal angle, and occur in the middle of CIR compression intervals. In general, the distribution of azimuth angles in the solar wind upstream of Saturn as sampled by Cassini is in good agreement with the predictions of the Parker model, with some minor deviations (Jackman *et al.*, 2008). Following the SOI maneuver, Cassini spent several months back in the solar wind. During this period, the two-sector CIR-dominated IMF structure was not as clear. This may be due to the fact that this period was closer to the expected time of solar minimum, and thus the heliospheric structure was less predictable than during the declining phase.

An example of the IMF structures described above can be seen from the lower two panels of Fig. 3.2 and Fig. 3.4, especially for the period from day 154 to day 171. The period from day 154 to day 160 encompasses a rarefaction region of extremely low magnetic field strength which was very steady over several days. On day 160, the field strength abruptly increased from ~ 0.2 to $\sim 0.7\,\mathrm{nT}$, marking the shock at the beginning of a compression region. The field strength fluctuated somewhat over the following days, although it remained higher than $0.3\,\mathrm{nT}$, peaking at $\sim 1\,\mathrm{nT}$ on day 163. The $180°$ change in azimuthal angle on the same day represents a spacecraft traversal of the HCS. This particularly interesting period from day 154 to day 160 when Cassini crossed a rarefaction region with unusually stable solar wind conditions with a continuous low flux of stream particles arriving from the Saturn LOS offers a unique opportunity to constrain the physical properties of Saturnian stream particles (see Section 3.4).

3.3.2 Stream-particle directionality

To visualise the stream particles' directionality, we characterize the time-variable three–dimensional CDA orientation by two angles: i) the δ_{CDA} is the elevation angle of the detector boresight with respect to Saturn's ring plane and ii) the γ_{CDA} is the angular separation between the detector boresight and Saturn direction (Fig. 3.1 b). The meaning of these angles is straight forward: δ_{CDA} is positive when CDA is oriented in the direction of Saturn's south pole, negative when CDA is oriented in Saturn's north-polar direction, and zero when the CDA boresight is parallel to Saturn's ring plane, i.e., orthogonal to Saturn's rotation axis. A zero CDA-Saturn angle (γ_{CDA}) indicates that the detectors boresight coincides with the spacecraft–Saturn line of sight. In Fig. 3.2, we show the two angles together with the impact rate and the azimuth angle of the IMF as functions of time and the distance to Saturn.
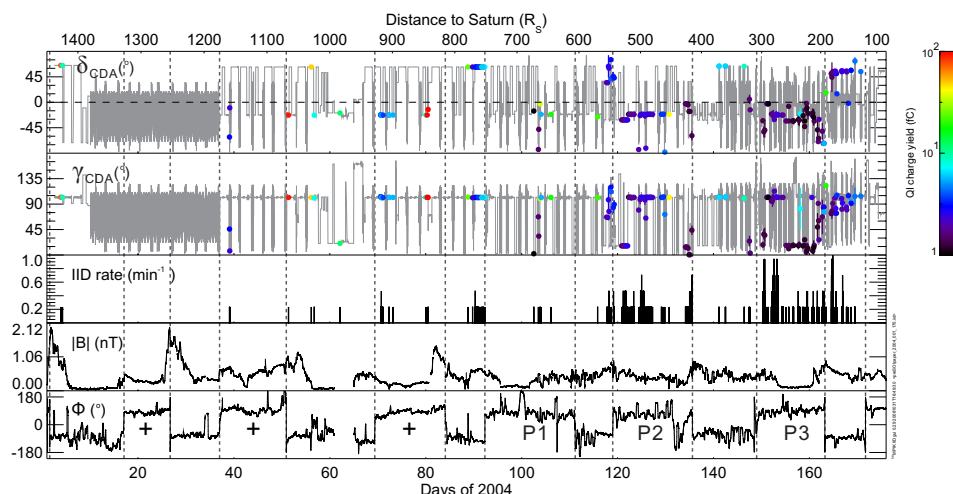
Figure 3.2: Directionality of stream particles detected by CDA between day 1 and day 173 of 2004, - shown together with the particles' impact rate (mid-panel) and with the strength $|\mathbf{B}|$ and the azimuthal direction ϕ of the IMF (two lowermost panels). In the two uppermost panels showing the evolution of the CDA–ring plane angle δ_{CDA} and the CDA–Saturn angle γ_{CDA}, the times of stream particle impacts are colour–coded with the ion charge produced by the impacts. The Heliospheric Current Sheet (HCS) crossings are marked by vertical dash lines, which define the boundaries of IMF sectors. In the bottom panel, the $+$, $P1$, $P2$, and $P3$ symbols mark the periods with positive ϕ angle. (see Table 3.1)

time		ϕ	impacts	δ_{CDA}	γ_{CDA}	name
(date)	(days of 2004)	(°)		(°)	(°)	
April 1 - April 20	092-111	> 0	7	-31 ± 27	73 ± 40	P1
April 20 - April 29	111-119	< 0	23	54 ± 27	93 ± 24	N1
April 29 - May 14	119-135	> 0	279	-22 ± 18	10, 100	P2
May 14 - May 27	135-149	< 0	9	0, 60	20, 100	N2
May 27 - June 11	149-163	> 0	319	-27 ± 13	10, 100	P3
June 11 - June 19	163-171	< 0	74	50 ± 18	87 ± 14	N3

Table 3.1: Solar wind conditions and observed stream-particles directionality in each IMF sector between day 92 and day 171 of 2004. Given are the azimuthal IMF direction ϕ, the number of stream particle impacts, and the CDA–ring plane angle δ_{CDA} and CDA–Saturn angle γ_{CDA} of the observed stream particles. In most cases, the mean value and the standard deviation of the δ_{CDA} and γ_{CDA} are given. For periods which show a bimodal impact angle distribution (ex. P2, N2 and P3), the two maximun values with 10° resolution are given. Notice that the number of stream particle impacts detected during P2 and P3 exceeds those during N2 and N3 by far.

3. OBSERVATION OF SATURNIAN STREAM PARTICLES IN THE INTERPLANETARY SPACE

To meet the ambitious Cassini science program during the approach phase the spacecraft orientation profile was quite complex. As a consequence, the time coverage of the relevant impact directions was sometimes incomplete. To compensate at least partially for the fragmented observational profile, the spacecraft performed at the beginning of the approach phase between day 10 and day 37 an almost continuous series of rolls covering slightly more than a full solar rotation period (the two largest gray areas in the two upper panels of Fig. 3.2). Despite the favourable observational conditions, CDA did not detect stream particles during this period. A possible explanation is that, because of the large distance between the spacecraft and Saturn during this period (ranging between 1400 and $1200 \, R_S$), the stream particle flux had already been diffused by the IMF's stochastic component. After day 37 until day 140 there was on average one data transmission roll every three days. After day 140, when the distance to Saturn became less than $400 \, R_S$, the frequency of data transmission roll periods increased to one per day. Because we observed the most prominent IMF–stream interactions during this period, we restrict our analysis to the time interval between day 100 and day 171. This is also justified by the fact that during this period CDA registered 89% of the stream particle impacts of the approach phase.

The time-dependences of the impact directionality as well as of the impact rate clearly correlate with the IMF structure (see Table 3.1), particularly after day 120. The most prominent indicators for an IMF-stream interaction are:

1. CDA observed changes of the impact rate, the impact charge yields, and the stream directionality whenever the spacecraft traversed the compression regions of CIRs. During the CIR compression region traversals the stream direction changed during a few days from low to high γ_{CDA} values, and δ_{CDA} changed from negative to positive (or vice versa) after the HCS crossings. Simultaneously we observe an increase in the impact rate by a factor of 5 (with respect to the average rates observed when the spacecraft crosses rarefaction regions in the solar wind) and of the ratio between IIT and CAT impacts (more details in Fig. 3.4 and section 3.4.3), indicating that the impacts become more energetic and produce amounts of impact plasma sufficient to trigger the less sensitive IID.

2. CDA detected most of the stream particles during periods when Cassini traversed 'toward' sectors of the IMF characterized by $\phi > 0$ (P2: day 120 to day 135 and P3: day 148 to day 163). Within 'away' sectors of the IMF, i.e. when $\phi < 0$, CDA either recorded very low impact rates or registered particles arriving far off the Saturn line of sight (LOS) direction (N3: day 163 to day 171).

3. Impacts recorded within 'toward' IMF sectors are characterized by negative δ_{CDA} angles, meaning that the grains arrived from below Saturn's ring plane. The γ_{CDA} angle of stream particles detected during 'toward' sector periods decreased with the approach to Saturn. During the last 'toward' sector P3 of the approach phase, the stream particles arrived almost from the Saturn LOS.

3.4 Analysis

3.4.1 Ejection from Saturn's magnetosphere

To start we investigate the connection between the stream particles' escape from the Saturnian magnetosphere and the dependence of the stream particle flux on the IMF sector structure as observed by CDA during the approach phase. At first we note that the typical propagation time of a Saturnian stream particle to an observer at about $500\,R_S$ distance to Saturn is about 3 days (assuming a typical speed of $\sim 100\,\mathrm{km\,s^{-1}}$ is consistent with the rise time of the impact signal, see (Kempf *et al.*, 2005a)), while the typical solar wind propagation time from the observer to Saturn is less than a day. Both propagation time scales are short compared to the typical duration of an IMF 'toward' or 'away' sector of 7 to 13 days. This suggests that to a rather good approximation the IMF conditions along the particle's trajectory to the observer were similar to the IMF conditions measured at the spacecraft at the time of the particle detection.

Within the Saturnian magnetosphere positively charged grains are accelerated outward by the outward–pointing co–rotational electric field stemming from the Saturnian plasma rigidly rotating with the planet's magnetic field (Hamilton & Burns, 1993; Horányi, 2000; Horányi *et al.*, 1993). All possible sources of positively charged grains such as the A ring outside the synchronous radius at $1.86\,R_S$ and the E ring outside approximately the Dione's orbit are located close to the ring plane. Because the planet's magnetic dipole field is aligned within $1°$ of the planet's rotation axis, Saturnian stream particles are accelerated mostly along the ring plane. Hence, one expects the stream particles to emerge from the Saturnian system mainly orthogonal to the planet's rotation axis, i.e., in the ring plane.

In fact, the CDA observations provide evidence for this scenario, because the detector mainly registered stream particle impacts when Cassini was within a 'toward' IMF sector, i.e., when the $\mathbf{E}_c$ direction was southwards (see Section 3.3.2). This suggests that the trajectories of stream particles registered within 'toward' IMF sectors were bent by the co-moving E field below the ring plane towards Cassini. In contrast, stream particles which escaped from Saturn's magnetosphere when Cassini moved through an 'away' sector of the IMF experienced an acceleration toward the north of the ring plane and could thus not reach the spacecraft. Escape trajectories significantly deviating from the ring plane would cause a less pronounced rate dependence on the sector polarity.

On the first view, the simple picture that stream particles exit the Saturnian system mostly on trajectories parallel to the ring plane may be spoiled by the fact that at larger distances CDA observed stream particles during 'toward' IMF sector periods, which did not arrive from the Saturn LOS direction. To verify our idea we simulated the propagation of $2\,000$ stream particles started at $25\,R_S$ distance to Saturn with charge–to–mass ratios in the range $2\,000\,\mathrm{C\,kg^{-1}} \leq Q_d/m_d \leq 20\,000\,\mathrm{C\,kg^{-1}}$ and followed their motion

until they hit the detector. In these simulations, we approximated the IMF structure by a constant tangential magnetic field, whose direction flips at the location of the HCS crossings. For simplicity, we ignored the IMF's fine structure and variations in the solar wind speed and density. From the simulations we derived the distance-dependent ranges of δ_{CDA} and γ_{CDA}, and compared them to the CDA observations (Fig. 3.3). Due to the complex spacecraft operations during the approach phase, the CDA observations did not cover the full range of δ_{CDA} and γ_{CDA}. To visualise the resulting biasing of the CDA data we also show the gray–scaled total sensitive area of CDA as a function of the two angles. Despite the simplified description of the IMF structure, the simulation results match the CDA observations well. The increase of γ_{CDA} with the distance to Saturn is clearly caused by the continuous, though weak acceleration of the stream particles by the tangential magnetic field inside the rarefaction regions of the IMF.
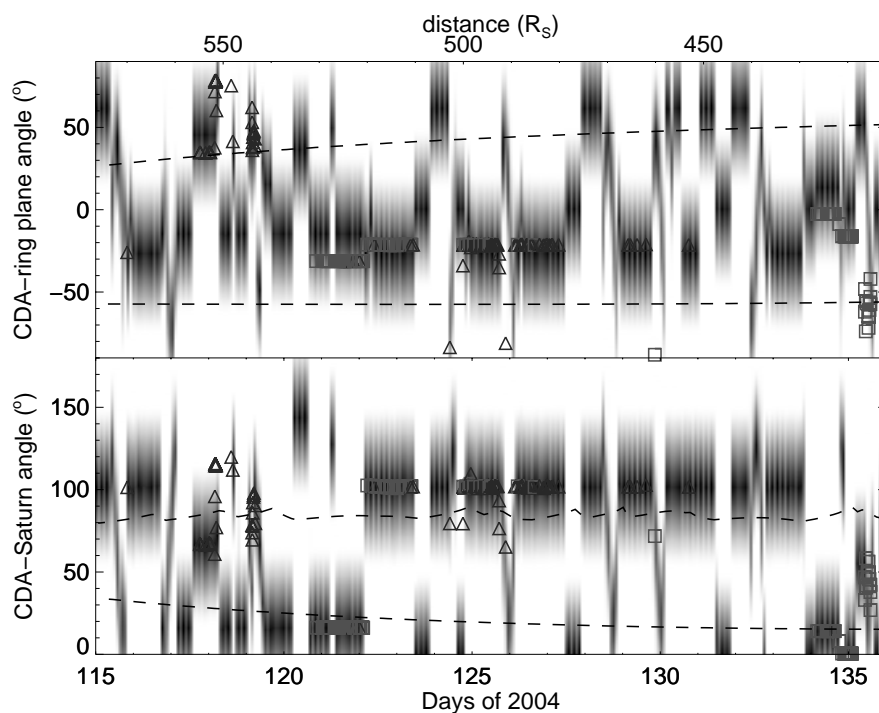
Figure 3.3: Comparison between the impacts angles of stream particles registered during P2 from day 119 to day 135 and simulations - predicting an impact angle range indicated by the broken lines. The gray areas give the color-coded sensitivity area of the IIT. Note that the shown impact angles refer to the instrument's boresight at the time of detection, i.e., the true ITT impact angles (triangles) may deviate from the shown angles by up to $\pm 45°$, while the CAT impact angles (squares) may differ by up to $\pm 28°$.

3.4.2 Stream-particle dynamics inside IMF rarefaction regions

We already mentioned that the stream particle data obtained during the "quiet period" from day 154 to day 160 (see Fig. 3.4), when the IMF conditions were unusually stable, are useful to constrain the charge–to–mass ratio and the ejection speed of the detected particles, which cannot be derived directly from the recorded impact signals. During this period the tangential, clockwise oriented IMF component dominated the other field components, implying an induced electric field roughly parallel to Saturn's rotation axis and oriented away from the ring plane. Because the IMF fluctuated only weakly during this period it is justified to approximate the IMF by a constant tangential field $B_t = 0.1\,\mathrm{nT}$. To simplify the problem further we ignore Saturn's obliquity of $26.73°$ and assume that the solar wind direction is parallel to Saturn's ring plane (leading to a 10% error of the charge–to–mass ratio estimates) We also assume that the solar wind moves at constant speed $v_{sw} = 430\,\mathrm{km\,s^{-1}}$, which is the average value of the solar wind speed during the "quiet period" derived from the phase space density cut–off of He^+ measured by Cassini CHEMS (Hill *et al.*, 2004). Then, under the assumption that stream particles propagate within a plane parallel to Saturn's rotation axis and perpendicular to the solar wind flow direction projected onto the ring plane, Fig. 3.5 illustrates the resulting geometry of the simplified problem.
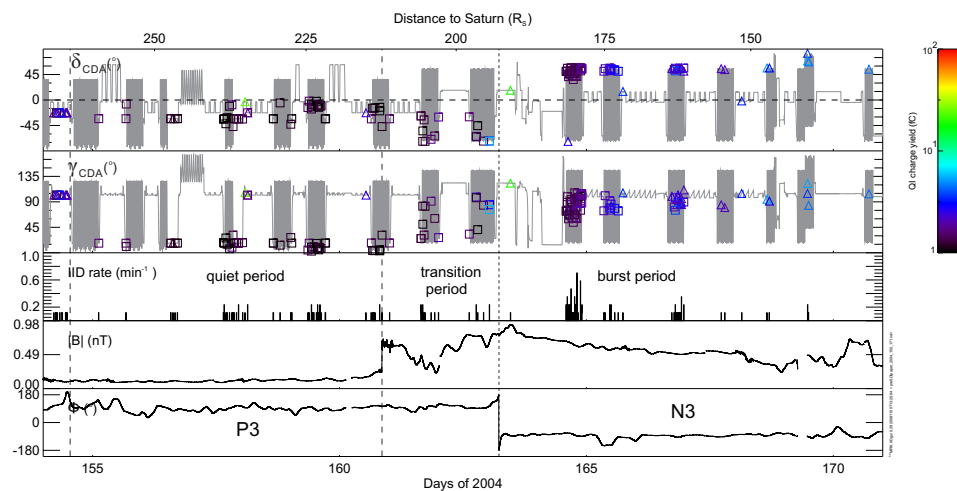
Figure 3.4: Stream particle observations between day 154 and day 171 of 2004 presented together with the IMF field strength |B|. - The data are presented as in Fig. 3.2. Squares identify CAT impacts while triangles mark impacts onto the IIT. The shown time interval includes the "quiet" period from day 154 to day 160, the "transistion" period from day 160 to day 163, and the "burst" period from day 163 to day 171. The time when Cassini crossed the heliocentric current sheet (HCS), defining the boundary between two IMF sectors, is marked by the short dashed line.

3. OBSERVATION OF SATURNIAN STREAM PARTICLES IN THE INTERPLANETARY SPACE

We now consider a stream particle, which escaped at the planetocentric latitude θ at speed v_{ex} from the Saturnian system. The y-component $s_y = v_{ex}\cos\theta\, t$ of the particle position depends only on the flight time t and the y-component of v_{ex}, because the induced electric field accelerates the particle only in z-direction. The z-component of the particle position is approximately

$$s_z(t) \approx v_{ex}\sin\theta\, t - \frac{1}{2}\frac{Q_d}{m_d}v_{sw}B_t t^2,\tag{3.1}$$

where m_d and Q_d are the dust mass and the charge on the grain, respectively. Thus, the charge–to–mass ratio of a stream particle registered at the spacecraft location (s_y, s_z) is

$$\frac{Q_d}{m_d} = \frac{2v_{ex}^2\cos\theta}{B_t \cdot v_{sw}\cdot s_y}\left(\sin\theta - \frac{s_z}{s_y}\cos\theta\right).\tag{3.2}$$
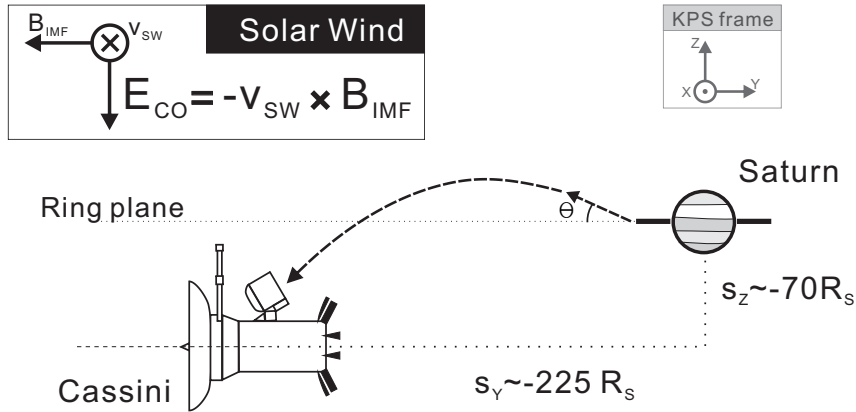
Figure 3.5: Sketch of the observational geometry during the IMF "quiet period" from day 154 to 160 of 2004 - , projected onto a plane parallel to Saturn's rotation axis and perpendicular to the solar wind flow direction projected onto the ring plane (y-z plane of the KPS reference frame). The Sun is in $+x$-z plane and $\sim 27°$ below the ring plane. The IMF points in $-y$ direction. The corresponding induced electric field $\mathbf{E}_c$ points in $-z$ direction, bending the particle's trajectory toward the spacecraft. Cassini's distance to Saturn was about $250\,R_S$ ($\sim 15\cdot 10^6$ km), s_y and s_z are the coordinates of the spacecraft location in this frame. The broken line illustrates a sample trajectory of a stream particle, which escaped from Saturn's magnetosphere at an angle θ to the ring plane.

Fig. 3.6 shows the dependence of the grain size $s_d = Q_d/4\pi\varepsilon_0\phi_d$ on v_{ex} and θ, where we assumed a constant electrostatic surface potential of $\phi_d = +5$ V, which is typical for interplanetary conditions (Horányi, 1996; Kempf *et al.*, 2004). By comparing the

impact signals of Saturnian stream particles with the signals of the fastest calibration impact recorded at the Heidelberg dust accelerator facility, Kempf *et al.* (2005a) showed that the impact speed of these grains exceeds $63\,\mathrm{km\,s^{-1}}$. This suggests that the typical Q_d/m_d of stream particles registered during the "quiet period" ranged between $1\,650$ and $25\,000\,\mathrm{C\,kg^{-1}}$ (including the 10% factor introduced by the simplified geometry) corresponding to grain sizes between $2.3\,\mathrm{nm}$ and $9.0\,\mathrm{nm}$, provided that the grains escaped from the Saturnian system on trajectories closely aligned with the ring plane $(-10° \leq \theta \leq +10°)$.
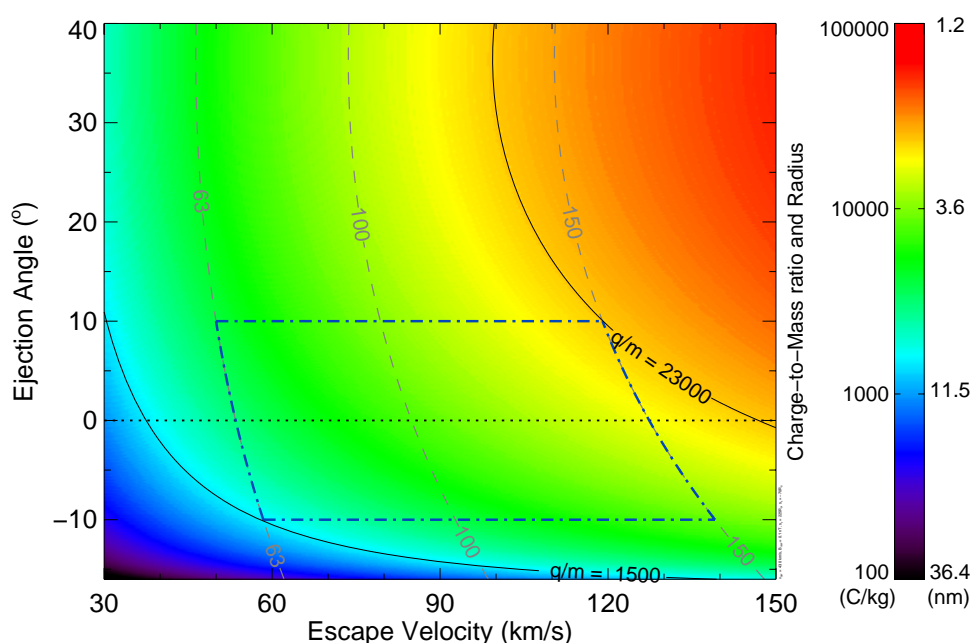
Figure 3.6: Colour-coded charge–to–mass ratio Q_d/m_d and grain size s_d of the stream particles registered during the "quiet section" from day 154 to day 160 of 2004 - , given as functions of their exit speed v_{ex} and the planetocentric latitude θ of their escape trajectory. The grain size s_d was calculated for an electrostatic surface potential of $\phi_d = +5\,\mathrm{V}$.

The flight time of these particles in the solar wind is less than 3 days, which is comparable to the time for a $9.0\,\mathrm{nm}$ dust grain to collect a single solar wind electron (assuming plasma density of $5\cdot10^4\,\mathrm{m^{-3}}$ and a temperature of $1\,\mathrm{eV}$) and to emit a single photo-electron produced by the solar UV. This corresponds to a 3% effect for the Q_d/m_d of $9.0\,\mathrm{nm}$ grains and to a 20% effect for $2\,\mathrm{nm}$ grains. Nevertheless, the charging time, proportional to inverse square of the grain radius, for $2\,\mathrm{nm}$ grains is much longer

than the 3 day flight time. The assumption of a constant grain charge is justified for grains with 3 day flight time through the solar wind.

3.4.3 Stream-particle dynamics inside CIR compression regions

During recent years, the close connection between CIR traversals of the observing spacecraft and periodic stream-particle impact bursts – the so-called streams – has become an accepted view (Flandes & Krüger, 2007; Kempf *et al.*, 2005a; Krüger *et al.*, 2006). CDA observed the strongest stream particles–CIR interaction shortly after the "quiet period" discussed in the previous section. On day 162 Cassini crossed the outer boundary of compressed solar wind indicated by a rapid increase of the IMF field strength from 0.2 to $0.7\,\mathrm{nT}$ within a few hours. The IMF field strength reached its maximum value of about $1\,\mathrm{nT}$ on day 163 accompanied by an abrupt $180°$ change of the field direction marking the crossing of the HCS. Cassini left the CIR compression region around day 170. Fig. 3.4 shows the directionality and impact rates of the stream particles and the IMF conditions between day 154 to day 171 covering the transition from the rarefaction to the compressed region of the solar wind.

The stream-particle properties clearly changed during the transition from rarefaction to compressed solar wind conditions. During the "quiet" period, the stream particles arrived roughly from the Saturn LOS and produced only little impact plasma of typically less than $1\,\mathrm{fC}$. The scatter of the CDA-RP angle of $\delta_{CDA} = -24° \pm 21°$ during this period may reflect the divergence of the escape trajectories from the ring plane. The "transition period" started from the sharp increase of the magnetic field strength on day 160 and lasted till the HCS crossing on day 163. During this period γ_{CDA} started to increase simultaneously with the strength of the registered impacts. At the end of the "transition period", right before the spacecraft crossed the HCS, the arriving direction of stream particles had significantly changed and became almost orthogonal to the ring plane and Saturn direction ($\delta_{CDA} \sim -70°$ and $\gamma_{CDA} \sim 90°$). The observed change of the stream directionality as well as of the impact strength clearly correlates with the increase of the magnetic field strength suggesting that within the compressed solar wind region the stream particles experienced a strong acceleration away from the ring plane due to the enhanced field strength and increased solar wind speed. Because of the resulting increase of the stream particle speed, the detected particles produced more impact plasma and their impact rate increased. This explanation is consistent with the simplified picture discussed in the previous section: a spacecraft approaching Saturn from below its ring plane can only detect grains accelerated away from the ring plane.

During the "burst" period extending from day 163, right after the HCS crossing, to day 171, the dust detector observed a strong burst of stream particle impacts. The impact rate rapidly rose to its maximum value and slowly decayed afterwards. During

the first 8 hours spacecraft roll after the HSC crossing, CDA detected 41 impacts, or about five times more impacts per roll than observed during the "quiet" and "transition" periods. Only one of the particles hit the IIT. The impact's large negative CDA–ring plane angle of $\delta_{CDA} \sim -75°$ may indicate that this particle still belonged to the "transition period" population, whose members arrived during the "burst period" from directions outside the CAT FOV. In contrast, the positive δ_{CDA} angles of the 40 CAT impacts are a consequence of the flip of the field direction during this period, i.e., after their escape from the Saturnian system the particles first traversed a "toward" IMF sector corresponding with $\mathbf{E}_c$ directed away from the ring plane and entered after the HCS crossing an "away" sector corresponding to $\mathbf{E}_c$ directed toward the ring plane. The mean solar wind properties after the HCS crossing ($v_{sw} \approx 450\,\mathrm{km\,s^{-1}}$, $|\mathbf{B}| \approx 0.6\,\mathrm{nT}$) lead to an induced electric field of $E_c \approx 2.7 \cdot 10^{-4}\,\mathrm{V\,m^{-1}}$. After one day, a 4 nm stream particle with a surface potential of $+5\,\mathrm{V}$ accelerated by such a strong induced electric field already gained about $200\,\mathrm{km\,s^{-1}}$, which exceeds its ejection speed by far and explains the large observed δ_{CDA} angles. The later spacecraft rolls are characterized by lower impact rates and by increasing impact strengths and an increasing ratio between IIT to CAT impacts. These facts indicate that during this period the particles were accelerated further by the strong $\mathbf{E}_c$ field to even higher speeds. As a consequence, the impacts became energetic enough to exceed the IIT thresholds, while the particles' trajectories were bent outside the instrument's angular FOV. Thus, an instrument with a 4π angular FOV would have observed a continuously increasing impact rate with a simultaneous rotation of the stream particles' impact direction until the end of the "burst" period. After the "burst" period, CDA detected again only stream particles moving through the rarefaction region of the IMF and thus arriving from directions close to the Saturn LOS.

3.5 Summary and future work

During its approach to Saturn in 2004, the dust detector on Cassini discovered stream particles escaping from the inner Saturnian system. Between January and June 2004 CDA registered 801 stream particle impacts. The impact rates as well as the directionality of the stream particle flux provides clear evidence for a strong interaction between the positively charged dust grains and the IMF convected by the solar wind plasma. In contrast to the observations of Jovian stream particles by the Ulysses and Galileo dust detectors (Grün *et al.*, 1993, 1996), CDA monitored a more-or-less continuous weak flow of stream particles. This fact gives clear hint that the periodic impact bursts characteristic of the stream-particle phenomenon stem from local interactions of the particles with the IMF. The amplitudes of these interactions depend on both solar wind conditions and the particle properties. In contrast to the quiescent dust activity within the rarefaction regions of CIRs (ex. between day 154 and 160), strong acceleration occurs within the compression regions of CIRs and leads to a strong increase of the impact rate and the impact energy as well as to the change of the impact direction

as observed by CDA between day 163 and 171. Further evidence for local IMF interactions comes from the fact that the impact bursts observed by CDA always coincide with spacecraft traversals through CIR compressions, confirming earlier observations (Flandes & Krüger, 2007; Grün *et al.*, 1993; Kempf *et al.*, 2005a; Krüger *et al.*, 2006).

These observational facts lead to a more general picture about the stream-particle dynamics in the interplanetary space. As the nano-meter size dusts are continuously produced and ejected from the planetary system with high velocity, an extended dust sheet forms and is located within the plane close to the magnetic equatorial plane of the planet. As dusts propagate outward and enter the interplanetary space, these particles are steadily accelerated away from the ecliptic plane due to the tangential component dominated the IMF at Jupiter and Saturn distance. In the interplanetary space, the dust sheet is warped by the IMF as suggested by Hamilton & Burns (1993). Consequently, the thickness of the dust sheet increases with the distance to the source body. Meanwhile its density decreases. The overall morphology of the dust sheet is controlled by the IMF structure and the solar wind conditions. Thus, the sheet morphology varies with the solar cycle.

However, in regions where the solar wind is compressed and the IMF is enhanced (e.g. CIR compressions), particles gain much more energy in a short period. Here, the dust sheet can be strongly deformed and even be bent to the opposite direction after the HCS crossing, as observed by CDA. The strong increase of the impact rate, impact energy, and the IIT-to-CAT impact ratio within the compressed solar wind suggest that the dust stream phenomenon as observed by in-situ detectors mainly results from the local dust-IMF interaction.

Another interesting result is the pronounced dependence of the stream particle impact rate on the magnetic field direction inside rarefaction regions of the solar wind. As an immediate consequence, Saturnian stream particles escape from the planet's gravity on trajectories close to its ring plane. We show that the CDA observations between day 154 and day 160 constrain the size of the detected grains to 2 to 9 nm and the particles' ejection speed from the Saturnian system to $\sim 70\,\mathrm{km\,s}^{-1}$.

After Cassini's arrival at Saturn the spacecraft explored the inner part of the planetary system and crossed the boundary of the planet's magnetosphere multiple times. We expect that the stream particle data acquired inside and outside the Saturnian system will be helpful in understanding the evolution from micron-sized ring particles to nanometer-sized particles capable of escaping from the planet's gravity (Hsu *et al.*, 2008).

3.6 Acknowledgments

3. OBSERVATION OF SATURNIAN STREAM PARTICLES IN THE INTERPLANETARY SPACE

4

Interaction of the Solar Wind and Stream Particles, Results From the Cassini Dust Detector

H. W., Hsu, S., Kempf, F., Postberg, R., Srama, C. M., Jackman, G., Moragas-Klostermeyer, S., Helfert, and E., Grün
AIP conference proceedings, Solar Wind 12 (in press)

Abstract
The stream particles are nanometer-size dust particles ejected from the jovian and the Saturnian systems with velocities greater than sensitive 100 $\mathrm{km\,s}^{-1}$. Due to their small size, stream particles are more to the electromagnetic force than to gravity. It has been shown by the simulations that the stream–particle dynamics in interplanetary space should be dominated by the interplanetary magnetic field (IMF) (Zook *et al.*, 1996). Based on the measurements by the dust detector on board the Cassini spacecraft, we found that the detection patterns of the stream particles are well correlated with the IMF structures. As the spacecraft crosses the compression regions of the Co–rotation Interaction Regions (CIRs), not only the directionality of the impacts changes with the field direction, but also the impact signal and rate vary with an increase of field strength. By understanding the interaction of stream particles and the solar wind, the data provide important insight to the formation environments of the stream particles and is an unique opportunity to study the dust-moon-magnetosphere system of Jupiter and Saturn.

4.1   Introduction

Stream particles are nanometer-size dust particles ejected from jovian and Saturnian systems with velocities greater than 100 $\mathrm{km\,s}^{-1}$. They were first discovered by the dust detector of the Ulysses spacecraft during its first Jupiter flyby in 1992 (Grün *et al.*, 1993). Using in-situ IMF and solar wind measurements as constraint, the backward tracing simulation convincingly showed that the particles detected by the Ulysses spacecraft have sizes of 10 nm and impact velocities above 200 $\mathrm{km\,s}^{-1}$ (Zook *et al.*, 1996). Subsequent measurements by the Galileo spacecraft suggest that Io is the

main source of jovian stream particles (Graps *et al.*, 2000). Models showed that positively charged dust particles in the magnetosphere may gain enough energy from the outward–pointing co–rotation electric field and are capable to escape from the planetary system with high speed (Horányi, 2000; Horányi *et al.*, 1993). By understanding the ejection process, the long–term stream–particle observations from Galileo spacecraft can serve as a tool for monitoring the Io plasma torus and ionian volcanic plume activities (Krüger *et al.*, 2003).

The Cassini–Huygens mission was launched in 1997 and flew by Jupiter on December 30, 2000. Since the Saturn Orbit Insertion (SOI) on July 1, 2004, the spacecraft has been orbiting Saturn and is currently on the extended Cassini Equinox Mission. In September 2000, when the Cassini spacecraft was still 1 AU away from Jupiter, CDA started to register stream–particle impacts. The chemical analysis suggested that the major compound of jovian stream particles is sodium chloride, which supported the idea of them originating from Io's volcanic plumes (Postberg *et al.*, 2006). On the other hand, the Saturnian stream particles, one of the discoveries during Cassini's Saturn approach in 2004 (Kempf *et al.*, 2005a), are mostly composed of silicate material (Kempf *et al.*, 2005b) and unknown amount of water ice. Besides the compositional difference, Saturnian stream particles were found to be smaller, and were ejected more slowly along the ring plane (**?**), while their big and fast counterpart at Jupiter gains more off–equator acceleration and forms a dust sheet with 'ballerina skirt' structure (Grün *et al.*, 1998).

After leaving the planetary magnetosphere, the stream-particle dynamics is determined by the co–moving electric field $\mathbf{E}_{co} = -\mathbf{V_{sw}} \times \mathbf{B}$ induced by the solar wind plasma flow. Charged dust particles are accelerated either northward or southward from the ecliptic plane and consequently form periodic bursts observed by the Ulysses spacecraft (Hamilton & Burns, 1993).

In this work we focus on dynamical properties of jovian and Saturnian stream particles in interplanetary space. CDA data are combined with solar wind measurements by Cassini MAG and MIMI instruments. The CDA jovian stream–particle observation during 2000 to 2001 is discussed in Section 4.2. We analyze Saturnian stream–particle data during Cassini's first orbit (orbit A) in Section 4.3. A short summary is presented in Section 4.4.

4.2   Jovian Stream Particles

Fig. 4.1 shows the CDA measurement of jovian stream particles during 2000 and 2001 close to the solar maximum. To fulfill various scientific goals, the pointing profile of the Cassini spacecraft is very complex and not uniform. So it is difficult to compare the Cassini dust measurements directly with those obtained from the rotating

Galileo spacecraft. Nevertheless, two tendencies can be identified. First, CDA detected stream particles when it pointed toward the Jupiter line of sight (LOS) direction (small γ_{CDA} in Fig. 4.1) even though the IMF strength fluctuated a lot. Second, albeit that two spacecrafts were at different locations and experienced different electromagnetic field, the CDA data seem to have a similar trend as the Galileo total dust emission rate (Krüger *et al.*, 2003). As one can see in Fig. 4.1, though the Cassini spacecraft was at similar jovicentric distance in period A and B, the number of impacts is clearly higher during period A. This matches the declining trend in the Galileo result. At the right end of the plot, the dust burst detected by CDA in period C again coincided with the Galileo trend.
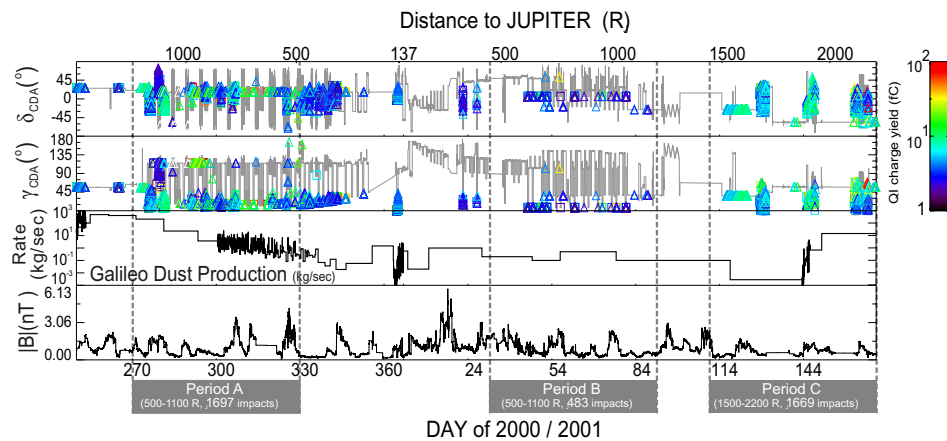
Figure 4.1: Jovian stream–particle observations between day 250 of 2000 and day 170 of 2001 - are presented together with pointing profile, the total dust production rate derived from Galileo measurements (Krüger *et al.*, 2003), and the IMF field strength. CAT and IIT impacts are shown in squares and triangles and color–coded with CDA ion grid signal (QI) to represent the impact strength. The impact directionality is expressed by two angles: γ_{CDA} is the angle between the CDA boresight and the source (Jupiter or Saturn). δ_{CDA} is the elevation angle between the CDA boresight and a reference plane. The ecliptic plane and the Saturnian ring plane are chosen as reference planes for jovian and Saturnian observations respectively. To compare with the Galileo result, three periods with corresponding number of CDA impacts and the spacecraft–Jupiter distance are marked at the bottom.

Fig. 4.2 demonstrates a clear evolution of stream particles within high IMF solar wind. Based on the impact directionality and strength, two impact components are identified. Component one impacts arrived roughly from the Jupiter direction. Their signals were in general higher than those of component two, which suggests that component one particles were either bigger or faster. Component two impacts were mostly detected during day 278 to 281 at large γ_{CDA}. Most of component two impacts

69

were detected by the IIT, while the CAT–to–IIT ratio of component one decreased with time.
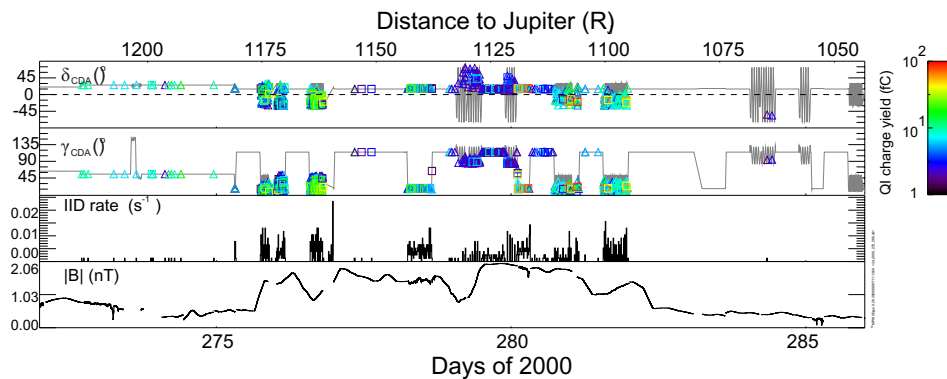
Figure 4.2: Jovian stream–particle observations between day 272 and day 286 of 2000. - The lower three panels are the CDA impact rate, IMF strength, and the IMF azimuthal angle. Note that the impact rate was strongly biased by the complex pointing profile. Nevertheless, two impact components can be clearly identified based on the impact directionality and strength.

To understand the reason for these two dynamically different components, we first notice that not only the impact charge yield but also the impact direction of component one were comparable to stream particles detected by Ulysses and Galileo dust detectors (with $QI \sim 10^{-14}$ fC and from direction close to Jupiter LOS). Hence, we consider the component one as the typical 'Ulysses/Galileo' dust bursts. Component two is more difficult to understand. Their lower impact charges suggest that they could be slower or smaller, or both. Moreover, since they did not come from the Jupiter direction, they could even be of non–jovian origin.

However, stream particles can be accelerated substantially by $\mathbf{E}_{co}$ and be detected at large γ_{CDA} as observed at Saturn (Hsu *et al.*, 2009b). Considering component two was observed during high–IMF period and there were no other known sources of nano–dust except the jovian system, they were most likely also jovian stream particles but with smaller sizes. If so, their dynamics would be more influenced by the IMF and it explains their large γ_{CDA}. Further chemical analysis probably can provide crucial evidence to justify the origin of component two.

Back to component one (typical jovian stream particles), their relatively bigger sizes allowed them to preserve original velocity vectors after a period of strong IMF and eventually to be detected at small γ_{CDA}. Moreover, the increasing impact charge

and the decreasing CAT–to–IID ratio during this high–IMF period indicate that a pronounced acceleration had occurred during the observation. A similar phenomenon has been observed in the compressed solar wind regions upstream of Saturn (e.g. (Hsu *et al.*, 2009b) and Fig. 4.3) and suggests that the dust stream phenomenon is mainly due to local dust–IMF interaction.

4.3 Saturnian Stream Particles

The approach of Cassini toward Saturn was during the declining phase of the solar cycle. The IMF was highly structured by compressions and rarefactions associated with Co–rotation Interaction Regions (CIRs) (Jackman *et al.*, 2004). Following Hsu *et al.* (2009b), we extend the IMF–stream–particle analysis from pre–SOI phase to orbit A.
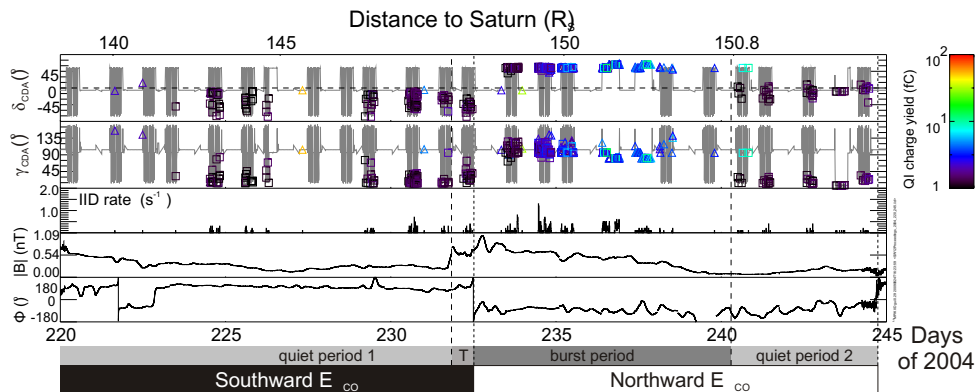
Figure 4.3: Saturnian stream-particle observations between day 220 and day 245 of 2004. - Panels are similar as Fig. 4.2. As in Hsu *et al.* (2009b), we use IMF structures as a reference frame to define three stream-particle-IMF interaction periods. The direction of the $\mathbf{E}_{co}$ is also shown. Note the correlation between the $\mathbf{E}_{co}$ direction and the δ_{CDA}.

Fig. 4.3 demonstrates 25 days of stream–particle data during the orbit A. The impact pattern was highly correlated with the rarefaction and compression structures, as those observed during the pre–SOI phase (Hsu *et al.*, 2009b, Fig. 6). Three periods, which reflect different phases of IMF–stream–particle interactions, have been marked. They are: two quiet periods, the transition period (marked as 'T'), and the burst period. During the quiet period 1, CDA observed weak impacts with small γ_{CDA}. The burst period came after the short transition period. The strengthened and reversed $\mathbf{E}_c$ pushed particles toward the opposite direction of the ring plane (as the δ_{CDA} changed

from negative to positive). Moreover, the impacts were getting stronger with increasing γ_{CDA}, which suggests that stream particles experienced substantial acceleration comparable to their initial velocity. Impacts detected after the burst period showed again the quiet-period characteristics, i.e., low–energy impacts with small γ_{CDA}.

Since the IMF strength and direction during quiet periods were stable, it is reasonable to assume that particles experienced a constant $\mathbf{E}_c$ during their journey from Saturn to CDA. As the IMF configuration during the quiet period 1 was the same as the one in Hsu *et al.* (2009b), we only show the analysis of the quiet period 2 (day 240 to 245 in 2004). During this time, $\mathbf{E}_{co}$ pointed roughly northward from the ring plane and the spacecraft was about 44 R_S south of the ring plane. This means that particles ejected along the ring plane from the Saturnian system would be bent northward and reach the detector with lower probability. In other words, these detections gave information about the (south) ejection angle of Saturnian stream particles.
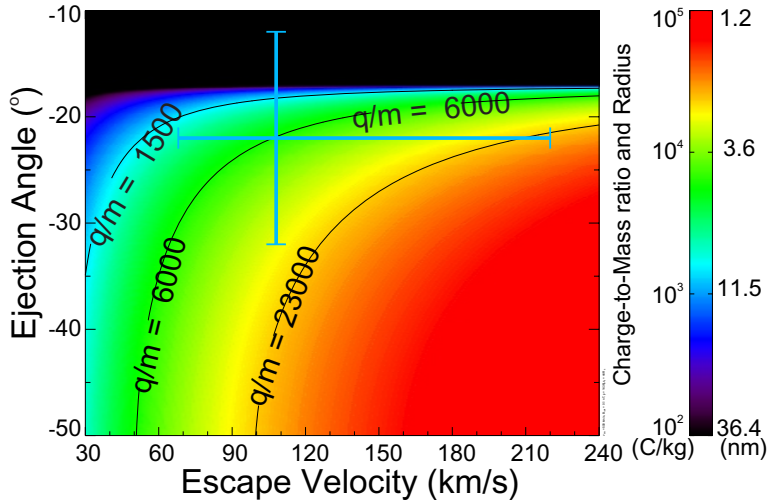
Figure 4.4: Saturnian–stream–particle properties in the rare- faction solar wind from day 240 to 245 in 2004. - The grain charge–to–mass ratio is shown as function of θ and v_{ex}. The blue cross marks the most likely parameter region.

Using the MAG and MIMI Hill *et al.* (2004) data for the IMF and the solar wind speed ($\mathbf{B}_T \sim 0.1\,\mathrm{nT}, v_{sw} \sim 500\,\mathrm{km\,s^{-1}}$), the dependence of the grain size on ejection velocity (v_{ex}) and ejection angle (θ) during this period is shown in Fig. 4.4. The observed δ_{CDA} ($-11° \pm 12°$), the minimum impact speed (63 $\mathrm{km\,s^{-1}}$), and the travel time (≥ 0.5 day) serve as further constraints and are marked by the blue cross. The stream particles detected during this period have charge–to–mass ratio around 6,000 $\mathrm{C\,kg^{-1}}$,

which corresponds to $\sim 4\,\mathrm{nm}$ radius (assuming $\phi = +5$ volt). The v_{ex} is between 60 to 200 $\mathrm{km\,s^{-1}}$ and the maximum θ is about $-20°$ to $-30°$.

4.4 Summary

In this work, we presented the jovian and Saturnian stream–particle observations carried out by the Cosmic Dust Analyser on–board Cassini spacecraft. The data cover different heliospheric distances and solar–cycle phases, which allow us to compare with measurements from previous spacecrafts and to improve our knowledge of nano–dust dynamics in interplanetary space.

In consequence of the complex IMF structure during Cassini's Jupiter flyby in 2000/2001, two impact components with different dynamical properties were observed within one high–IMF period. The stronger component from Jupiter LOS has similar dynamical properties as those detected by the Ulysses and Galileo spacecrafts. More important, combined with the chemical analysis results (Postberg *et al.*, 2006), the similar trend between Cassini and Galileo dust data justify the idea of monitoring ionian volcanic plume activities with stream–particle measurement (Krüger *et al.*, 2003).

The CDA Saturnian observation took place during the declining phase of the solar cycle in 2004. The IMF was much more structured compared to the condition during the Cassini Jupiter flyby. The imprint of the recurrent IMF structure could be identified in the stream-particle patterns. Stream-particle properties derived during the solar wind rarefactions in orbit A are consistent with Hsu *et al.* (2009b), with an ejection angle maximum of $-20°$ to $-30°$.

4. INTERACTION OF THE SOLAR WIND AND STREAM PARTICLES, RESULTS FROM THE CASSINI DUST DETECTOR

5

Saturnian Stream Particles as the Probe of the Dust-Magnetosphere Interaction

H. W., Hsu, F., Postberg, S., Kempf, M., Trieloff, M., Burton, M., Roy, R., Srama, G. Moragas-Klostermeyer,
to be submitted

Abstract

Stream particles are nano–meter scale dust particles ejected with speeds $\gtrsim 100\,\mathrm{km\,s^{-1}}$ from both Jovian and Saturnian systems. In this work we analyse the dynamics and composition of Saturnian stream particles based on measurements during 2004 and 2005 carried by the Cosmic Dust Analyser on board the Cassini spacecraft. To reconstruct the ejection dynamical properties of Saturnian stream particles, we adopt a backward tracing method with in–situ solar wind measurements to filter out the influence of the interplanetary magnetic field. Our results show that stream particles from Saturn have sizes ranged from 2 to 8 nm with ejection velocities between 50 and 200 $\mathrm{km\,s^{-1}}$. Moreover, the derived "source region" of stream particles in Saturn's E ring is indicative of dust charging condition profile in the magnetosphere. By using the Cassini magnetospheric plasma measurements as input, our ejection mode considers stochastic charging and well reproduces the dynamical properties of stream particles derived from backward simulations. An updated analysis of CDA stream–particle mass spectra suggests that in contrast to E ring particles, water ice is not the major component of Saturnian stream particles. Considering plasma sputtering as the dominant dust mass loss mechanism, the difference in sputtering yield between silicate and water ice combined with the "source region" concept not only confirms the E ring as the major source of Saturnian stream particles but also explains the compositional discrepancy. In the end, we discuss the role of dust particles as a mobile neutral reservoir in Saturn's magnetosphere which may be responsible to certain neutral / plasma observations made by the Cassini spacecraft.

5. SATURNIAN STREAM PARTICLES AS THE PROBE OF THE DUST-MAGNETOSPHERE INTERACTION

5.1 Introduction

Since decades, the interaction between dust particles, the plasma, and neutral molecules have been proposed to explain both the in-situ plasma electron measurements (Rymer *et al.*, 2008; Sittler *et al.*, 1983) and neutral molecule observations (Ip, 1997; Johnson *et al.*, 2008; Jurac *et al.*, 2001) in Saturn's magnetosphere. In respect of the plasma/neutral–surface interactions, small dust grains in the tenuous E ring could be as important as embedded icy moons due to their large total surface area and the great extension (between 3 and 20 R_S (Srama *et al.*, 2006), $1\,R_S = \text{Saturn radius} = 60,330\,\text{km}$). In a planetary magnetosphere, dust particles can act as both source (e.g. via sputtering) and obstacle to the magnetospheric plasma/neutrals and modify their spatial and energy distributions via mass and charge exchange processes.

From the dust–dynamics point of view, by transferring electric charges and momentum, the magnetospheric plasma is shown to have great influence on E ring dust grains. As the Lorentz force exerted on a dust particle is directly proportional to the number of charges it carries, the plasma, which determines the charging conditions, regulates the dust dynamics accordingly. Adopting $-5\,\text{V}$ surface potential for E ring dust grains loacted at Enceladus' orbit and considering the electromagnetic force, the radiation pressure, and the gravitational force from the oblate Saturn, Horányi *et al.* (1992) suggested that only particles of one micrometer radius are able to develop large orbital eccentricity and to populate the region between 3 to 8 R_S, the dimension of the E ring based on early optical observations (Showalter *et al.*, 1991). Acquiring momentum from co–rotating ions in the magnetosphere, the plasma drag effect enables E ring dust grains to propagate from the inner to the outer system and was proposed to explain the large extent of the E ring based on recent in–situ observations (Beckmann, 2008; Horányi *et al.*, 2008; Srama *et al.*, 2006).

In this work we focus on dust particles which have even smaller sizes – the stream particles. Stream particles are nano–meter scale dust particles ejected with speeds $\gtrsim 100\,\text{km}\,\text{s}^{-1}$ from both Jovian and Saturnian systems. Due to their nanometer scale, they are much more sensitive to the electromagnetic force than to gravity. Hence, their dynamics is governed not only by the electromagnetic field but also by the plasma environment via charging processes. Applying a proper method, the information that stream particles carry can provide further implications and constraints on the dust–plasma/neutral interaction at their source region (the Dust Astronomy concept (Grün *et al.*, 2001)). In this work we analyse Saturnian stream–particle measurements carried out by the Cosmic Dust Analyser (CDA) (Srama *et al.*, 2004) onboard Cassini spacecraft. Equipped with a time-of-flight (TOF) mass spectrometer, CDA can measure both the elemental composition and the dynamical properties of impinging dust grains. More instrument details will be described later in section 5.2.1. We first briefly introduce the discovery and unique properties of stream particles.

5.1.1 Jovian Stream Particles

The discovery of Jovian stream particles was made by the Ulysses spacecraft during its first Jupiter flyby in 1992 (Grün *et al.*, 1993). Soon after the discovery, the strong influence of the interplanetary magnetic field (IMF) on these sub–micron dust particles' dynamics was realized, and the IMF modulation due to solar rotation was suggested to cause the dust–stream 28 ± 3 day periodicity (Hamilton & Burns, 1993). Considering the outward pointing co–rotation electric field $\mathbf{E}_c$ in the Jovian magnetosphere, Horányi *et al.* (1993) demonstrated that with proper size the positively charged dust particles can acquire enough energy from $\mathbf{E}_c$ and escape the gravitational well of Jupiter with high velocity.

However, the extreme properties of stream particles were not really explained until the work by Zook *et al.* (1996). The authors performed backward tracing simulations to examine the 1992 Ulysses dust observations. Adopting in–situ IMF and solar wind speed measurements, the Lorentz force and gravitational forces from the Sun and Jupiter were taken into account for calculating the stream–particle trajectories. With an assumed Jupiter–origin, test particles were released from the spacecraft and traced backward in time to find the particle properties which are comparable to the observation. Their results showed that, for 11 registered dust streams, the measurements could only be reproduced by particles with radii between 5 and 15 nm and impact velocities exceeding $100\,\mathrm{km\,s^{-1}}$, which were about 10 times smaller and 5 to 10 times faster than values derived from the instrument impact signals. None of the dust detectors had been designed and calibrated for particles as small and fast as stream particles and the backward tracing results showed that the dynamical properties of stream particles could not be derived directly from the respective impact signals. The work by Zook *et al.* (1996) demonstrated impressively that the backward tracing method (with in–situ solar wind data) is an effective method to study the stream–particle dynamics.

After the Ulysses measurements outlined the stream particle dynamics in interplanetary space, the subsequent Galileo mission provided further details in the Jovian magnetosphere. The Galileo dust detector monitored the dust–stream activity since its approach to Jupiter in 1996. The continuous data acquisition between 1996 and 2003 allowed the study of time variability of stream particle activity. By applying a frequency analysis, the orbital period of the volcanic active moon Io was identified in the Galileo data set. This finding strongly suggests that Io is the main source of Jovian stream particles (Graps *et al.*, 2000). Besides Io's orbital period, ~ 5 and ~ 10 hours period features indicate a strong modulation of the stream particle activity by the Jovian magnetic field, which rotation axis is inclined with respect to Io's orbital plane (Grün *et al.*, 1998). It was also found out that, based on measurements in different Galileo orbits, the stream–particle ejection pattern showed a longitudinal asymmetry which probably resulted form discrepant charging conditions in the dawn–to–dusk asymmetric Io Plasma Torus (IPT) (Horányi *et al.*, 1997; Krüger *et al.*, 2003).

Aiming towards the Saturnian system, the Cassini-Huygens spacecraft was launched on October 15, 1997 and flew by Jupiter on December 30, 2000. Between 2000 and 2001, various instruments on–board Cassini spacecraft, including the CDA, performed collaborative observations with the Galileo spacecraft to study the Jovian system. Postberg *et al.* (2006) showed that mass spectra of Jovian stream particles obtained by CDA are dominated by sodium chloride with traces of sulfur, which proofed their origin from the volcanic plumes of Io. Furthermore, via the abundance of sodium ions the average size of Jovian stream particles was estimated to be 12 nm, which confirmed the simulation results by Zook *et al.* (1996). A preliminary dynamical analysis showed that the flux measured by CDA had a similar trend as the dust emission rate derived from the Galileo data (Hsu *et al.*, 2009a; Krüger *et al.*, 2003). Moreover, the ultraviolet emission of the IPT observed by the Cassini Ultraviolet Imaging Spectrograph (UVIS) also showed a pronounced correlation with the Galileo stream particle emission rate (Delamere *et al.*, 2004). It is likely that there is a more complex interaction/coupling between tiny dust particles and the magnetospheric neutral/plasma that has not yet been understood (Hsu *et al.*, 2009).

5.1.2   Saturnian Stream Particles

The existence of Saturnian stream particles was predicted first by Horányi (2000) based on the plasma model derived from the Voyager data. The discovery of Saturnian stream particles during Cassini's Saturn approach in 2004 (Kempf *et al.*, 2005a) confirmed the idea of the Saturnian system being the source of fast nanometer sized dust particles. At a distance of $1,400\,R_S$ $(0.56\,AU)$ away from Saturn, the CDA started to register faint impacts characterized by a short signal rise time. Based on the similarity between these impact signals and those of Jovian stream particles and also by the fact that the impact flux increased as the distance to Saturn decreased, these particles were recognized as Saturnian stream particles (Kempf *et al.*, 2005a).

The IMF conditions during Cassini's Saturn approach phase was monitored by the on–board magnetometer over more than 10 solar rotations (Jackman *et al.*, 2004, 2005). It was found that the IMF was highly structured and consisted of compression and rarefaction regions which were associated with the Corotation Interaction Regions (CIRs), a common solar wind structure between 2 and 10 AU resulting from the interaction between slow and fast solar wind. The field direction followed the Parker spiral model well and showed a two–sector structure during each solar rotation with the Heliospheric Current Sheet (HCS, where the field direction flips) embedded in the compression region (Jackman *et al.*, 2008).

Within $\sim 500\,R_S$ $(0.2\,AU)$ to Saturn, CDA observations showed a recurrent stream–particle impact pattern that correlated with the CIR rarefaction and compression regions. Impact bursts were observed during high–IMF–strength solar wind compres-

sion periods, while very faint impacts from the Saturn line–of–sight (LOS) direction were detected in low–IMF–strength rarefaction regions. The clustering of impacts in only one IMF sector implied that Saturnian stream particles were ejected in alignment with the planet's ring plane ($\pm 25°$). Impacts registered during quiet IMF periods were found to be caused by particles with sizes between 2 and 9 nm and ejection velocities $\geq 70\,\mathrm{km\,s}^{-1}$ (Hsu *et al.*, 2009a,b).

As the stream particles originate from the Saturnian system, one would expect them to have a similar composition to those of Saturnian ring particles. It has been known that the dense main rings and the tenuous E ring together with the embedded icy moons are mostly composed of pure water ice (Hillier *et al.*, 2007; Pilcher *et al.*, 1970). In contrast, the main element initially identified in mass spectra of Saturnian stream particles is silicon (Kempf *et al.*, 2005b) with only a small and occasional contribution of water ice. During Enceladus' plumes crossings in 2008, strong features coincided with plume jets' sources were detected by the Cassini Plasma Spectrometer (CAPS) and suggested to be caused by nanometer scales grains carrying opposite signs of electric charges. The nano–grain features extended further out from the Enceladus' Hill sphere and were therefore proposed to be the major source of Saturnian stream particles (Jones *et al.*, 2009). A comparison of the composition of these particles with Saturnian stream particles may help to investigate the actual source of stream particles detected outside Saturn's magnetosphere. Unfortunately, these particles are not yet accelerated by $\mathbf{E}_c$ and therefore the impact signals are simply too faint to be detected by CDA. Based on the dynamical and compositional analyses in this work, we will address this issue later in the discussion (section 5.5).

Using advanced knowledge and techniques of CDA spectra interpretation, a refined analysis of stream particle composition was carried out for this work. The main focus was to look for the presence of water in stream particles but also the presence of other components is considered. Together with the dynamical information, we make constraints on the chemical/physical properties and the likely source of Saturnian stream particles. More important, these information can provide further implication to the dust–neutral/plasma interaction in Saturn's magnetosphere. The data used in this study cover all the registered stream–particle impacts in 2004 and early 2005, i.e., the Cassini–Saturn approach phase and the first three orbits after Saturn Orbit Insertion (SOI). We start with the instrumentation and the stream–particle observation in section 5.2. In section 5.3 we present the backward–tracing simulation to give more precise constraints on the dynamical properties of Saturnian stream particles. Moreover, an axial-symmetric ejection model, which calculates the equation of motion and the charging equation of nanodust grains, is built for justifying our backward simulation. An update of chemical analysis for Saturnian stream particles is given in section 5.4. Results from various approaches will be discussed together with other Cassini findings in section 5.5. A summary concludes this paper in section 5.6.

5.2 CDA Saturnian Stream Particle Observations

5.2.1 Cosmic Dust Analyser

The Cosmic Dust Analyser (CDA) is the dust instrument aboard the Cassini space-craft (figure 5.1). CDA consists of two independent subsystems: the High Rate Detector (HRD) and the Dust Analyser (DA). The HRD is designed for monitoring the flux of micron–sized grains in high dust density environment. As it is too insensitive for stream–particle impacts, the HRD will not be discussed further. The DA is capable to measure the velocity, the mass, the charges, and the chemical composition of each single impinging dust grain. It is composed of following detectors: a charge sensing unit (QP detector) as the entrance grids of the instrument, an Impact Ionisation Detector (IID) similar to Ulysses/Galileo detectors, and a time-of-flight (TOF) mass spectrometer (Mass Analyser MA). To integrate the TOF mass spectrometer in to the DA the IID target is divided into two concentric hemispherical targets: an inner rhodium target of 16 cm in diameter (Chemical Analyser Target – CAT) and a large outer gold target of 41 cm in diameter (Impact Ionisation Target, IIT). The angular field of view (FOV) of the DA is $\pm 45°$ while the CAT FOV is only $\pm 28°$.

Figure 5.1: Technical drawing of the Cosmic Dust Analyzer. - The abbreviation of CDA components states as following: CAT - Chemical Analyzer Target, EG - Entrance Grids, HRD - High Rate Detector, IG - Ion Grids, IIT - Impact Ionization Target, MP - Multiplier.

As a dust particle impinges into the DA aperture, it will first pass through the entrance grids in front of the instrument. However, the charge carried on a stream particle is far less than the detection threshold of the charge sensor of 1 fC. The QP signal is therefore negligible in this work. Afterward, the particle may collide with either the inner rhodium target (CAT) or the outer gold target (IIT). The collision will transform the particle and the target material at least partially into impact plasma whose amount and expansion time scale provide information about the impactor's mass and impact speed [1]. To achieve this, the plasma generated on the impact target is separated into its constituents by an electric field between the targets and the ion grid. The plasma is then collected by individual electrodes and monitored by attached charge amplifiers (plasma electrons impact target, ions - ion grid). A DA measurement is started either when the impact charge collected in at least one of the electrodes exceeds a pre–set IID threshold or when the strength of a TOF mass line measured at the MA's multiplier in the center of the instrument exceeds the MA threshold. In normal cases, an impact event consists of one target signal (QC for CAT impacts or QT for IIT impacts) and one ion grid signal (QI). Once the dust grain hits on the CAT, the positive ions in the impact plasma will then be accelerated toward the MA and generate a TOF mass spectrum.

5.2.2 Stream particle Mass Spectra

However, most of Saturnian stream–particle impacts were too faint to trigger a recording event at CDA targets and the ion grid. Instead, the stream–particle event was always triggered by the multiplier signal of the H^+ mass line in the TOF spectrum. An analysis showed that hydrogen ions found in Jovian and Saturnian stream particle spectra most likely originates from target contamination since the yield was much higher than the number of atoms in the particles (Postberg *et al.*, 2006, 2009b). In other words, the sensitivity of CDA to detect stream particles is enhanced due to extra hydrogen ions released from the target by high energy–density stream–particle impacts. Taking advantage of the hydrogen contamination, CDA is capable to study Saturnian stream particles, whose impact signals were in general 10 times weaker than those of their Jovian counterpart. It is also worthy to mention: in spite of the improved sensitivity, the effective detection area of CDA for faint stream–particle impacts is limited to the CAT and therefore reduced by a factor of 6.5.

Two examples of stream particles' mass spectra are shown in figure 5.2. Figure 5.2a and 5.2b are CDA mass spectra of Jovian and Saturnian stream particles respectively. In both cases, the most prominent mass lines are H^+ C^+, and Rh^+. The rhodium clearly comes from the target material, while the carbon feature, similar to the

---

[1]As mentioned before, CDA has not been calibrated for stream–particle impacts. Therefore signals from DA detectors can not be interpreted quantitatively but only qualitatively. For example, faint signals imply tiny impactor mass and a short signal rise time infers fast impact velocity.

hydrogen line, most likely has a contamination origin (Postberg *et al.*, 2009a). Note that the H$^+$ lines in both examples usually triggers the event recording and are absent in most of stream–particle spectra. The spectra in figure 5.2 are triggered on impact and very rare. They are shown here to demonstrate the stream–particle mass lines.
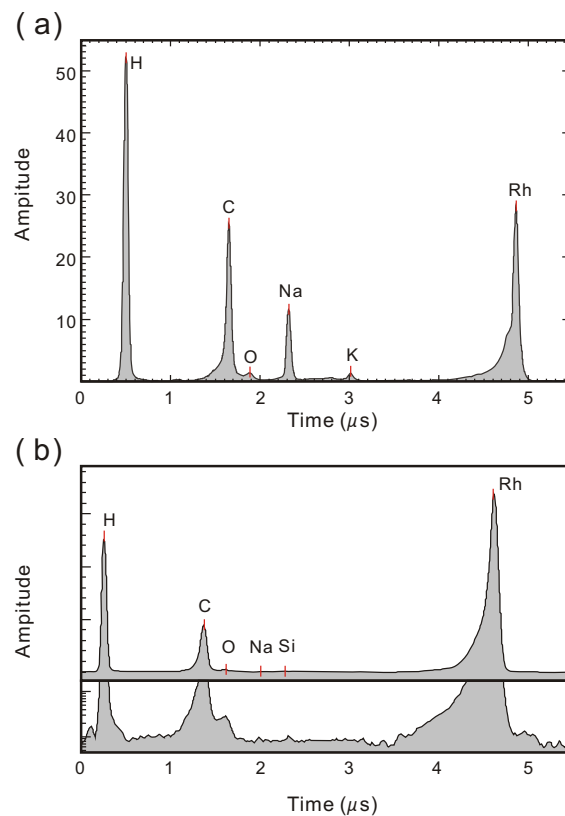
Figure 5.2: The CDA mass spectra of Jovian and Saturnian stream particle. - (a – Jovian and b – Saturnian stream particle.) Due to the high impact velocity and small impactor mass, stream–particle spectra are usually dominated by target and contaminant ions. (a) The mass spectrum is co–added from thirty Jovian stream particle spectra recorded during Cassini's Jupiter flyby in 2000. The Na$^+$, K$^+$, and probably O$^+$ lines are particle constituents. (b) Saturnian stream particle mass spectrum recorded in 2004. The lower panel is in logarithmic scale to show the weak lines. The main peaks in the spectrum are target (Rh$^+$) and target contamination ions (H$^+$, C$^+$).

As mainly composed of NaCl, the sodium can be easily recognized in the spectrum of Jovian stream particles (figure 5.2a). Another alkali metal feature, the K$^+$, also appears but with lower strength. In contrast, the even smaller Saturnian stream particles

almost exclusively produce target and contamination ions (i.e., H^+, C^+, and Rh^+ mass lines). Though the Si^+ line appears to be weak in figure 5.2b, its consistent presence in most of Saturnian particles' spectra suggests that the silicon is the main building block of Saturnian stream particles (Kempf *et al.*, 2005b).
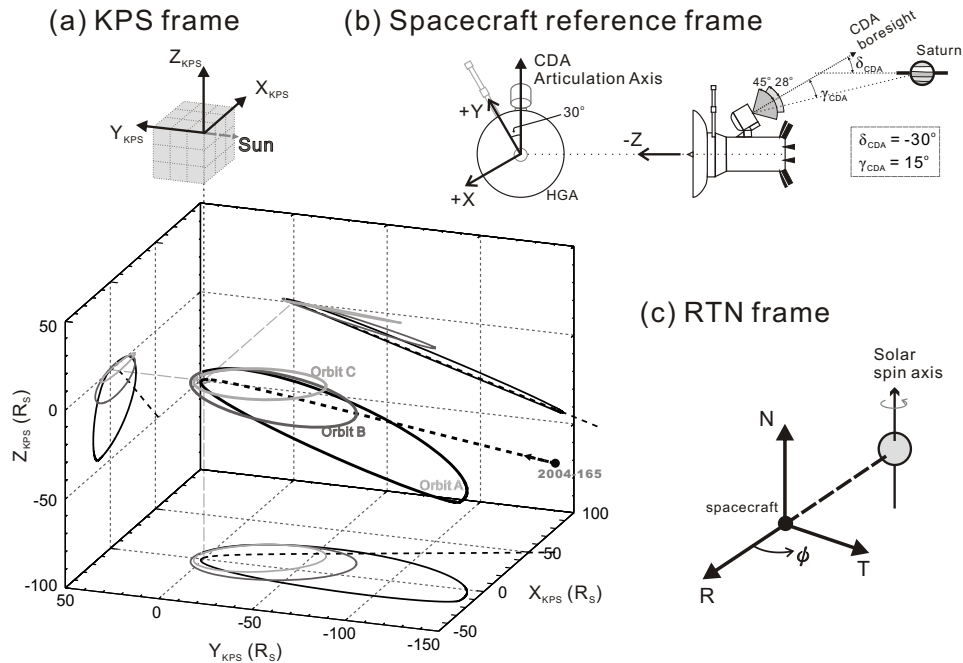
Figure 5.3: Sketch of Cassini's orbits and coordinates systems relevant in this study. - (a) The interplanetary trajectory (dash line) and the first three orbits of Cassini spacecraft after the Saturn Orbit Insertion. The orbit A, B, and C are shown in Saturn–centric KPS coordinates with unit of Saturn radius (R_S). *x–y* plane is parallel to the ring plane of Saturn. The Sun is in $+x$–z plane and its direction is indicated by the gray dash array. (b) The mounting geometry, the field of view, and an example of γ_{CDA} and δ_{CDA} angles are shown in the spacecraft reference frame. (c) The observer–centric RTN frame and the azimuthal angle ϕ which are used for describing the magnetic field data.

5.2.3 Observation Geometry

The Cassini stream–particle observation was greatly limited by the fact that the Cassini spacecraft is three–axis stabilized. While the stream particles' directionality change dramatically with the IMF conditions, data with bad angular coverage may lead to serous misinterpretation. Therefore, it is more important to have good angular cover-

age than deep exposure at limited directions.

The best observational configuration to obtain good angular coverage is by a spacecraft roll. During the data transmission, the High Gain Antenna (HGA) pointed toward the Earth and the spacecraft performed rolls along the spacecraft Z axis for 8 hours at a rate of about 2 revolutions per hour (see also figure 5.3). The data down–link took place approximately once every two days after the SOI. Thus the down–link rolls provided opportunity for temporally uniform stream–particle observations with large angular coverage. Moreover, consider the detector's FOV, the plane that CDA scanned through during the down–link roll was sensitive to the stream–particle directionality change caused by the IMF (Hsu *et al.*, 2009b). As the limitation of the angular coverage is eased by spacecraft rolls, it is fair to believe that there is no selection bias in the CDA stream–particle measurements and the registered particles are representative samples regarding the chemical and dynamical properties.

Two coordinates systems are used in this work: the Saturn–centric KPS system and the observer–centric RTN system. Both coordinates systems are right–handed. The KPS is formed by X (+X-Z plane contains the Sun), Y (completes the right–hand set), and Z (parallel to Saturn's pole axis). The RTN frame is composed of: **R** points from the Sun to the spacecraft. The tangential component **T** lies in the solar equatorial plane and is the vector product of the solar rotation axis and **R**. The normal component **N**, which completes the right–handed triad, is the projection of solar rotational axis (see also figure 5.3).

5.2.4   Impact Patterns and the IMF Modulation

Figure 5.3 shows the instrument configuration together with the first three orbits of Cassini spacecraft in the KPS system. From orbit A to orbit C, the apocenter decreased from $151\,R_S$ to $60\,R_S$ and the inclination varied from $-16.9°$ to $-4.3°$. During these three orbits the spacecraft was inside the solar wind most of the time, it provided additional six months to study the stream–particle–IMF interaction at the vicinity of Saturn's magnetosphere. Figure 5.4 shows the stream–particle observations during the orbits A, B, and C together with the magnetometer (MAG) measurements. The time periods when the spacecraft was inside Saturn's magnetosphere are shaded in gray. As the stream–particle directionality changed significantly with IMF, the instrument orientation is expressed by two angles to demonstrate the IMF influence: the δ_{CDA} and the γ_{CDA} angles (see also figure 5.3). The δ_{CDA} is the elevation angle between the instrument boresight and Saturn's ring plane, $\delta_{CDA} = -90°$ when the instrument points parallel to the north of Saturn's rotation axis. The γ_{CDA} is the angular separation between the detector boresight and Saturn direction, $\gamma_{CDA} = 0°$ indicates
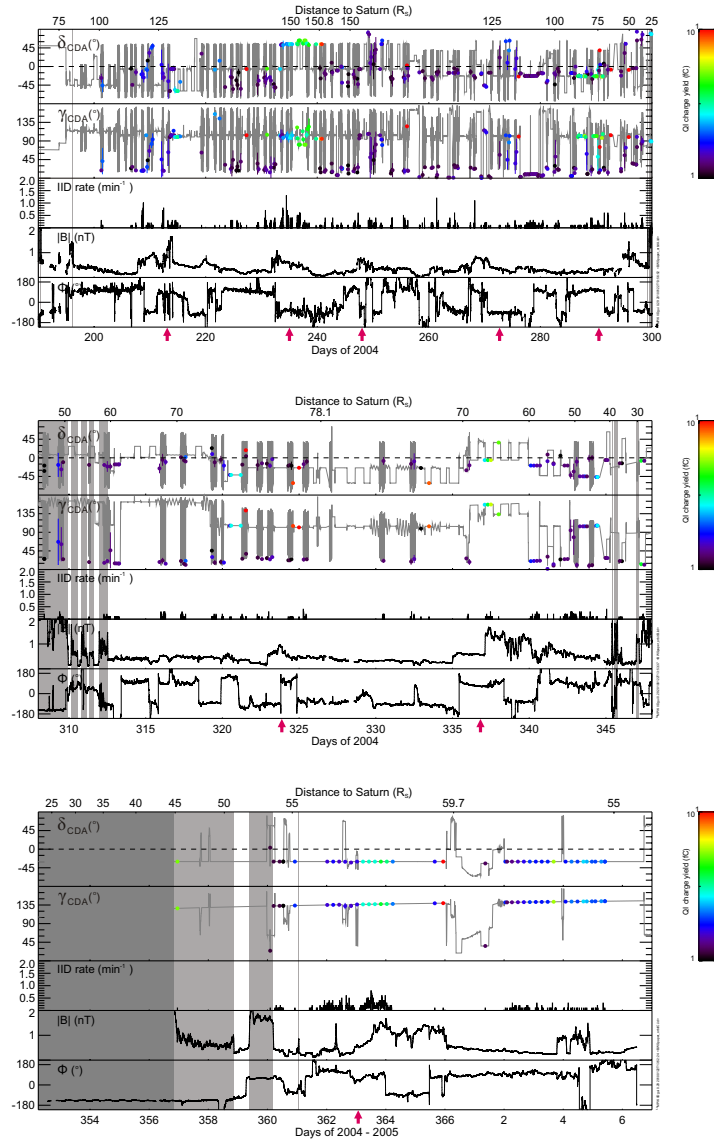
Figure 5.4: CDA stream particle observations during first three orbits after Saturn Orbit Insertion. - From top to bottom the panels are: the stream–particle directionality expressed by CDA–ring plane angle (δ_{CDA}) and CDA–Saturn angle (γ_{CDA}), impact rate (mid–panel), the magnetic field strength and the azimuthal direction ϕ. In the first two panels impacts are binned and color–coded with the ion grid signals (QI). The time and the distance of Cassini spacecraft to Saturn are also shown in horizontal axes. In general, based on the magnetic field and the impact strengths, stream particle impacts can be divided into two categories: weak impacts detected from direction close to Saturn line of sight during low magnetic field strength period, and strong impacts detected with large γ_{CDA} during high magnetic field periods. The identified dust bursts are marked by purplish red arrows under each plot. Periods when the spacecraft was inside of Saturn's magnetosphere and magnetosheath are shaded with gray and light–gray areas.

that the detector's boresight coincides with the spacecraft–Saturn LOS.

In the upper two panels of figure 5.4, binned stream–particle impacts are color–coded with QI signal strength and over–plotted on the CDA δ_{CDA} and γ_{CDA} profile. The impact flux of stream particles is shown in the middle panel. The two bottom panels are the magnetic field strength and the azimuthal direction ϕ measured by MAG. The angle ϕ is the azimuthal angle of magnetic field vector in the RTN frame as shown in figure 5.3c.

Because the CDA angular coverage during orbit C was extremely limited, we focus here on the observation during orbit A and B. Different from observations during Cassini's Saturn approach phase, stream–particle activity in orbit A and B did not show a correlation with the IMF sector structure, i.e., no impact–clustering during $\phi > 0°$ periods. Instead CDA observed constantly faint impacts (QI ~ 1 fC) from Saturn LOS direction. Stream particles spent less time under the IMF influence and still preserved their original momenta (close aligned with the ring plane) at the time of detection because the spacecraft was closer to Saturn and its ring plane after the SOI. Therefore most of these faint impacts were detected along Saturn LOS, with δ_{CDA} similar to spacecraft latitude ($\sim -17°$ and $\sim -12°$ for orbit A and B, respectively). In contrast, bursts of strong impacts still correlated with the high–IMF strength periods (e.g., between DOY 233 to 240), as the observation during the pre–SOI phase. Impacts during the bursts were characterized by higher impact charge yield and large γ_{CDA} angle. Time durations of impact bursts were similar to the corresponding high–IMF periods (between 5 to 10 days). These facts again suggest that the "local acceleration" of stream particles during the high–IMF periods is the key to produce the "dust stream" phenomenon (Hsu *et al.*, 2009b; Kempf *et al.*, 2005a) and agree with the Ulysses' observation during its second Jupiter flyby at the same period (Flandes & Krüger, 2007).

During orbit C, CDA pointed toward directions far away from the Saturn LOS most of the time. Interestingly, two impact bursts were detected: the first burst took place around day 362 and 364 of 2004 and the second one was between day 002 to 006 of 2005 (figure 5.5). The first burst showed characteristics of stream–particle interaction in a CIR compression region, such as increasing impact charge yield and IIT–to–CAT impact ratio with IMF strength. However, due to the bad angular coverage, the exact cause of these features can not be simply determined. Unlike the first burst, the second burst consisted of only faint impacts. About 90% of them were CAT impacts, which agreed with the enhancement of CAT sensitivity by the H^+ triggering mechanism. Nevertheless, no explanation can be made for the cause of this faint, non–Saturn LOS impact component.

Another important point is the recurrence and the periodicity of impact bursts. Due to the complex instrument orientation, it is very difficult to apply a frequency analysis to CDA measurements. However, features of impact bursts due to IMF influence, like

the change of impact directions and the enhanced impact charge yield, can still be recognized. As the solar wind structure recurred after each solar rotation (Jackman *et al.*, 2004), we found that impact bursts occurred with similar frequency. The bursts are marked with red arrows in figure 5.4. Since the coincidence of timing, we presume that the first impact burst during orbit C most likely result from the interaction with the CIR–associated compression region.
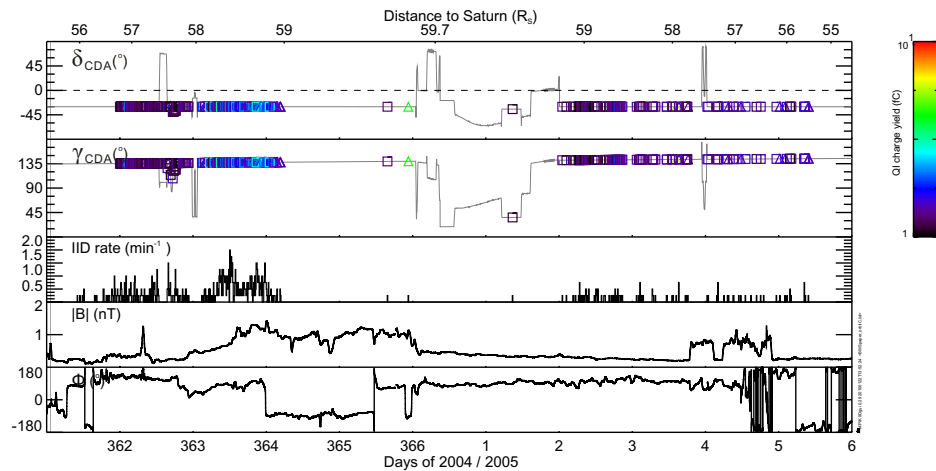
Figure 5.5: Saturnian stream particle observation during orbit C - presented together with magnetic field strength and direction. Different from figure 5.4, in this figure each identified stream particle during this period is plotted. Squires represent CAT impacts while triangles are impacts on the big target, IIT. Two dust bursts were detected with large γ_{CDA} angle. The first burst took place during day 362 and 365 of 2004 showed increasing impact charge and IID–to–CAT impact ratio with time, which resembles the stream–particle–CIR compression interaction. The second one happened during day 2 and 6 of 2005, however, showed only weak impacts.

5.3   Stream Particle Dynamics

Following the preliminary dynamical analysis of pre–SOI measurements presented by Hsu *et al.* (2009b), we adopt a larger CDA Saturnian stream–particle dataset that contains all 2004 detections for a more detail backward simulation. The backward tracing has been proven to be an effective method for studying the dynamics of Lorentz force–sensitive dust particles (Zook *et al.*, 1996). Based on Cassini dust and solar wind measurements, a similar approach is applied for for Saturnian stream particles. The backward simulation not only is used for deriving particles' dynamical properties but also provides clues about their origin.

5.3.1 Backward Simulation

The main idea of backward tracing method is to use in–situ IMF and solar wind measurements as constraints for studying stream–particle dynamics. In interplanetary space, the IMF acts as a giant mass–spectrometer which shapes the trajectories of dust stream particles depending on the IMF configuration and particle properties. Therefore, detections of stream particles along the spacecraft trajectory are actually the outcomes of combined effects of initial particle properties and time–varying solar wind conditions. By reversing the direction of the electromagnetic force based on IMF measurements and by integrating backward in time, we can (at least partially) cancel out the solar wind influence and derive the stream–particle dynamic properties (which are outside the instrument calibration range).

For each registered stream particle, we start the simulation at the time of impact detection. Test particles are launched from the spacecraft position with velocity vectors along the instrument FOV. We divide the CAT (IIT) FOV into 16 (25) directions along concentric cones (figure 5.6b). Particles launched along each direction have various combinations of impact velocities ($\mathbf{v}_{imp}$) and charge–to–mass ratios (Q_d/m_d). In our simulation, $\mathbf{v}_{imp}$ is set to be the initial velocity of test particles and ranges from 40 to $350\,\mathrm{km\,s^{-1}}$ with 11 intervals. The charge–to–mass ratio ranges from 50 to $32{,}000\,\mathrm{C\,kg^{-1}}$ with 15 intervals. In other words, there are $2{,}640$ ($4{,}125$) test particles for each CAT (IIT) impact in our simulation.

Instead of using the grain size, we chose to scan through the charge–to–mass ratio:

$$\frac{Q_d}{m_d} = \frac{3\varepsilon_0\phi_d}{\rho_d s_d^2},\tag{5.1}$$

where ε_0 is the vacuum permittivity, s_d is the radius of dust grain, ρ_d is the dust bulk density, and ϕ_d is the dust grain electrostatic surface potential, which is $\phi_d = Q_d/4\pi\varepsilon_0 s_d$. As can be seen in Eq. (5.1), Q_d/m_d couples these three free parameters s_d, ρ_d and ϕ_d together and it is also the quantity that directly involves in the calculation of the equation of motion (Eq. (5.2)). Therefore, we adopt Q_d/m_d in our simulation to reduce the parameter space and to save computation time. The Q_d/m_d range of dust grains used in our simulation is equivalent to a radius range of 51.5 to 2.0 nm (assuming $\rho_d = 1.0\,\mathrm{kg\,m^{-3}}$ and $\phi_d = +5\,\mathrm{V}$), or m_d/Q_d range of $\sim 2\times 10^6$ to $3{,}000$ amu/q.

With the initial conditions given above, the equation of motion of each test particle is then numerically integrated backward in time. Considering the Lorentz force together with the gravitational force from the Sun and Saturn, the acceleration of a charged dust particle is

$$\mathbf{a_d} = -\frac{GM_\odot \mathbf{r}_\odot}{r_\odot^{\,3}} - \frac{GM_S \mathbf{r_S}}{r_S^3} + \frac{Q_d}{m_d}(\mathbf{v}\times\mathbf{B}).\tag{5.2}$$

G is the gravitation constant, $M_\odot$ $(1.989 \cdot 10^{30}\,\mathrm{kg})$ is the mass of the sun, M_S $(5.685 \times 10^{26}\,\mathrm{kg})$ is the mass of Saturn. $\mathbf{r}_\odot$ and $\mathbf{r_S}$ are the position vectors from the Sun and Saturn to the dust grain. $\mathbf{B}$ is the interplanetary magnetic field vector, and $\mathbf{v} = \mathbf{v_d} - \mathbf{v_{sw}}$, where $\mathbf{v_d}$ and $\mathbf{v_{sw}}$ are the velocity vectors of the dust grain and the solar wind. Since the equation of motion is integrated backward in time, the directions of $\mathbf{v_{sw}}$ and $\mathbf{B}$ need to be reversed in the calculation.

The first two terms at the right–hand side of Eq. (5.2) are gravitational forces from the Sun and Saturn. The third term is the Lorentz force, which exceeds gravitational forces by orders of magnitude for stream particles. The in–situ Cassini solar wind measurements are adopted for calculating the electromagnetic force. We use five–minute averaged Cassini MAG data for the IMF and the one–hour temporal resolution solar wind speed derived from the phase space density cut–off of He^+ measured by Cassini MIMI/CHEMS (Hill *et al.*, 2004). During the period of interest, the solar wind velocity varied between 400 and 600 $\mathrm{km\,s^{-1}}$. The IMF ranged from $\leq 0.1\,\mathrm{nT}$ in rarefaction regions to $\gtrsim 1\,\mathrm{nT}$ in the compressed solar wind.

For each time step, the measured $\mathbf{B}$ and v_{sw} are extrapolated from the spacecraft location to the location of the test particle with following assumptions: (1) solar wind plasma flows radially outward from the Sun with measured speed, (2) the IMF structure stays intact while the solar wind plasma is moving outward, (3) the solar wind conditions at the position of the test particle at t_{now} are the Cassini measurements at t', which can be solved by :

$$r'_\odot = \sum_{t=t'}^{t_{now}} v_{sw} \times 5\,min. \tag{5.3}$$

$r'_\odot$ is the distance between the dust grain and the spacecraft, projected on to the spacecraft–Sun line at t_{now} (positive toward the Sun in the simulation). Eq. (5.3) simply uses the solar wind speed measurements to transform the distance between the spacecraft and the test particle to the solar wind propagation time. For example, for a test particle located further from the Sun than the spacecraft, t' is always smaller than t_{now}.

The radial component (with respect to the Sun) of the particle velocity (v_{dR}) determines the time that a particle spends in a solar wind parcel. Since stream particles can reach speeds comparable to the solar wind, the size of the time steps needs to be evaluated with care. Imagine a particle that moves radially outward from the Sun with the speed of solar wind (i.e., co–moving with the solar wind plasma), except the decreasing strength with increasing distance to the Sun, the magnetic field along the particle trajectory will be approximately constant. Since the spacecraft moves a lot slower than the solar wind, the Cassini solar wind speed measurements can be approximated as real values. With the solar wind speed (the extrapolation follows the method described above) and the dust velocity, the length of a time step (Δt) can be determined as: $\Delta t = 5min \times v_{sw}/(v_{sw} + v_{dR})$. In the simulation, v_{dR} is positive toward the

sun direction.

The procedure described above is basically the same as in Zook *et al.* (1996). It allows applying the in–situ solar wind measurements to calculate the Lorentz force at any given location without engaging in expensive MHD (Magnetohydrodynamics) computations. In fact, solar wind structures re–organized themselves as moving outward from the Sun, for example, CIRs, the common solar wind structures within 10 AU (Gazis *et al.*, 1999). They form when fast solar wind streams overtake slow streams, and shock waves and compression–rarefaction structures are formed. Our solar wind propagation method is not tenable at regions either close to CIR–related shocks or within highly fluctuated solar wind compressions. As mentioned before, in 2004, the solar wind was highly structured and consisted of rarefactions and compressions. In rarefaction solar wind, the variation of **B** is generally small, which is ideal for the backward simulation. However, the field strength in solar wind compressions varied largely in a short time scale. From the CDA–measurement aspect, as shown in figure 5.4, 5.5, and in (Hsu *et al.*, 2009a,b), Saturnian stream particles were accelerated significantly in solar wind compressions which results in large γ_{CDA} (CDA–Saturn angle) detections. Therefore, to assure the accuracy of our backward simulation results, we can simply eliminate impacts with large γ_{CDA} (i.e., detections in solar wind compressions) from the impact list of the simulation.

Another limitation of the backward simulation relates to the dust charging. Since the charging process is un–reversible, performing backward simulation implies a premise of constant dust charge. At the vicinity of Saturn's orbit, it takes ~ 3 days for a 9 nm dust grain to collect a single solar wind electron and to emit a single photo-electron produced by the solar UV (assuming plasma density of $5 \cdot 10^4 \, \text{m}^{-3}$ and a temperature of 1 eV). The long charging time means that in most cases the electrostatic charge carried by a stream particle at time of impact is the same as when it left the dense plasma region in the Saturnian magnetosphere. The difference on Q_d/m_d induced by one additional elemental charge is 3% for 9.0 nm grains and 20% for 2 nm grains.

Since the main idea of backward simulation is to use the solar wind measurements as constraints for the stream–particle dynamics, we consider only impacts registered when the spacecraft was outside Saturn's magnetosphere and thus exposed to the solar wind (the un–shaped areas in figure 5.4). Among $3,258$ impacts recorded in 2004, $2,375$ are simulated (pre–SOI: 784, post–SOI: 1591). In the simulations, test particles that reach given "sphere" around Saturn are ranked as possible solutions. In general the "Saturn sphere" has angular size of $\sim 30°$ seen from the spacecraft location.

An example of solutions from a CAT impact registered at 2004-330/12:50:57 is shown in figure 5.6. Squares on the dotted–line–grid in figure 5.6a represent our parameter space and are color–coded with the number of test particles that were successfully traced backward from the spacecraft to Saturn for this impact event. A similar

color–code is applied on the CDA–FOV grid demonstrated in figure 5.6b. The information from this impact is also listed. The backward tracing result of this event comprises multiple solutions, which are often seen in results of small γ_{CDA} impacts. In fact, only very few events have one unique solution (ex. impact at 2004-214T20:36:24 shown in figure 5.6c and figure 5.6d). There are 409 impact events where we find no solution at all (pre–SOI: 258, post–SOI: 151). Most of the no–solution impacts are detected at large γ_{CDA} and therefore are not included in the final result (describe below). To find the factual solutions, we adopt a two–step strategy – elimination and intersection. At first, we eliminate solutions with initial conditions that are genetically unsuitable for our backward tracing code. Secondly, we add valid solutions of all Saturnian stream–particle impacts together to find statistical meaningful results.
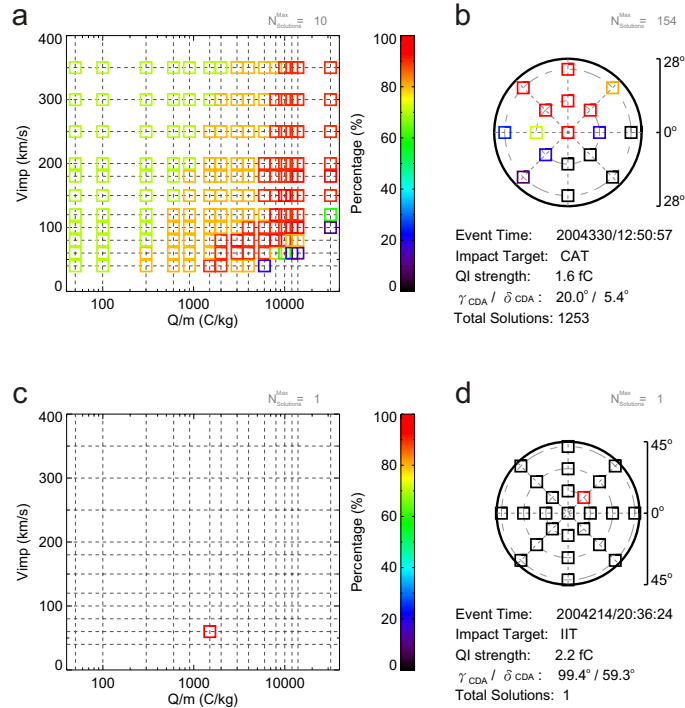
Figure 5.6: Solutions of backward simulation of two stream–particle impact events. - Plot a is the solutions of an CAT impact detected at 2004–330/12:50:57. Plot b shows the result of an IIT impact registered at 2004-214/20:36:24. The left panels of these two plots show the number of solutions on the charge–to–mass ratio–impact velocity parameter space while the panels at the right–hand side show the instrument field of view grid used in our simulation with overlapped number of solutions. Other information related to the impact event, such as QI amplitude, directionality, and number of solutions obtained from the backward tracing simulations, are also listed.

5. SATURNIAN STREAM PARTICLES AS THE PROBE OF THE DUST-MAGNETOSPHERE INTERACTION

As mentioned above, our solar wind model may not be fully applicable to large γ_{CDA} impacts (i.e., particles that traveled through solar wind compressions). Hence, we first limit our samples only to impacts detected at $\gamma_{CDA} \leqslant 60°$. Moreover, considering the artificial "Saturn sphere", the test particles whose initial velocity vectors point towards the "Saturn sphere" will easily fulfill our criterion for a successful backward tracing. This significantly biases our simulation results especially for solutions with small Q_d/m_d (less influenced by the Lorentz force) and leads to bad resolution in terms of refining the stream–particle dynamic properties in the parameter space. Therefore, only impacts with $\gamma_{CDA} \leqslant 60°$ whose solutions are derived from particles launched with direction $> 15°$ away from spacecraft–Saturn direction are taken into the next procedure – the solution intersection.

Statistics related to impacts used for the final analysis are shown in figure 5.7a–d. The ion yield measured at QI (bold line in figure 5.7a) is below 5 fC, which is typical for detections during quiet IMF periods. The γ_{CDA} of the impacts show a bimodal distribution (figure 5.7b): the two γ_{CDA} groups correspond to weak and strong IMF–influenced impacts. Only solutions from the weak IMF–influenced impacts are used (bold line in figure 5.7b). Figure 5.7c shows the numbers of solutions as function of angular separation between the initial particle velocity vector and the Saturn LOS. Applying all selection criteria, figure 5.7d shows numbers of solutions in each $\mathbf{v}_{imp}$– Q_d/m_d set (normalized to the maximum and expressed in percentage). The area filled with red squares represents the most probable impact properties for Saturnian stream particles detected by CDA. This area roughly centers along the line of $v_{imp} = 0.011 \times Q_d/m_d + 30$, and extends from $Q_d/m_d \simeq 1,000\,\mathrm{C\,kg^{-1}}$ and $v_{imp} = 40\,\mathrm{km\,s^{-1}}$ to the upper–right conner of the parameter space. Notice that the numbers of successful tracing events for big and fast particle bins (upper left part of the figure 5.7d) are only 20% less than the peak value in the red area. However, these solutions are from parameter sets that are not sensitive to the electromagnetic force and may be beyond the capability of the backward tracing method. Hence, it is reasonable to assume that most, if not all, of them are unrealistic solutions which just can not be filtered out by our selection criteria.

One big advantage of employing backward simulation technique is that it helps to wipe out the influence inserted by the Lorentz force on stream particles' dynamics and to recover the initial dynamical properties with which they were ejected from the system. We then take the velocity vectors of each particle at its closest approach to Saturn as their ejection velocities. By means of that, we can transform our solutions from the frame of v_{imp} in figure 5.7d to v_{ex}. Figure 5.7e to figure 5.7h show the results of the backward simulation. In figure 5.7e, the number of impacts with solutions which fit in each v_{ex}–Q_d/m_d bin is counted, normalized to the total number of selected impacts, and shown in percentage. This plot basically shows the likelihood of certain stream–particle properties right after the ejection from the Saturnian system. Similar to figure 5.7d, high likelihood bins ($> 60\%$) concentrate along the belt across bottom–middle to the upper–right corner. Figures 5.7f and 5.7g show histograms of Q_d/m_d

and v_{ex} separately. The simulations suggest that the Saturnian stream particles in general have Q_d/m_d greater than $1,000\,\mathrm{C\,kg^{-1}}$ (smaller than $\sim 11\,\mathrm{nm}$) with ejection velocity between 50 to $200\,\mathrm{km\,s^{-1}}$. This agrees with the estimates by Hsu *et al.* (2009a,b).

Before going further to the backward tracing results, a few remarks should be made concerning the stream–particle ejection process. As described before, positively charged particles with proper size can acquire enough energy from the outward pointing $\mathbf{E}_c$ to overcome the gravitational force and finally escape from the system. Therefore, the equation of energy conservation can be written as:

$$\frac{1}{2}m_d v_{ex}^2 = -\frac{GM_S m_d}{2r_0} + \int_{r_0}^{r_{ms}} f_{co} \cdot Q_d \cdot \mathbf{E}_c \, dr. \tag{5.4}$$

At the right–hand side, the first term is the total energy of a dust particle with initial Keplerian motion. The second term is the energy that particles acquire from the co–rotation electric field. The E field can be expressed as $\mathbf{E}_c = -\mathbf{V}_{co} \times \mathbf{B}$, where $\mathbf{V}_{co}$ is the corotation velocity and $\mathbf{B}$ is the magnetic field of Saturn. The f_{co} is the fraction of corotation, r is the distance to Saturn, r_{ms} is the boundary of the Saturnian magnetosphere, and r_0 is the radial distance where a particle starts to be accelerated by $\mathbf{E}_c$.

Assuming that the magnetic field of Saturn is a perfect dipole and f_{co} is independent of radial distance, we can express Eq. (5.4) as funtion of Q_d/m_d and v_{ex}:

$$r_0 = \frac{\frac{Q_d}{m_d} \cdot f_{co} \cdot A - B}{v_{ex}^2 + \frac{Q_d}{m_d} \cdot f_{co} \cdot C}, \tag{5.5}$$

where $A = 2 \cdot \Omega \cdot B_0 \cdot \mathrm{R_S}^3$, $B = G \cdot M_S$, and $C = A/r_{ms}$. $\Omega = 1.64 \times 10^{-4} sec^{-1}$, $B_0 = 21.535 \mu T$, and $\mathrm{R_S} = 6.033 \times 10^7\,m$ are the rotation rate, the equatorial magnetic field strength, and the radius of Saturn, respectively. With Eq. (5.5), we can interpret our solutions from the backward tracing simulation as the likelihood of the region from which particles start to be accelerated, also called the "source region".

Figure 5.7h shows the likelihood of the stream–particle source region along the equatorial plane of Saturn's magnetosphere after applying Eq. (5.5) to the backward tracing results. The reason of the limitation in the equatorial region is that in the Eq. (5.5) the latitude is not taken into consideration. Nevertheless, it is still sufficient for our purpose since both model calculations (Horányi, 2000) and observations (Hsu *et al.*, 2009b) suggest that Saturnian stream particles were ejected along the magnetic equator. As a consequence, for deriving the source region, we only use solutions with velocity vectors which lie within $\pm 30°$ from the Saturn ring plane.

As apparent in figure 5.7h, the most likely source region is close to Rhea's orbit. This result is intriguing since all the known dust reservoirs are located inside of $4\,\mathrm{R_S}$
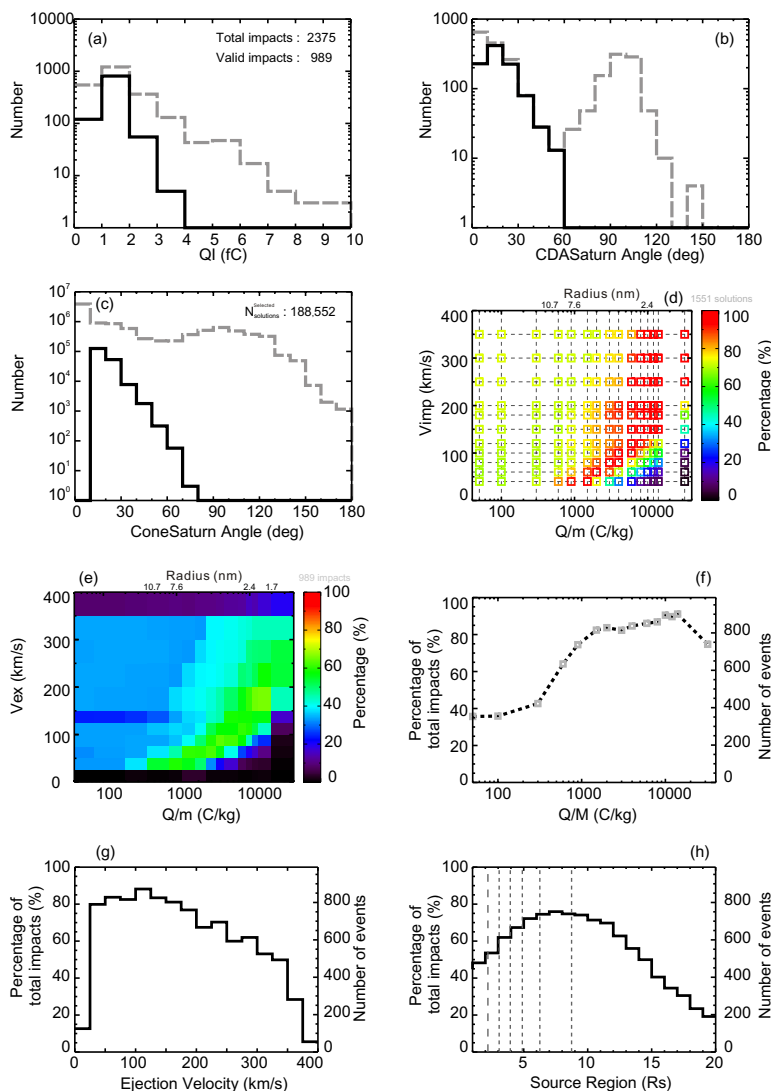
Figure 5.7: Statistics of the data and results of backward tracing simulation. - All dataset/simulations (gray dash line) and the selected part (black solid line) are both shown in histograms of (a) impact charge yield (QI signal), (b) impact CDA–Saturn angle (γ_{CDA}), and (c) number of solutions as function of angular separation between particles' initial velocity vectors and Saturn direction. From 989 out of 2,375 impacts are selected and in total 188,552 solutions are used to in (d), the number of solutions of each charge–to–mass ratio–impact velocity gird. The maximal solutions in one single bin are 1551. From (e) to (h) are the backward simulation results. After filtering out the IMF influence, plot (d) is transformed into (e), which shows the likelihood of the charge–to–mass ratio and the ejection velocity of detected stream particles. (f) and (g) are the likelihood of stream–particle charge–to–mass ratio and ejection velocity. Finally, (h) is the most likely acceleration–starting location, or we called the "source region" of Saturnian stream particles. See text for more detail.

(the dense part of the E ring, active Enceladus plumes, and the main rings). However, it coincides with CDA charge measurements which indicate the surface potential of E ring dust grains is negative inside and turns positive outside Rhea's orbit (Kempf *et al.*, 2006). For being accelerated by $\mathbf{E}_c$, dust particles need to be charged positively. In other words, nano–meter size dust particles could only start to be accelerated outward outside of Rhea's orbit, if the surface potential of them follows the same equilibrium potential as micron–sized grains measured by CDA.

5.3.2 Ejection Model

To examine our backward tracing results, we construct a stream particle ejection model to simulate the ejection process. In contrast to the situation at Jupiter where most of the stream particles are ejected in few hours after condensing in ionian volcanic plumes (Horányi *et al.*, 1997), no such active nanodust–particle source is located at the "source region" ($\sim 8\,R_S$) derived from the backward simulation in Saturn's magnetosphere. Therefore, we consider a new scenario discussed by Kempf et al. (manuscript in preparation), that stream particles are actually the dynamically evolved old E ring particles (the nanodust particles found in Enceladus' plumes by Jones *et al.* (2009) will be discussed later).

While orbiting Saturn, the E ring dust grains are sputtered by magnetospheric ions and their mass is converted into neutral molecules/atoms and subsequent plasma. As the sputtering yield depends on the target geometry and can be enhanced for very small grains, the sputtering life time of dust particles is size dependent. At Enceladus' orbit, the life time of E ring grains is estimated to be about 50, 5, and 0.5 years for 1.0, 0.1, and 0.01 μm grains respectively (Jurac *et al.*, 2001). Since the sputtering rate between 4 to 8 R_S does not vary much (within a factor of 3, (Johnson *et al.*, 2008)), sub–μm to μm sized E ring particles will fall into nanodust category within few years after ejection from Enceladus' plumes, if not colliding with Saturn's icy satellites or the A ring. Moreover, the assumption of sputtering–origin also agrees with the formation scenario inferred from the CDA composition analysis, i.e., Saturnian stream particles are the silicate impurities of E ring particles and are ultimately ejected from the system (Kempf *et al.*, 2005b; Postberg *et al.*, 2008).

As indicated by CDA charge measurements (Kempf *et al.*, 2006), the equilibrium potential of E ring dust grains at the "source region" is positive. Since it is certain that positively charged nanodust particles can acquire enough energy from the outward pointed co–rotational electric field and escape from the system, a more important question is how the negatively charged dust grains turn their electric polarity to positive in the negative–charging environment. Here we present an axial–symmetric ejection model, which calculates the charging and dynamical evolution simultaneously for nano–meter sized dust particles in Saturn's magnetosphere. Since the electric po-

larity of dust grains is the key issue, we have paid special attention on simulating the charging process of tiny dust grains. First, we adopt the latest plasma models based on Cassini measurements in our calculation. In particular, the charging currents of two Lorentzian (κ distribution) electron populations are considered. Second, due to the small size of stream particles and the quantized nature of electric charge, we assume that the dust charging follows the Poisson process. The number of charging events in each time step can be calculated by knowing the rate of each current. This approach is used for fitting laboratory measurements and is a realistic way to calculate the stochastic charge variation of tiny dust grains. Before going further into the model, we shall discuss the basic concept of the dust charging calculation.

As having been extensively discussed in the literature ((Horányi, 1996; Kempf *et al.*, 2006; Whipple, 1981)), the time evolution of electric charges carried on a dust grain (Q_d) in a plasma environment is:

$$\frac{dQ_d}{dt} = J_e + J_i + J_\nu + J_{sec}. \tag{5.6}$$

The J_e and J_i are the electron and ion collection currents, i.e, the flux of electron and ion that a dust grain captures from the ambient plasma. J_ν is the current that describe the flux of photo–electron induced by solar UV photons. J_{sec} is secondary electron emission current, which describes the flux of secondary electron emission caused by energetic electrons. The electron current is a negative current while the others are positive currents. The current strengths depend on various conditions, such as plasma characteristics (the composition, the number density, the temperature, and the energy distribution of plasma), the solar UV photon flux (effect on J_ν), and dust grain properties (the surface potential ϕ, the material properties, the dust grain–plasma relative speed ... etc.).

The dust charging calculation in this work basically follows the Orbit Motion Limit (OML) theory which is valid under condition of $s_d \ll \lambda_D \ll D_d$ where the s_d, λ_D, and D_d are the grain radius, the plasma Debye length, and the inter–grain distance respectively. Except for regions at the dense main ring, the F ring (Goertz & Ip, 1984), and possibly the densest part of the E ring (Wahlund *et al.*, 2009), the OML condition is fulfilled in Saturn's magnetosphere.

As Io to Jupiter, the tiny icy moon Enceladus is the major neutral / plasma source in Saturn's magnetosphere (Hansen *et al.*, 2006). However, different from the Jovian magnetosphere, the neutral gas density exceeds plasma density by more than an order of magnitude across the Saturnian magnetosphere. Every second Enceladus emits a few hundred kilograms of water vapor into the system and only about 10% are ionized by electron impact or photo–ionization (Sittler *et al.*, 2008). The density of neutral atoms/molecules (such as O and OH) at Enceladus is estimated to be $\sim 700 \text{cm}^{-3}$ (Melin *et al.*, 2009) or even $1,000 \text{cm}^{-3}$ (Jurac *et al.*, 2002), i.e., more than 10 times higher than the ion density. Within the dense Enceladus neutral cloud, the electron

temperature is low ($< 1\,\mathrm{eV}$) and the charge–exchange between neutral–ion collisions is the dominant mechanism to re–distribute neutrals from Enceladus into the broader torus (between ~ 3 to $7\,\mathrm{R_S}$). Further outward from Enceladus, due to the increase of electron temperature, more ions are to be produced by the electron–impact ionization process. The plasma ions and electrons formed in the inner system then diffuse outward and go through centrifugal instability interchange with the outer hot, tenuous plasma, observed as injection events in the region between 6 to $11\,\mathrm{R_S}$. The planet-ward transported hot electrons follow adiabatic heating and superimposed with the cold electron population, while the injected ions may interact with the dense neutral torus which produces energetic neutral atoms (ENAs).

The plasma models that we use for the ejection model is based on recent Cassini measurements. Results from Moncuquet *et al.* (2005), Persoon *et al.* (2006), and Schippers *et al.* (2008) are adopted for the plasma (thermal and superthermal) electrons. Models from Young *et al.* (2005), Kane *et al.* (2008), Tokar *et al.* (2008), Wilson *et al.* (2008, 2009), and Persoon *et al.* (2009) are adopted for the ion populations. Based on these works, an ad hoc axial–symmetry plasma model is built as input for the charging calculation. Magnetospheric protons (H^+) and water group ions (W^+) are assumed to have Maxwellian distribution while both electron components (cold and hot) are found to follow the kappa distribution (Schippers *et al.*, 2008). The density, the temperature, and the scale height (with respect to the equatorial plane) of ion and electron components along the L shell are plotted in figure 5.8. Also shown in the plot are the kappa indices for electron populations and the plasma ion flow speed (v_ϕ), which is adopted from Wilson *et al.* (2009) and Kane *et al.* (2008) and is used to evaluate the strength of the co–rotational electric field by $\mathbf{E}_c = -\mathbf{v}_\phi \times \mathbf{B}$.

In an environment with dense plasma such as planetary magnetosphere, where the ionization current induced by UV photons is not important, thermal electrons (energy $< 100\,\mathrm{eV}$) always dominate the grain charging due to their high mobility and therefore lead to a negative surface potential. This is the case for E ring particles inside of $\sim 7\,\mathrm{R_S}$. The equilibrium potential (the potential when the net current to the grain is zero) of water ice grain together with CDA charge measurements in Saturn's magnetosphere (Kempf *et al.*, 2006) are shown in figure 5.9. Contributions from various currents at equilibrium potential as function of distance to Saturn are shown in the lower panel of figure 5.9. As mentioned above, the electron current is the primary one throughout the magnetosphere. Inside 5 $\mathrm{R_S}$, the charge equilibrium is reached by the balance between the electron and (mainly) ion currents. As the electron temperature increases with distance to Saturn, outside of 5 $\mathrm{R_S}$ the secondary electron current takes over ion currents and becomes the major positive current that counterbalances the electron current. Outside $\sim 7\,\mathrm{R_S}$ the electron temperature is so high that dust grains loose more electrons than they collect and reach positive equilibrium potential.
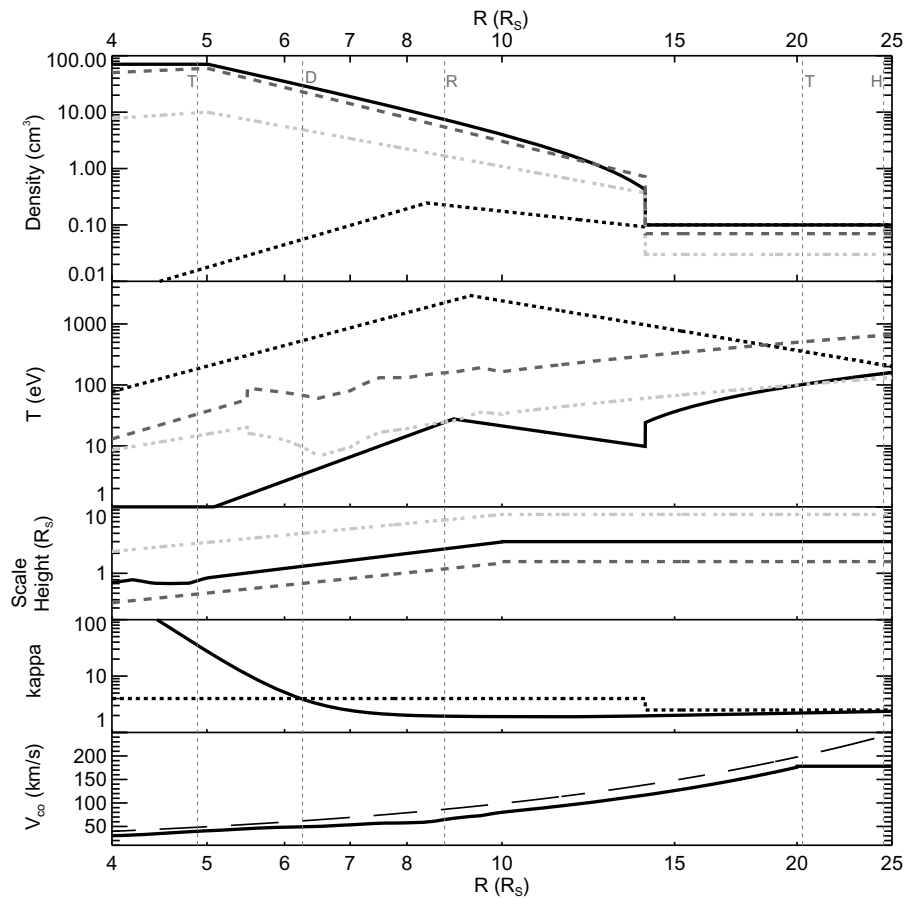
Figure 5.8: The plasma model used for the charging calculation in the ejection model. - From the top to the bottom, the panels are the plasma density, the temperature, the scale height, electron κ indexes, and the azimuthal plasma flow speed. Except for the plasma speed panel, the solid, dotted, dash, and dot–dash lines represent the properties of cold electrons, hot electrons, water group ions, and protons as function of L shell in the equatorial region. The hot electron population are assumed to distribute homogeneously regardless of the distance to the equator. In the bottom panel, the dash line marks the speed of full–corotation and the solid line represents the true plasma flow speed. Five vertical dotted lines mark the orbits of Saturnian moons: Tethys, Dione, Rhea, Titan, and Hyperion. The plasma model is based on Cassini measurements, for more detail please see references mentioned in the text.

Electrostatic equilibrium potential
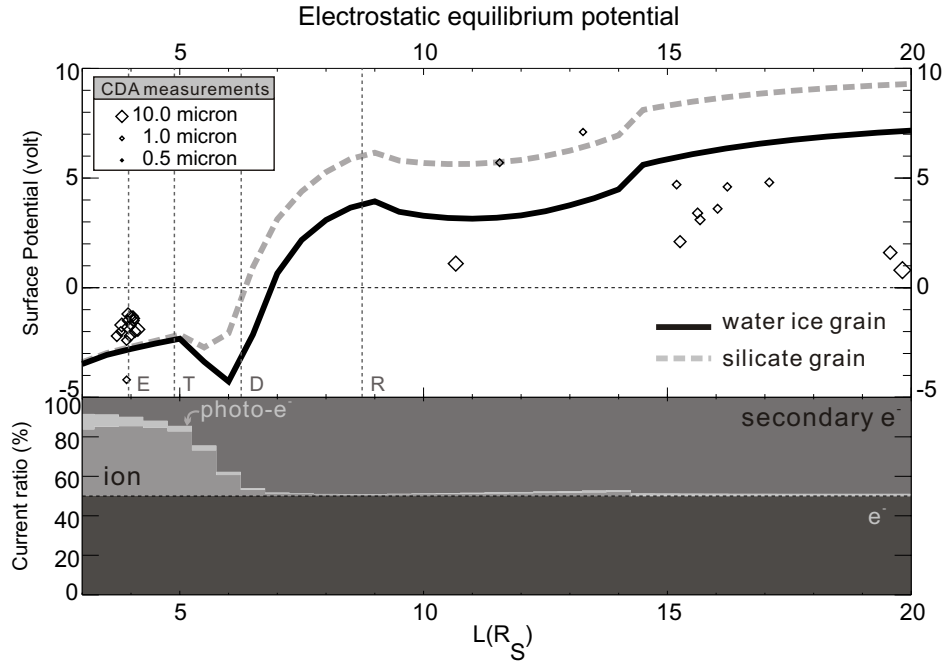
Figure 5.9: The equilibrium surface potential and current ration of water ice and silicate dust grains in Saturn's magnetosphere. - Upper panel: the equilibrium surface potential of water ice (solid) and silicate (dash) dust grains in Saturn's magnetosphere. Diamonds represents the size, the distance, and the grain charge measured by CDA (Beckmann, 2008; Kempf *et al.*, 2006). The only difference between icy and siliceous grains considered in the calculation is the secondary electron yield (5.1. Due to relatively weak secondary electron currents in the inner system (¡ 5 R_S), potential curves of these two grain types are similar. Bottom panel: the ratios between different currents for water ice grains at the equilibrium potential. The size of the area represents the current strength. Positive currents are located in upper half region.

In this work, we adopt the same equations as in Horányi (1996) and Kempf *et al.* (2006) to calculate the ion collection current (J_i) and the photo–electron current (J_ν). The non–isotropic plasma effect on J_i, caused by the relative velocity between dust particles and the plasma flow, is considered. However, the temperature anisotropy of plasma ions is ignored here. We simply assume that the ion distribution is isotropic and the ion temperature shown in figure 5.8 is calculated by $T_{ion} = (T_\parallel + 2T_\perp)/3$, with $T_\parallel$ and $T_\perp$ from aforementioned references. The two parameters related to J_ν: the photo–electric efficiency and the mean energy of the photo–electrons are set to be 0.1 and 2.5 eV respectively in our simulation.

As above-mentioned, the energy distributions of both cold and hot electron components in Saturn's magnetosphere are found to follow the kappa distribution (Schippers

5. SATURNIAN STREAM PARTICLES AS THE PROBE OF THE DUST-MAGNETOSPHERE INTERACTION

	δ_M	E_M (eV)	reference
SiO_2	3.9	430	(Kanaya *et al.*, 1978)
water ice	2.3	340	(Kempf *et al.*, 2006)

Table 5.1: The secondary electron emission parameters used in this work.

et al., 2008) and can be expressed as:

$$f_e(E) = n_e \left(\frac{m_e}{2\pi\kappa E_0} \right)^{3/2} \frac{\Gamma(\kappa+1)}{\Gamma(\kappa-\frac{1}{2})} \left(1 + \frac{E}{\kappa E_0} \right)^{-\kappa-1} , \tag{5.7}$$

where n_e is the density of electron, m_e is the electron mass, κ is the kappa index, $\Gamma(n) = (n-1)!$ is the Gamma function, and $E_0 = (2\kappa-3)T_e/2\kappa$.

Different from the Maxwellian distribution, the kappa distribution is characterized by an additional high–energy tail, which implies a non–equilibrium state. The kappa distribution reduces to the Maxwellian when $\kappa \to \infty$. Regarding the dust charging, due to the contribution from the high–energy tail, a kappa distribution plasma leads to higher collection flux than the Maxwellian case. Under the OML condition, the flux of electrons under kappa distribution collected onto a dust grain is written as (Chow *et al.*, 1993; Rosenberg & Mendis, 1992):

$$J_e = C_0 \times \begin{cases} \Gamma(\kappa-1) \cdot \left(1 - \frac{2e\phi}{(2\kappa-3)T_e} \right)^{1-\kappa}, & \text{if } \phi \leq 0 \\ \Gamma(\kappa) \cdot \left(\frac{\Gamma(\kappa-1)}{\Gamma(\kappa)} + \frac{2e\phi}{(2\kappa-3)T_e} \right), & \text{if } \phi \geq 0 \end{cases} , \tag{5.8}$$

where

$$C_0 = -en_e \left(\frac{kT_e}{4\pi m_e} \right)^{1/2} \frac{(2\kappa-3)^{1/2}}{\Gamma(\kappa-\frac{1}{2})} ,$$

$e = 1.602 \cdot 10^{-16}$ C is the elementary charge, and kT_e is the plasma electron temperature in eV.

When a dust grain collects an electron whose energy is high enough to excite other electrons on that dust grain to escape as secondary emission, a positive current called secondary electron current (J_{sec}) is produced:

$$J_{sec} = \frac{2\pi e}{m_e^2} \times \begin{cases} \int_0^\infty E\delta(E) f_e(E - e\phi) dE, & \text{if } \phi \leq 0 \\ exp(-e\phi/kT_{sec}) \cdot (1 + e\phi/kT_{sec}) \\ \quad \cdot \int_{e\phi}^\infty E\delta(E) f_e(E - e\phi) dE, & \text{if } \phi \geq 0 \end{cases} , \tag{5.9}$$

where kT_{sec} is the mean secondary electron energy. Laboratory studies found that the energy of secondary electrons follows the Maxwellian distribution with mean energy of

few eV. Here we set $kT_{sec} = 2.5\,\text{eV}$.

The $\delta(E)$ is the secondary electron yield and is a function of primary electron energies E. It can be expressed by an empirical universal yield curve with two material–dependent parameters: the maximum yield δ_M and the optimal energy E_M (in eV), i.e., the secondary yield curve reaches the maximum value δ_M at the incident energy of E_M. Here we adopt the expression for the secondary electron yield from Sternglass (1954):

$$\delta(E) = 7.4\,\delta_M\,(E/E_M)\cdot exp(-2(E/E_M)^{1/2})\,. \tag{5.10}$$

Adopting the Sternglass yield curve (Eq.5.10), Meyer-Vernet (1982) has derived the secondary electron current for a Maxwellian distributed plasma. As the yield increases with the energy of primary electrons, the excess high–energy tail of kappa distribution plasma consequently results in greater J_{sec}. As J_{sec} becomes more and more important toward the outer Saturnian magnetosphere, it ultimately determines the the neutral point of the E ring dust grain potential (figure 5.9). By substituting Eq.5.7 and Eq.5.10 into Eq.5.9, the secondary electron current under kappa distribution plasma can be written as:

$$J_{sec}^{\kappa} = C_1 \times \begin{cases} F(\kappa,\phi,E_M), & \text{if } \phi \leq 0 \\ exp(-e\phi/kT_{sec})\cdot(1+e\phi/kT_{sec}) \\ \quad\quad \cdot F(\kappa,\phi,E_M), & \text{if } \phi \geq 0 \end{cases}, \tag{5.11}$$

where

$$C_1 = 7.4\,\delta_M\,n_e\,e\cdot(2\pi m_e)^{-1/2}\cdot(\kappa E_0)^{-3/2}\cdot(\kappa+1)/(\kappa-1/2) \quad,$$

and

$$F(\kappa,\phi,E_M) = \int_{max(e\phi,0)}^{\infty} (E^2/E_M)\cdot exp(-2(E/E_M)^{1/2})$$
$$\cdot(1+(E-e\phi)/\kappa E_0)\,dE\,.$$

Using the κ indices profile (figure 5.8) and a given E_M value, the secondary electron current at different grain potential can be calculated by integrating Eq.5.12 numerically up to 10keV.

As mentioned earlier, the main component of most Saturnian stream particles probably is siliceous material (Kempf *et al.*, 2005b) though Saturn's ring system is dominated by water ice. We adopt the secondary emission characteristics of SiO_2 from (Kanaya *et al.*, 1978) in the ejection model. Furthermore, we also perform the same calculation with parameters of water ice grain as a comparison in order to understand the compositional discrepancy from the dynamics point of view. The δ_M and E_M are listed in table 5.1. Due to the fact that the secondary emission yield of SiO_2

is almost twice as the emission yield of water ice, the zero equilibrium potential point of silicate grains locates around Dione's orbit (6.26 R_S), inward of those of water ice grains (see figure 5.9). Nevertheless, the two curves lie within $-5\,V$ to $+10\,V$ among the magnetosphere.

The number of electric charges carried on a spheric grain is about $0.7 \cdot \phi \cdot s_{nm}$, where s_{nm} is the grain radius in nanometer. So a 5 nm grain with $\phi = -2\,V$ carries only 7 additional electrons on its surface. The small number of charges implies that the charging currents can not be approximated as continuous fluxes (as for μm–sized grains) but must be considered as discrete and quantized processes. Furthermore, by adding or removing one electron, the Lorentz force that this dust particle experiences will change $\sim 14\%$. Therefore, a more sophisticated method for stream–particle charging calculation is necessary.

To simulate the charging and dynamical evolution of a stream particle, we developed a procedure that treats the dust charging as a Poisson process. In this scenario, the aforementioned charging currents are considered as the expected number of charging events in a given time interval so that the probability of an event number can be calculated from the Poisson distribution. Moreover, the charging conditions vary throughout the magnetosphere, the expected event rate is not a constant but is a function of plasma and dust particle parameters (e.g. surface potential). To be more specific, this is actually an inhomogeneous Poisson process. Hence, the probability distribution of the number of events between t_1 and t_2 can be written as:

$$P(\lambda_{12}, k) = \frac{e^{-\lambda_{12}} \cdot \lambda_{12}^k}{k!}, \quad k = 0, 1, 2, \dots, \tag{5.12}$$

where k is the number of an event and λ_{12} is the expected number of charging events between t_1 and t_2. With the charging currents Eq.5.6, it can be expressed as:

$$\lambda_{12} = \int_{t_1}^{t_2} \lambda(t)dt = \int_{t_1}^{t_2} |J_e| + |J_i| + |J_\nu| + |J_{sec}| \, dt \,. \tag{5.13}$$

Then the type of charging event can be determined by the following probability distribution:

$$P(J_\alpha) = \int_{t_1}^{t_2} |J_\alpha|dt \,/\, \lambda_{12} \,, \tag{5.14}$$

where $\alpha = e$, i, ν, and sec. Eq.5.14 turns the various OML currents into a charging event type probability distribution. In other words, it determines whether a dust grain will obtain / loose an ion / electron for this charging event.

So there are two probabilities involved in this procedure: the first one describes the event number probability in one time step (the Eq.5.12). It is a function of k and λ_{12}. The second one is converted from OML currents and it reflects the relative importance of each current. In practice, the charging event during a given time interval can be

evaluated with Eq.5.12, Eq.5.14, and $n + 1$ random numbers. The first random number determines the amount of events (n) that happen during this time interval via Eq.5.12, while the other random numbers are used to decide the type of charging event based on the relative strength between aforementioned currents via Eq.5.14. Interestingly, we have developed this procedure independently but somehow reached a similar approach as Cui & Goree (1994).
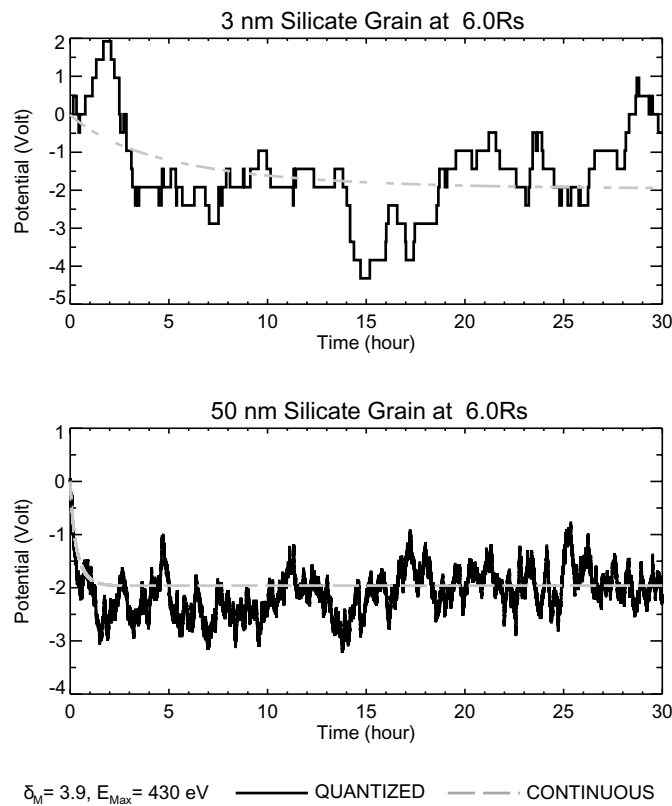
Figure 5.10: Comparison of stochastic charge variation on 3 and 50nm grains. - The potential calculated from continuous charging currents is marked by the gray dash line as a reference. One electric charge variation corresponds to $\sim 0.48\,V$ and $\sim 0.03\,V$ difference for 3 nm and 50 nm grain respectively.

As mentioned, the goal of the ejection model is to follow the dynamical and charging evolution of negatively charged nanodust grains. Since the grain is so tiny that it only carries small number of charges, each charging event could have determinant

influence on its evolution path. Therefore, in order to monitor each charge variation it is necessary to adopt small time steps in a way that in most cases not more than one charging event takes place during each time step, i.e., $P(\lambda_{12}, k > 1) \ll 1$. Moreover, even with one elementary charge variation, the potential of such a small grain changes largely, which consequently affects the current strength. Thus, our stochastic charging approximation is valid only with a small time step size.

As the event rate is proportional to the grain surface area, bigger grains then require smaller time steps to fulfill the condition. Compromising with the computation time, we set an upper limit of $\lambda_{12} \sim 0.4$, which means that in the worst case the probability to have more than one event in single time step is about 6.2% ($P(\lambda_{12} = 0.4, k = 0, 1) \simeq 67.0\%, 26.8\%$).

Figure 5.10 shows the comparison between continuous charging and stochastic charging curves for different sized silicate grains (3 nm and 50 nm) at 6 R_S in the ring plane. Their equilibrium potential at this distance is around -2 V. Though both grains start with zero charge, the charging histories of these two grains are quite different. For the 50 nm grain, the stochastic grain potential fluctuates between -1 V and -3 V, i.e., ± 1 V of the "expected" equilibrium potential. In contrast, for the 3 nm grain the deviation between two charging curves is large. Even though the equilibrium potential is negative, short excursions toward positive grain potential can still occur. As expected, the stochastic effect is more important for tiny grains due to the quantized nature of electric charge. Since the Lorentz force governs the dynamics of nanodust grains, the stochastic charge variation then acts as a strong diffusion mechanism on stream particles' dynamics and makes their dynamical evolution no longer determinative.

The motion of a charge particle under Saturn's gravity and the Lorentz force in cylindrical coordinates (r, Φ, z) can be described as:

$$\ddot{r} = \frac{Q_d}{m_d} \cdot B_z \cdot r \cdot (\dot{\Phi} - \Omega) - \frac{GM_S}{R^3} r + r\dot{\Phi}^2$$

$$\ddot{\Phi} = \frac{1}{r}\left[\frac{Q_d}{m_d} \cdot (\dot{z}B_r - \dot{r}B_z) - 2\dot{r}\dot{\Phi}\right] \qquad (5.15)$$

$$\ddot{z} = \frac{Q_d}{m_d} \cdot B_r \cdot r \cdot (\Omega - \dot{\Phi}) - \frac{GM_S}{R^3} z ,$$

where r is defined as the distance between the particle and Saturn's center of mass projected onto the ring plane, ϕ is the azimuthal angle, and z is the distance of the particle to the ring plane. We ignore the gravitational force (the J2 term) caused by the oblateness of Saturn and simply use a dipole magnetic field in our calculation. Test particles start with negative charges equivalent to ~ -1 V from slightly eccentric orbits between 5 to 6 R_S with maximum z of $\pm 1 R_S$ (corresponds to inclination of 10°). Their position vector and charge are traced until reaching one of the following scenarios: collision with the A ring, remaining in the E ring [1], or escaping from the magnetosphere

---

[1]Since our ejection model does not consider the reduction of the grain size due to sputtering, particles in the simulation may keep trapped in the E ring. In reality, grains trapped in E ring will eventually be sputtered.

$(r \geq 25\,R_S)$.

Figure 5.11 shows an example of the dynamical evolution path of a $3\,$nm SiO_2 particle. The particle starts with 2 electron charges from $5.5\,R_S$ with $\sim 3°$ inclination. It keeps charged negatively for 30 hours and then oscillates between different polarities a few times before the ejection. The velocity curve shows that during the first positive charge excursion, the grain immediately gets boosted (i.e., velocity increases with the distance) and its apocenter increases from 6 to $\sim 8\,R_S$, which puts the particle into the positive charging region (outside of $6.5\,R_S$, see figure 5.9). During the last orbit, the grain charges flip forth and back in a few hours and eventually become positive and ejected from the system. The final ejection speed of this particle is about $100\,$km s^{-1}. The "source region" of this ejection event calculated from Eq.5.5 is $9.8\,R_S$.

Figure 5.12 shows the distributions of charge–to–mass ratio (Q_d/m_d), ejection speed (v_{ex}), ejection time, the elevation angle of $3\,$nm SiO_2 stream particles. The simulated 'source region' is also shown to compare with the backward simulation results. For $3\,$nm grains, 98.5% of simulated grains are ejected but never collided with the A ring. Interestingly, there are even negatively charged particles ejected (2 out of $\sim 10,000$ ejected with one negative charge and 3 out of $\sim 10,000$ ejected with neutral potential). In this sense, the ejection of stream particles is similar to the energetic neutral atoms (ENAs) formation process.

The charge–to–mass ratio and ejection velocity distributions together with the joint contour are shown in figure 5.12a. Each bin of Q_d/m_d histogram (the upper panel) represent one electric charge difference. Most of $3\,$nm grains carry 9 ± 2 electric charges during ejection. The charge–to–mass ratio extends widely from $1,000$ to $10,000\,$C kg^{-1}, corresponding to 1 to 15 electric charges. However, the large difference in grain charge does not lead to a board ejection velocity distribution. About 90% of them reach ejection speed between 75 and $125\,$km s^{-1}. More important, the Q_d/m_d–v_{ex} contour fits to the backward simulation results (figure 5.7e) very well. Note that these two methods are entirely independent. The backward tracing results are derived from the observations in the interplanetary space, i.e., stream–particle–solar wind interaction, whereas the ejection model is based on the magnetospheric plasma measurements.

Furthermore, even though these grains start from 5 to $6\,R_S$, the simulated "source region" showed in figure 5.12b locates at the vicinity of Rhea's orbit, the same as the backward tracing result (figure 5.7h). In fact, the "source region" derived here actually reflects the combined dynamical effects from the plasma configuration of Saturn's magnetosphere, the grain properties, and the stochastic charging process. The consistence between results of two independent approaches provides confirmation for both methods and the dynamically–old stream particle scenario.
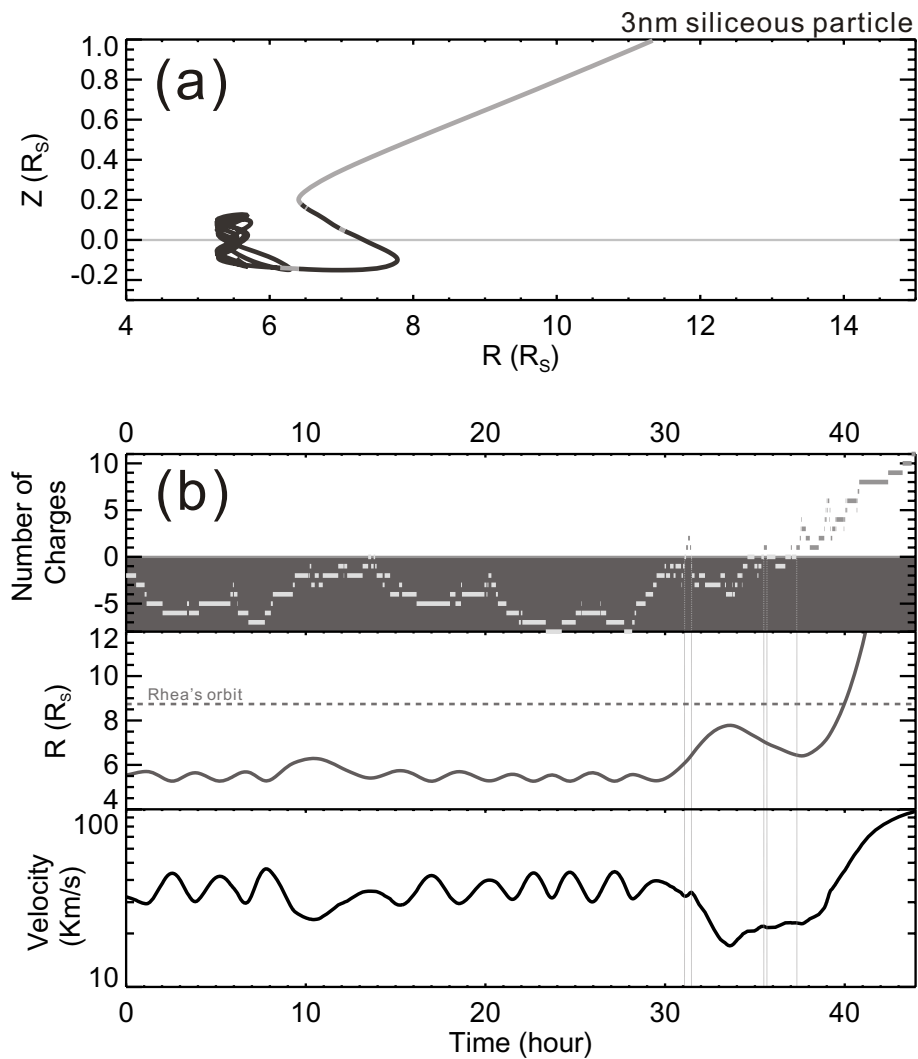
Figure 5.11: The evolution path of a 3 nm siliceous grain. - The particle starts from $5.5\,R_S$ and charged $\sim -1\,V$ with a slightly inclined ($\sim 3°$) and elliptic orbit. (a)The particle trajectory in the r–z plane. The electric polarity is shown by different colors: negative and neutral – black, positive – gray. The ring plane of Saturn is marked by the horizontal gray line. (b)The charges, the distance to the planet (center), and the velocity of this particle are plotted with respect to time. The periods when the particle charged positively are marked by vertical dotted lines. Notice the changes of particle velocity during the positive charge epochs.
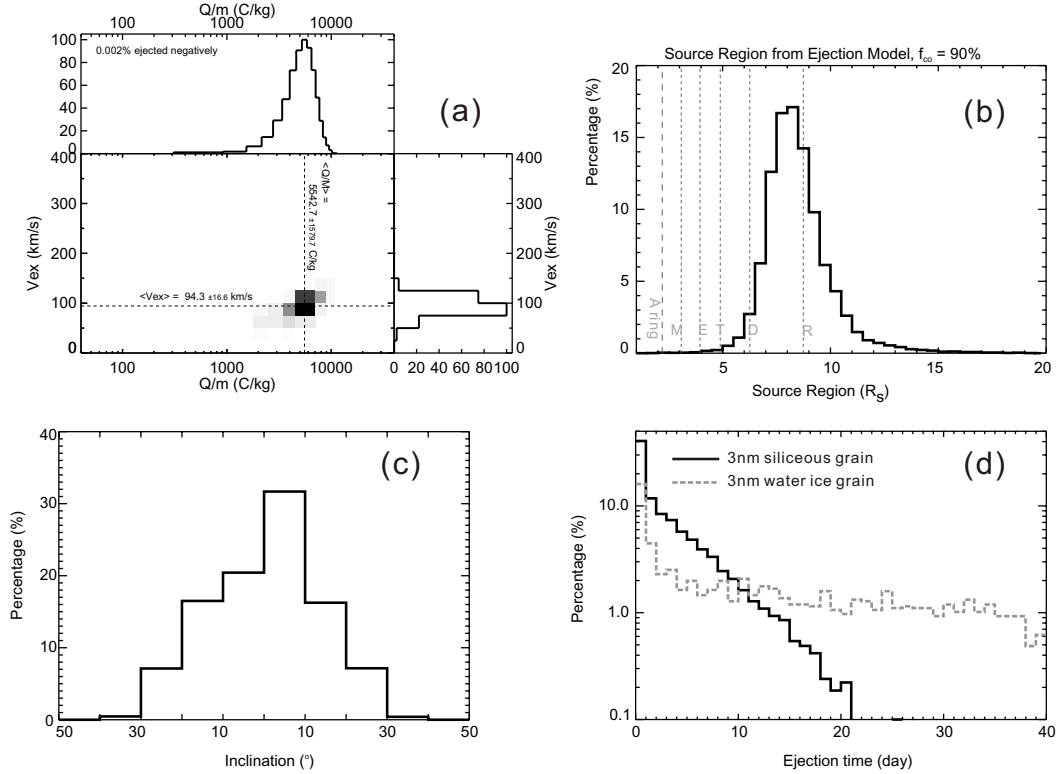
Figure 5.12: The statistics of dynamical properties from $\sim 10,000$ **simulated 3** nm **siliceous particles.** - (a)The charge–to–mass ratio–ejection velocity distributions. The binsize of charge–to–mass ratio histogram represents one electric charge difference. The grid used in the contour is the same as those in figure 5.7e. The most probable charge–to–mass ratio value, average ejection velocity, and their standard deviation are also given. (b)The source region calculated based on simulation results and Eq.5.5. (c)The distribution of the inclination of ejection velocity vector. (d)The ejection time of 3 nm particles with different compositions. It is clear that siliceous particles (black solid line) are ejected more efficiently than water ice ones (gray dash line). Note that there is no δ_M enhancement in this plot.

The inclination distribution (figure 5.12c) shows that most of the particles are ejected along the ring plane, which agrees with the CDA observations. Figure 5.12d shows the ejection time distributions of 3 nm particles with different compositions. About 80% of siliceous grains are ejected in first five days after the starting of simulation, in contrast the ejected percentage of icy grains in the same time scale is only 42%. The sputtering lifetime (τ_{sp}) extrapolated from Jurac *et al.* (2001) for icy 3 nm particles is about 55 days (assuming $\tau_{sp} = 50 \times (s_d/1000)$ years, s_d in unit of nm), τ_{sp} for siliceous grain may be ten times longer. Therefore, the shorter ejection time of nanoscale silicate parti-

cles implies that the ejection process is a more effective mechanism to remove these particles from the system, while half of icy grains are still bound in the magnetosphere after 20 days and are expected to be further sputtered down.

In figure 5.13a we plot the ejection model results on to the Q_d/m_d–v_{ex} contour obtained from backward simulations (figure 5.7e) in order to compare the dynamical properties between different grain materials. On top of that, Chow *et al.* (1993) had shown that the secondary electron yield of nanodust grains could be largely enhanced (i.e., by triple the δ_M for 5 nm grains). The stream–particle observations then provide an opportunity to examine their hypothesis. The secondary electron emission parameters of water ice and siliceous grains are listed in table 5.1. Accounting for the proposed yield enhancement due to their small sizes, we simply double the maximum yield by a factor of 2 regardless of the incident electron energy and grain sizes.

In general, the four parameter sets shown in figure 5.13a fit well with the "solution belt" from backward simulations. The Q_d/m_d and v_{ex} derived from different parameters are fitted by a power–law function $v_{ex} = \alpha \cdot (Q_d/m_d)^{\beta}$. The parameters α and β are listed in table 5.2. For particles with the same size, the lower density (i.e., the icy type) and the higher secondary electron yield lead to slightly larger ejection velocity and charge–to–mass ratio. Except that, there is no significant difference between results of four parameter sets. The maximal Q_d/m_d and v_{ex} derived are about 20,000 C kg^{-1} and 180 km s^{-1} (2 nm water ice grains with doubled δ_M). Since backward simulation results show a decreasing likelihood toward higher Q_d/m_d and v_{ex} (figure 5.7e, 5.7f, and 5.7g), we suggest that the size of detected Saturnian stream particles is $\gtrsim 2$ nm in radius.

Figure 5.13b shows the ratio between the ejection time (the median value) and the estimated sputtering lifetime as a function of particle radius. As the fate of nanodust particles in the E ring is determined by two competing processes – the ejection process and the plasma sputtering, the ratio between the time scales serves as an index of the relative importance of these two mechanisms and consequently the index of the particle destiny. If the ratio reaches unity (marked by the blue dash line), the sputtering effect dominates, otherwise these particles are likely to be ejected. The sputtering lifetime used here is only a rough estimation based on $\tau_{sp} = 50 \times (s_d(nm)/1000)$ and does not consider the different sputtering efficiency between these two materials. Moreover, we did not consider the reduction of grain sizes due to sputtering in our ejection model (i.e., grain sizes kept constant in the calculation), figure 5.13b should be seen as a relative rather than an absolute result.

In order to examine the possibility of the plume nanodust population (Jones *et al.*, 2009) as the source of stream particles, results of water ice particles starting between 4 and 5 R$_S$ with different secondary electron yield are also shown in figure 5.13b. It is clear that water ice grains, especially those with starting location closer to Enceladus'

	α	β
SiO_2, $\delta_M = 3.9$	1.34	0.50
SiO_2, $\delta_M = 7.8$	1.59	0.49
H_2O, $\delta_M = 2.3$	0.52	0.60
H_2O, $\delta_M = 4.6$	1.65	0.48

Table 5.2: The Q_d/m_d and v_{ex} derived from the ejection model for different grain parameters are fitted by a power–law, $v_{ex} = \alpha \cdot (Q_d/m_d)^\beta$.

orbit with normal δ_M, are governed by the plasma sputtering rather than being ejected as stream particles. On top of that, tinier water ice particles seem more dominated by sputtering. Therefore, qualitatively speaking, the erosion of the nanoscale ice particles in the E ring behaves like a run–away process – the smaller the grain is, the less probable they are to be ejected. For SiO_2 grains or water ice grains with enhanced δ_M, the result is not sensitive to the grain size.

5.4   Stream Particle Composition

The main goal of the compositional analysis presented in this chapter is to investigate compositional similarities between stream particles and E ring grains, which predominantly consist of water ice. The identification of particle ions of Saturnian stream particle impacts is a challenging task. Because of the tininess of the grains which hit the instrument at extreme velocities, the impact produces much more ions from target material and contaminants (Rh^+, C^+, H^+) than from the dust particle (figure 5.2). The ion signal from the particle itself often is barely above the noise level or not present at all (Postberg *et al.*, 2009a). However, with the larger fraction of stream particles, which create an ion yield of at least 2 - 3 fC, a semi-quantitative chemical characterization can be attempted, but even here particles mass lines are often to weak to be detectable.

At low and intermediate impact speeds (1 to 12 $km\,s^{-1}$), as applicable for many E ring particle detections, the characterising cations for water in CDA spectra is the hydronium ion (H_3O^+) and its cluster with neutral water molecules $+(H_3O^+)$-$(H_2O^+)n$ (Hillier *et al.*, 2007). Kempf *et al.* (2005b) also used the hydronium ion as the tracer–ion for water ice in stream particles. However, the highly inclined E ring crossings carried out by Cassini in 2007 and 2008 provided spectra from higher impact velocities. They showed that at speeds of ~ 14 to 18 $km\,s^{-1}$ also H_2O^+, OH^+, O^+, O_2^+, H^+, H_2^+, and H_3^+ are formed in greater abundance. Extrapolating from this behaviour for the regime of stream particles (50 to 200 $km\,s^{-1}$) it is plausible that water molecules are mostly disintegrated into O^+ and H^+. Both ions form mass lines in stream particle spectra
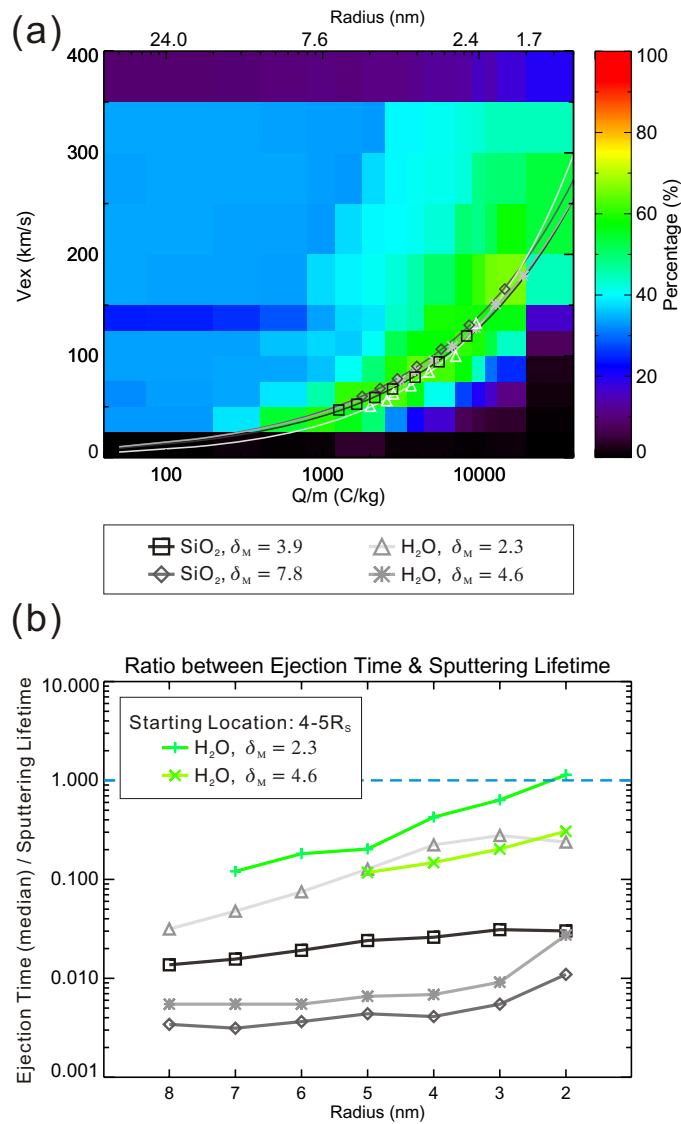
Figure 5.13: Comparison of backward simulation and ejection model result. - (a)Comparison of backward simulation (background contour) and ejection model (gray scale symbols and lines) results. Four different parameter sets are used in the ejection model to calculate the dynamical properties of Saturnian stream particles. The ejection velocities as function of the charge–to–mass ratio are plotted on top of the figure 5.7e. The best fits of these simulation sets are also plotted and listed in table 5.2. Particles with radius between 2 and 8 nm from four parameter sets all fit with the backward simulation results. Though particles with enhanced δ_M do have higher charge–to–mass ratio and ejection velocity. (b)The ratio between the ejection time (the median value) and the estimated sputtering lifetime as function of particle radius. This chart should not be seen in a absolute scale but as a relative variation between different parameter sets. In general, particles with smaller secondary electron yield are more difficult to eject from the inner system. See text for more detail.

		H_3^+	C^+	Rh^+	O^+	Si^+	Na^+
Occurrence:	Sat. pre-SOI	42 %	99 %	99%	77%	67%	11%
	Sat. Orbit A	59 %	99 %	92%	58%	36%	12%
	Jupiter	64 %	100%	98%	78%	20%	91%
Amplitude:	Sat. pre-SOI	1	1	1	1	1	1
	Sat. Orbit A	1.1	0.6	0.7	1.1	0.7	2.7
	Jupiter	0.7	1.1	2.0	1.1	0.5	12.0

Table 5.3: Frequency (occurrence) of mass lines and their average intensities (amplitude) in the respective data sets. Note that since the average ion yields of Jovian stream particles are higher, the amplitudes of the mass lines are normalised with respect to the ion yields.

	Number	Period (Day, Year)	Distance	Avg. ion yield
Sat. pre-SOI	66 (68)	120 - 165, 2004	160 - 550 R_S	3,5 fC
Sat. Orbit A	142(963)	181 - 300, 2004	25 - 150 R_S	2,8 fC
Jupiter	86 (222)	248 - 251, 2000	1490 - 1520 R_J	7,5 fC

Table 5.4: Properties of the spectra sets used in table 5.3. The first row is the number of spectra with ion yields between 2 - 10 fC used for the comparison in Table 5.3. The number in brackets is the total spectrum number recorded in that period (regardless of the ion yield).

(Kempf *et al.*, 2005b). However, H^+ is known to be produced from contamination of the CDA impact target at high impact speeds. This might also be the case for O^+, albeit only to a lesser extend (Postberg *et al.*, 2009a).

For this work it is attempted to estimate the water content in Saturnian stream particles by comparing the amplitudes of the O^+ mass line with those in spectra produced by Jovian stream particles, which are supposed to contain no water ice but sodium chloride as their bulk component (Postberg *et al.*, 2006). Because of their similar speed and size the latter are well suited for such a comparison. Although Jovian stream particle spectra frequently show an O^+ mass line it stems (too unknown extends) either from a minor siliceous compound in the grains or CDA contamination (Postberg *et al.*, 2006). Thus, if water is a bulk component of Saturnian stream particles, the fraction of released O^+ ions should be systematically higher than in the Jovian case.

Jovian stream particles are on average a bit faster (200 - 300 $\mathrm{km\,s^{-1}}$) and larger (5 - 20 nm) than in the Saturnian case. Therefore they produce a distribution with higher average ion yield on impact. However, the ion yields of both dust population have an overlap between 2 and 10 fC, this fraction of the populations is used for the comparison in table 5.3. In the Jovian case the spectra not considered in table 5.3 have ion yields above, in the Saturnian case mostly below the overlapping range. The table shows

the average mass line amplitudes of certain ion species and how frequently they are detected in Jovian and Saturnian stream particle spectra. Two Saturnian stream particle subsets are used. One set recorded in Cassini's approach phase before orbit insertion ('pre–SOI'), the other during Cassini's first Orbit ('Orbit A'). The properties of the different sets of spectra are summarized in table 5.4.

The first three ion species (H_3^+, C^+, Rh^+) shown in table 5.3 are ions stemming from the instrument target. Their yield is indicative for dynamical properties. The other species shown (O^+, Si^+, Na^+) are possible particle constituents. The higher abundance of C^+ and Rh^+ in Jovian stream particle spectra proves their higher impact energies. Since higher impact energies are unfavorable for the formation of hydrogen cluster-ions H_3^+ its reduced yield points at higher energy densities, too. Interestingly, the two Saturnian subsets also exhibit a significant difference in their abundance of target species. Before SOI, far from Saturn, the abundance of C^+, Rh^+ is increased, whereas H_3^+ is decreased relative to Orbit A which was recorded closer to Saturn. Since there is no reason to assume a size difference, the particles recorded further away from Saturn must have impacted with higher speed. This finding is supported by the higher average total ion yield of the respective data set.

The average contribution of O^+ ions is similar for the Jovian and Saturnian stream particles. This finding is indicative for water ice not being a main constituent of Saturnian stream particles in general. However, about 5% of the spectra are outliers with a significantly increased abundance of O^+ ions (figure 5.14a) - a phenomenon which cannot be observed in the Jovian case. This finding strongly indicates an occasional dominance of water ice. In most cases however there is no indication for water ice as the bulk component of the particles as observed in the E ring. A varying minor water ice constituent of not more than about 50% (maybe far less) is in agreement with most spectra.

The main difference between the stream particles spectra sets is the higher abundance and occurrence of Na^+ at Jupiter and of Si^+ at Saturn. Na^+ at Jupiter stems from the particles bulk component NaCl. At Saturn the faint sodium mass lines are in most cases in agreement with a low level target contamination (Postberg *et al.*, 2009a). This is of particular relevance since alkali ions play a major role in spectra of E ring grains (Postberg *et al.,* 2009b) which are to a greater part produced by the active venting of the moon Enceladus. About 6% of E ring ice grains contain sodium salts on a percent level and due to its low ionization energy Na^+ is the most abundant ion in these spectra. The strong depletion of alkali compounds in Saturnian stream particles coincides with the depletion of water ice. However, there is an indication of increasing Na^+ abundance in Orbit A (table 5.3) which points at sodium salts as an occasional particle compound closer to Saturn. This phenomenon will be investigated in future work.
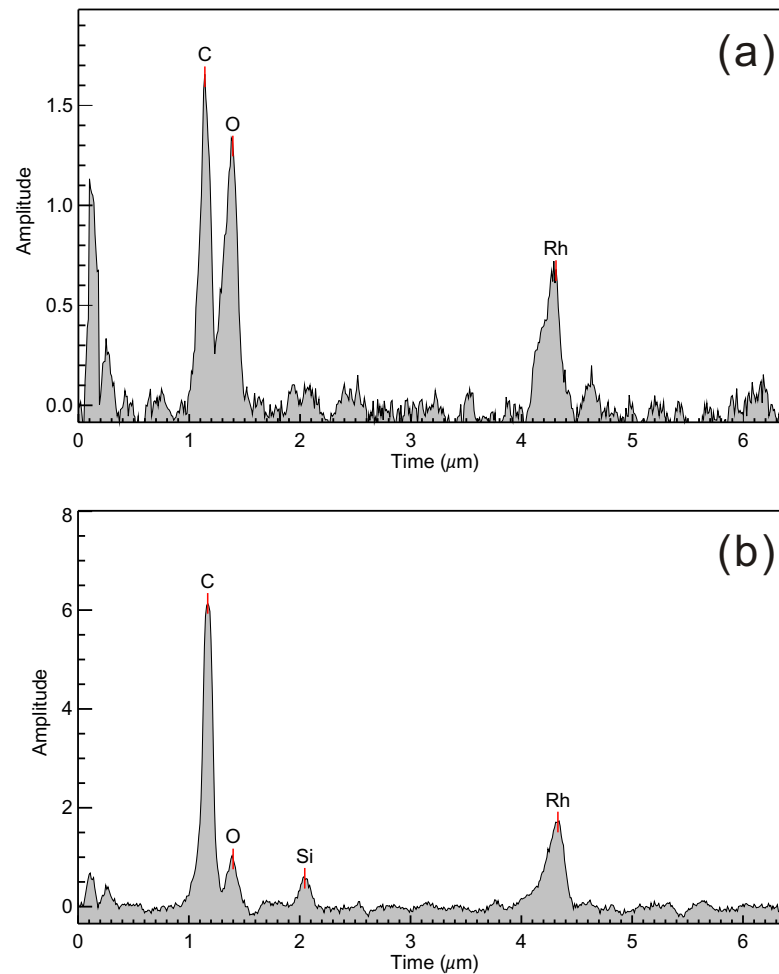
Figure 5.14: Examples of Saturnian stream–particle spectra. - (a) Example of a particularly oxygen rich spectrum. These rare cases likely mark an impact of a stream particle with abundant water ice. Mass lines from carbon (C^+) and rhodium (Rh^+) stem from the instruments target. Since the spectrum shows no silicon mass line it is in best agreement with a pure water ice grain. (b) Spectrum of an impact from a relatively large Saturnian stream particle (Ion yield = 6 fC) with unusually distinct particle mass lines and typical composition. Since there is no access of oxygen, the spectrum is indicative of a silicate particle with few or no water ice. The absence of metal mass lines points at silica as the main constituent.

Jovian and Saturnian spectra frequently show Si^+. Although the Jovian particles in the sample are likely larger than the Saturnian ones Si^+ mass lines have a lower frequency and average intensity and than at Saturn (table 5.3). Thus, the main finding of Si^+ as the only reliably identified particle compound (Kempf *et al.*, 2005b) is confirmed for most cases (Figure 5.14b). Often the ratio of Si^+ to O^+ is in good agreement with silicates as a main particle constituent. With the abundant C^+ signature silicon carbide is also possible but implausible from a cosmochemical point of view. Moreover, C^+ is an abundant target contaminant and the mass line therefore might stem solely from contamination (Postberg *et al.*, 2009a). The rare and faint Fe^+ mass lines (Kempf *et al.*, 2005b) and the almost complete absence of Mg^+ or any other non alkali mass line are remarkable. Because of their lower ionization energy the metal component would yield a higher cation signal than silicon if typical rock forming minerals (like olivine or pyroxene) are the main silicon bearing compounds. In contrast the silicon mass line is by far more abundant than any possible metal mass line. The siliceous component of Saturnian stream particles is thus likely heavily depleted in metals and stream particles are probably composed of silica (SiO_2) with only a small fraction of metal bearing minerals.
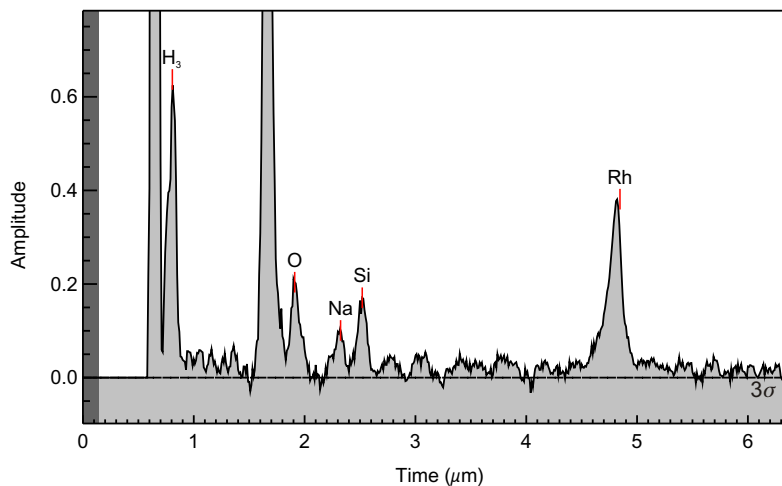
Figure 5.15: Co-added spectrum of the 923 individual ultra-faint spectra - with ion yields below $2\,fC$ which have not been considered for the individual analysis shown in table 5.3. Although the possible particle mass lines (O^+, Si^+, Na^+) are too weak for a definite identification in most of these individual spectra, they form distinct signatures when co-added.

Again it has to pointed out that the results discussed here refer to the 20% fraction of larger stream particles shown in table 5.3 which ion yields above $2\,fC$ are considered suitable for an individual compositional characterisation. Even in this subset the probable particle compounds show up only in a fraction of spectra. 80% of the registered stream particles show ion yields below $2\,fC$ and are in most cases to small to produce significant particle mass lines at all. Thus in principle the compositional results discussed here are only valid for a small proportion of particles. However, if these ultra-weak spectral signals are co-added, they show the same characteristic particle mass lines as the larger impacts (Figure 5.15). The similar proportion of mass line intensities indicates, that the fraction of larger particles used for table 5.3 is likely representative for the whole ensemble.

Organic compounds are also suspected to be a minor constituent of E ring grains (Postberg *et al.*, 2008). In the impact speed regime of stream particles Hydrocarbons likely decompose almost completely into H^+ and C^+ (Srama et al., 2009). Since these ions also form large mass lines from CDA target contamination (Postberg *et al.*, 2009a) no conclusions on a contribution of organic compounds in Saturnian stream particles can be drawn.

Kempf *et al.* (2005b), also suggest that nitrogen bearing compounds might play a role for the composition of stream particles because of occasional signatures at 14 (N^+) and 18 amu (NH_4^+). Here we suggest that H_2O^+ is responsible for the rare and faint 18 amu mass lines rather than NH_4^+. However, the mass line at 14 amu is in agreement with (albeit not proof for) an occasional contribution of a nitrogen bearing compound.

5.5   Discussion

The compositional discrepancy between stream particles and icy Saturnian rings is an intriguing finding. We also notice that, besides the secondary electron emission yield as mentioned before, the sputtering efficiencies of siliceous and icy materials are quite different. Studies have shown that the sputtering rate of water ice is about an order of magnitude higher than those of silicate (Guillet *et al.*, 2009; Tielens *et al.*, 1994). In the dense part of the E ring (4 to $5\,R_S$) where the ion temperature as well as the plasma flow speed are low, this difference can even reach a factor of 100 (i.e., the ratio shown in figure 5.13b for SiO_2 cases will be 100 times lower). Presuming that a certain number of E ring grains contain tiny amount of siliceous material, after ejected from Enceladus' plumes into the E ring, the icy material is constantly eroded by plasma sputtering whereas the embedded siliceous cores keep intact. When the surrounding icy structure is damaged to certain extend, nanometer–sized siliceous "raisins" are released from the water ice matrix and start their own dynamical evolutions as described by our ejection model.

The remaining part of the water ice grain then continues to drift outward via the plasma drag. In the middle to outer magnetosphere, the sputtering rate becomes much weaker and therefore the grain size decreases more slowly. Hence, the stream–particle production rate is reduced even the equilibrium potential is positive. Considering the reduction of grain sizes from plasma sputtering, studies of long–term dynamical evolution of E ring particles show that micron–sized grains which originate from Enceladus can migrate through the intense sputtering region and end up as sub–micron grains in orbits around 10 to $20 \, R_S$ (Beckmann, 2008; Horányi *et al.*, 2008). These particles may keep drifting outward either by plasma drag and / or gaining energy from $\mathbf{E}_c$ and ultimately leave the magnetosphere as small (but bigger than stream particles, say few 10s of nm) and relatively slow (10 to $20 \, \mathrm{km \, s^{-1}}$) populations. Most of the smaller, sub–micron sized particles emanated from Enceladus' plume may not survive to the outer magnetosphere but are sputtered down to stream–particle size range at the "source region". Due to the difference in sputtering yield, siliceous compounds remain as dominant constituent in these grains. Therefore, even though Saturn's magnetosphere is dominated by water ice material, the ice–to–silicon ratio of stream particles is largely reduced, which agrees with the mass spectra analysis.

Few percent of stream–particle mass spectra are found to have a dominant water ice content. The source of these particles could be E ring under aforementioned sputtering–diffusion process, the nanodust population in Enceladus' plumes (Jones *et al.*, 2009), or the main rings of Saturn locate inside $2.26 \, R_S$. The particle density of the dense rings is so high that the plasma is extremely depleted due to grain absorption. Therefore the grain charging in this region is dominated by the photo–electron emission which leads to a positive grain potential. Theoretically, particles outside of the synchronous orbit ($1.86 \, R_S$) with positive potentials would have a chance to be transported outward via the stochastic charging process and finally be ejected as stream particles. Our results do not exclude the idea that the A ring and the nanodust population from Enceladus' plumes being possible stream–particle sources. However, nanoscale dust grains from these two probable sources are presumed to be composed of water ice, which suffers from the sputtering, and are less preferential to be ejected as indicated from figure 5.13b. [1] Hence, based on the dynamical/compositional features derived from CDA measurements, we consider that the tenuous E ring as the main source of Saturnian stream particles. The sputtering process not only determines E ring grains' lifetime but also sets up a material selection mechanism for stream particles.

As proposed by (Chow *et al.*, 1993), the enhancement of the secondary electron yield does have influence on our simulation results. First, particles with higher δ_M

---

[1]As stated before and reiterated here, our calculation does not consider the erosion of grain sizes from the plasma sputtering simultaneously with the dynamical evolution, i.e., the particle size keeps constant in each simulation.

are ejected with higher Q_d/m_d and v_{ex}. Second, higher δ_M particles are ejected more easily than normal ones. From the dynamical point of view, the polarity flip of a dust grain potential must be located near the "source region" derived from backward tracing simulations (figure 5.7h). For grains with larger secondary electron yield, the potential turning point shifts planetward and results in "source region" distance $\ll 8\,R_S$. Therefore, our results agree with the moderate enhancement of secondary electron emission yield for tiny dust grains (e.g., ~ 2 or 3 times of the laboratory flat target, regardless of the incident electron energy and grain sizes).

For micron–sized dust grains, it is the plasma environment that determines the charging conditions and consequently regulates the dust grain dynamics. However, this is less strict for nanometer–sized particles because of the stochastic charge variation. As shown before, even in a negative charging environment, siliceous nanodust grains can temporarily reach positive surface potential and initiates the outward orbital evolution. Spahn *et al.* (2003) have shown that the perturbation from fluctuating planetary magnetic field is capable to produce dispersions on orbital inclinations and eccentricities for micron–sized grains. The authors also claimed that the stochastic variations might even dominate the dynamics of tiny dust grains. In our study, the stochastic charging variation acts as a diffusion mechanism and, as predicted, eventually governs the dynamical evolution of nanometer sized dust grains.

The existence of Saturnian stream particles together with their composition confirms the idea that the plasma sputtering dominates the mass loss of E ring dust grains, as proposed by Jurac *et al.* (2001) and Johnson *et al.* (2008). After being ejected from Enceladus' plumes, E ring particles behave as mass–transporting vehicles that redistribute Enceladus' material to the whole magnetosphere. Considering plasma–surface interactions, H_2O molecules are the main product of ion sputtering and O_2 can also be generated by thermal electrons (energy $< 100\,\mathrm{eV}$, (Sieger *et al.*, 1998)) from E ring grains. Following the ionization and dissociation processes, these neutral molecules then are transformed into other spices (OH and O) or ions (H_2O^+, OH^+, O^+, H^+, O_2^+, ...etc). Therefore, the mobile E ring grains serve as local sources that provide neutral and plasma in the middle–to–outer magnetosphere.

Recently reported atomic oxygen emission observed by the Cassini UVIS suggested that about 40% of total atomic oxygen is located outside of $10\,R_S$ (Melin *et al.*, 2009). Due to the low electron ionization and photo–ionization rates, the lifetime of atomic oxygen is very long (~ 1 year, (Melin *et al.*, 2009, Table 4)), which implies a slow source rate. Since the E ring extends outward until Titan's orbit, it is likely that the dissociated products from the sputtered E ring grain material is sufficient to maintain the observed oxygen UV emission.

Based on Cassini CAPS measurements, the analysis by Martens *et al.* (2008) showed that the abundance ratio between O_2^+ and water group ions is about 0.3%

inside $8 R_S$ and increases significantly between 8 to $10 R_S$ with a dip around Rhea's orbit. Since O_2^+ ions are most likely formed from O_2 and the oxygen molecules can not be produced from H_2O in gas phase. Probable sources of O_2 are E ring particles, Rhea and its ring as proposed by Martens *et al.* (2008), and the main rings. Based on simulations by Tseng *et al.* (2009), the amount of O_2 transported from the main ring to Rhea's vicinity is about an order of magnitude lower than the observed density [1], the observed O_2^+ is probably caused by the local source. Considering the surface area of Rhea is much larger than the surface of E ring grains, Martens *et al.* (2008) suggested that O_2 molecules produced from the surface of Rhea and its ring are the source of observed O_2^+.

However, as the reason of O_2 being the main constituent of Europa and Ganymade's tenuous atmosphere, only a fraction of O_2 molecules produced on the surface can escape from Rhea's gravity and enter the magnetosphere. In contrast, O_2 produced from the E ring grain surface are released freely. Furthermore, outside the dense Enceladus neutral torus, the electron temperature rises with increasing distance and reaches the O_2 production threshold of $10 \pm 2\,\mathrm{eV}$ (Orlando & Sieger, 2003) at around $7 R_S$ and coincides with the rising O_2^+/W^+ feature. Therefore, we suggest that the O_2 produced from the electron–E ring particle interaction may also contribute as a local extended source, which can be estimated based on plasma electron and dust measurements. To calculate the E ring contribution to the magnetospheric neutral / plasma is beyond the scope of this paper. Nevertheless, it is clearly necessary to adopt in–situ E ring measurements and/or dynamical simulations into sputtering calculations to understand the sources and sinks of plasma and neutrals in Saturn's magnetosphere.

5.6 Summary

In this work we have analyzed the CDA Saturnian stream–particle measurements in interplanetary space during 2004 and the beginning of 2005. Compared to the pre–SOI measurements, the different observation geometry changed the stream particle impact detection pattern from IMF–sector dependent to quiescence–burst alteration. Since these particles are outside the instrument's calibration range, we performed backward tracing simulations with the solar wind and dust measurements from the Cassini spacecraft to give constraints on their dynamical properties. We found that their ejection velocities ranges from 50 to $200\,\mathrm{km\,s^{-1}}$ and the charge–to–mass ratio range from $1,000$ to $20,000\,\mathrm{C\,kg^{-1}}$, which corresponds to a radius of 2 to $8\,\mathrm{nm}$ assuming $+5\,\mathrm{V}$ potential and density of $2,300\ \mathrm{kg\,m^{-3}}$.

---

[1]Future Cassini O_2^+ measurements during Saturn's equinox may help to distinguish the relative contribution between the main ring source and the local source (E ring + Rhea), as predicted by Tseng *et al.* (2009) the magnetospheric O_2^+ will then be nearly depleted assuming the ring's O_2 atmosphere is produced by photolysis.

Moreover, the backward tracing results also indicate that the "source region" of stream particles is predominately located between Dione and Rhea's orbits. Adopting the dynamically–old grain scenario [Kempf et al., manuscript in preparation], the stochastic charging, and the plasma model based on Cassini observations, our ejection model nicely reproduced the backward tracing results. In contrast to E ring grains which consist predominately of water ice, stream particles have a drastically enhanced siliceous component. Combining with the long–term E ring evolution simulations, we suggest that the discrepancy between stream–particle composition and the icy Saturnian system is mainly caused by the difference in sputtering rate of water ice and siliceous material. The existence of a water ice component (indicated by oxygen and sodium lines) in Saturnian stream particle spectra is also in agreement with the dynamically–old grain scenario.

In general, this work has three implications: First, the stochastic charge variation provides nanometer sized particles a diffusion mechanism, which weakens the dominance of charging environment, and eventually governs their dynamical evolution and results in the ejection of Saturnian stream particles.

Second, based on observation and backward simulation results, we also compare in our ejection model the influence of secondary electron yield enhancement due to tiny grain sizes. Our simulations show that by increasing the yield by a factor of two, the modeled stream–particle properties still fit to the backward tracing results.

The dominance of siliceous component in most stream particles proves the idea of sputtering being the major mass loss mechanism of icy E ring dust grains. Due to the large extension of the E ring, the neutrals and ions contributed from E ring particles via plasma–icy surface processes are influential to the magnetospheric environment (e.g., the O_2^+/W^+ ratio around Rhea's orbit and the large extension of oxygen molecule indicated by UV emission observations) and need to be considered in order to understand the mass budget and the dust–neutral–plasma interactions in Saturn's magnetosphere.

5. SATURNIAN STREAM PARTICLES AS THE PROBE OF THE DUST-MAGNETOSPHERE INTERACTION

References

BAGUHL, M., GRÜN, E., LINKERT, G., LINKERT, D. & SIDDIQUE, N. (1993). Identification of small dust impacts in the ULYSSES dust detector data. *Planetary and Space Science*, **41**, 1085–1098. 4, 48

BECKMANN, U. (2008). *Dynamik von Sataubteichen in Saturns E–Ring*. Ph.D. thesis, University Heidelberg. 8, 76, 99, 116

CHOW, V., MENDIS, D. & ROSENBERG, M. (1993). Role of grain size and particle velocity distribution in secondary electron emission in space plasmas. *J. Geophys. Res.B*, **98**, 19 065–19 076. 100, 108, 116

CUI, C. & GOREE, J. (1994). Fluctuations of the charge on a dust grain in a plasma. *IEEE Transactions on Plasma Science*, **22**, 151–158. 103

DELAMERE, P.A., STEFFL, A. & BAGENAL, F. (2004). Modeling temporal variability of plasma conditions in the Io torus during the Cassini era. *Journal of Geophysical Research (Space Physics)*, **109**, 10216. 30, 32, 78

FLANDES, A. & KRÜGER, H. (2007). Solar Wind Modulation of Jupiter Dust Stream Detection. *Dust in Planetary Systems*, **643**, 87–90. 48, 62, 64, 86

GAZIS, P.R., MCDONALD, F.B., BURGER, R.A., CHALOV, S., DECKER, R.B., DWYER, J., INTRILIGATOR, D.S., JOKIPII, J.R., LAZARUS, A.J., MASON, G.M., PIZZO, V.J., POTGIETER, M.S., RICHARDSON, I.G. & LANZEROTTI, L.J. (1999). Corotating Interaction Regions in the Outer Heliosphere. *Space Science Reviews*, **89**, 269–305. 90

GOERTZ, C.K. & IP, W. (1984). Limitation of electrostatic charging of dust particles in a plasma. *Geophys. Res. Lett.*, **11**, 349–352. 96

GRAPS, A., GRÜN, E., SVEDHEM, H., KRÜGER, H., HORÁNYI, M., HECK, A. & LAMMERS, S. (2000). Io as a source of the jovian dust streams. *Nature*, **405**, 48–50. 6, 7, 68, 77

GRÜN, E., FECHTIG, H., HANNER, M.S., KISSEL, J., LINDBLAD, B.A., LINKERT, D., MAAS, D., MORFILL, G.E. & ZOOK, H.A. (1992a). The Galileo Dust Detector. *Space Science Reviews*, **60**, 317–340. 51

REFERENCES

GRÜN, E., FECHTIG, H., KISSEL, J., LINKERT, D., MAAS, D., MCDONNELL, J.A.M., MORFILL, G.E., SCHWEHM, G., ZOOK, H.A. & GIESE, R.H. (1992b). The Ulyssses dust experiment. *Astron. Astrophys. Supl.*, **92**, 411–423. 51

GRÜN, E., ZOOK, H.A., BAGUHL, M., FECHTIG, H., HANNER, M.S., KISSEL, J., LINDBLAD, B.A., LINKERT, D., LINKERT, G. & MANN, I.B. (1992c). ULYSSES dust measurements near Jupiter. *Science*, **257**, 1550–1552. 48

GRÜN, E., ZOOK, H., BAGUHL, M., BALOGH, A., BAME, S., FECHTIG, H., FORSYTH, R., HANNER, M., HORANYI, M., KISSEL, J., LINDBLAD, B.A., LINKERT, D., LINKERT, G., MANN, I., MCDONNEL, J., MORFILL, G., PHILLIPS, J., POLANSKEY, C., SCHWEHM, G., SIDDIQUE, N., STAUBACH, P., SVESTKA, J. & TAYLOR, A. (1993). Discovery of Jovian dust streams and interstellar grains by the Ulysses spacecraft. *Nature*, **362**, 428–430. 4, 5, 15, 47, 48, 63, 64, 67, 77

GRÜN, E., BAGUHL, M., HAMILTON, D., RIEMANN, R., ZOOK, H., DERMOTT, S., FECHTIG, H., GUSTAFSON, B., HANNER, M., HORÁNYI, M., KHURANA, K., KISSEL, J., KIVELSON, M., LINDBLAD, B.A., LINKERT, D., LINKERT, G., MANN, I., MCDONNEL, J., MORFILL, G., POLANSKEY, C., SCHWEHM, G. & SRAMA, R. (1996). Constraints from galileo observations on the origin of jovian dust streams. *Nature*, **381**, 395–398. 15, 48, 63

GRÜN, E., KRÜGER, H., GRAPS, A., HAMILTON, D., HECK, A., LINKERT, G., DERMOTT, S., FECHTIG, H., GUSTAFSON, B., HANNER, M., HORÁNYI, M., KISSEL, J., LINDBLAD, B., LINKERT, D., MANN, I., MCDONNEL, J., MORFILL, G., POLANSKEY, C., SCHWEHM, G. & SRAMA, R. (1998). Galileo observes electromagnetically coupled dust in the jovian magnetosphere. *J. Geophys. Res.*, **103**, 20 011–20 022. 6, 68, 77

GRÜN, E., KEMPF, S., KRÜGER, H., LANDGRAF, M. & SRAMA, R. (2001). Dust astronomy: a new approach to the study of interstellar dust. In B. Warmbein, ed., *Proceedings of the Meteoroids 2001 Conference, 6 - 10 August 2001, Kiruna, Sweden*, ESA SP-495, 651–662, ESA Publications Division, Noordwijk. 4, 76

GUILLET, V., JONES, A.P. & PINEAU DES FORÊTS, G. (2009). Shocks in dense clouds. II. Dust destruction and SiO formation in J shocks. *Astron. Astrophys.*, **497**, 145–153. 115

HAMILTON, D. & BURNS, J. (1993). Ejection of dust from jupiter's gossamer ring. *Nature*, **364**, 695–699. 5, 47, 48, 57, 64, 68, 77

HANSEN, C.J., ESPOSITO, L., STEWART, A.I.F., COLWELL, J., HENDRIX, A., PRYOR, W., SHEMANSKY, D. & WEST, R. (2006). Enceladus' Water Vapor Plume. *Science*, **311**, 1422–1425. 22, 96

HILL, M.E., HAMILTON, D.C., GLOECKLER, G., KRIMIGIS, S.M. & MITCHELL, D.G. (2004). Near-Saturn Solar Wind Speeds Determined from MIMI/ CHEMS Measurements of Pickup Ion Spectra at the Cassini Spacecraft. *AGU Fall Meeting Abstracts*, A1412+. 59, 72, 89

HILLIER, J.K., GREEN, S.F., MCBRIDE, N., SCHWANETHAL, J.P., POSTBERG, F., SRAMA, R., KEMPF, S., MORAGAS-KLOSTERMEYER, G., MCDONNELL, J.A.M. & GRÜN, E. (2007). The composition of Saturn's E ring. *Mon. Not. Roy. Astron. Soc.*, **377**, 1588–1596. 8, 26, 49, 79, 109

HORÁNYI, M. (1996). Charged dust dynamics in the solar system. *Annu. Rev. Astrophys.*, **34**, 383–418. 60, 96, 99

HORÁNYI, M. (2000). Dust streams from Jupiter and Saturn. *Phys. of Plasmas*, **7**, 3847–3850. 7, 49, 57, 68, 78, 93

HORÁNYI, M., BURNS, J. & HAMILTON, D. (1992). The dynamics of Saturn's E ring particles. *Icarus*, **97**, 248–259. 76

HORÁNYI, M., MORFILL, G. & GRÜN, E. (1993). Mechanism for the acceleration and ejection of dust grains from Jupiter's magnetosphere. *Nature*, **363**, 144–146. 5, 57, 68, 77

HORÁNYI, M., GRÜN, E. & HECK, A. (1997). Modeling the Galileo dust measurements at Jupiter. *Geophys. Res. Lett.*, **24**, 2175. 77, 95

HORÁNYI, M., JUHÁSZ, A. & MORFILL, G.E. (2008). Large-scale structure of Saturn's E-ring. *Geophys. Res. Lett.*, **35**, 4203. 8, 76, 116

HSU, H., KEMPF, S., BURTON, M., ROY, M., SRAMA, R., MORAGAS-KLOSTERMEYER, G., HELFERT, S. & GRÜN, E. (2008). The stream particle observation during cassini's saturn tour. In *European Planetary Science Congress 2008*, vol. 3. 64

HSU, H., KEMPF, S., JACKMAN, C.M., POSTBERG, F., SRAMA, R., MORAGAS-KLOSTERMEYER, G., HELFERT, S. & GRÜN, E. (2009). Stream particles observation during the Cassini-Huygens flyby of Jupiter. 640. 78

HSU, H., KEMPF, S., POSTBERG, F., SRAMA, R., M., J.C., MORAGAS-KLOSTERMEYER, G., HELFERT, S. & GRÜN, E. (2009a). Interaction of the solar wind and stream particles, results from the cassini dust detector. *AIP conference proceedings; Solar Wind 12*, **In Press**, (in press). 78, 79, 90, 93

HSU, H.W., KEMPF, S. & JACKMAN, C.M. (2009b). Observation of saturnian stream particles in the interplanetary space. *Icarus*, **In Press**. 70, 71, 72, 73, 79, 84, 86, 87, 90, 93

IP, W. (1997). On the Neutral Cloud Distribution in the Saturnian Magnetosphere. *Icarus*, **126**, 42–57. 76

JACKMAN, C.M., ACHILLEOS, N., BUNCE, E.J., COWLEY, S.W.H., DOUGHERTY, M.K., JONES, G.H., MILAN, S.E. & SMITH, E.J. (2004). Interplanetary magnetic field at ˜9 AU during the declining phase of the solar cycle and its implications for Saturn's magnetospheric dynamics. *Journal of Geophysical Research (Space Physics)*, **109**, 11203. 53, 71, 78, 87

REFERENCES

JACKMAN, C.M., ACHILLEOS, N., BUNCE, E.J., COWLEY, S.W.H. & MILAN, S.E. (2005). Structure of the interplanetary magnetic field during the interval spanning the first Cassini fly-through of Saturn's magnetosphere and its implications for Saturn's magnetospheric dynamics. *Advances in Space Research*, **36**, 2120–2126. 53, 78

JACKMAN, C.M., FORSYTH, R.J. & DOUGHERTY, M.K. (2008). The overall configuration of the interplanetary magnetic field upstream of Saturn as revealed by Cassini observations. *Journal of Geophysical Research (Space Physics)*, **113**, 8114. 54, 78

JOHNSON, R.E., FAMÁ, M., LIU, M., BARAGIOLA, R.A., SITTLER, E.C. & SMITH, H.T. (2008). Sputtering of ice grains and icy satellites in Saturn's inner magnetosphere. *Planet. Space Sci.*, **56**, 1238–1243. 16, 33, 76, 95, 117

JONES, G.H., ARRIDGE, C.S., COATES, A.J., LEWIS, G.R., KANANI, S., WELLBROCK, A., YOUNG, D.T., CRARY, F.J., TOKAR, R.L., WILSON, R.J., HILL, T.W., JOHNSON, R.E., MITCHELL, D.G., SCHMIDT, J., KEMPF, S., BECKMANN, U., RUSSELL, C.T., JIA, Y.D., DOUGHERTY, M.K., WAITE, J.H. & MAGEE, B.A. (2009). Fine jet structure of electrically charged grains in Enceladus' plume. *Geophys. Res. Lett.*, **36**, 16204. 79, 95, 108, 116

JURAC, S., JOHNSON, R.E. & RICHARDSON, J.D. (2001). Saturn's E Ring and Production of the Neutral Torus. *Icarus*, **149**, 384–396. 14, 15, 33, 76, 95, 107, 117

JURAC, S., MCGRATH, M.A., JOHNSON, R.E., RICHARDSON, J.D., VASYLIUNAS, V.M. & EVIATAR, A. (2002). Saturn: Search for a missing water source. *Geophys. Res. Lett.*, **29**, 240000–1. 96

KANAYA, K., ONO, S. & ISHIGAKI, F. (1978). Secondary electron emission from insulators. *Journal of Physics D Applied Physics*, **11**, 2425–2437. 30, 100, 101

KANE, M., MITCHELL, D.G., CARBARY, J.F., KRIMIGIS, S.M. & CRARY, F.J. (2008). Plasma convection in Saturn's outer magnetosphere determined from ions detected by the Cassini INCA experiment. *Geophys. Res. Lett.*, **35**, 4102. 97

KEMPF, S., SRAMA, R., ALTOBELLI, N., AUER, S., TSCHERNJAWSKI, V., BRADLEY, J., BURTON, M., HELFERT, S., JOHNSON, T., KRÜGER, H., MORAGAS-KLOSTERMEYER, G. & GRÜN, E. (2004). Cassini between Earth and asteroid belt: First in-situ charge measurements of interplanetary grains. *Icarus*, **171**, 317–335. 60

KEMPF, S., SRAMA, R., HORÁNYI, M., BURTON, M., HELFERT, S., MORAGAS-KLOSTERMEYER, G., ROY, M. & GRÜN, E. (2005a). High-velocity streams of dust originating from Saturn. *Nature*, **433**, 289–291. 7, 8, 47, 48, 49, 57, 61, 62, 64, 68, 78, 86

KEMPF, S., SRAMA, R., POSTBERG, F., BURTON, M., GREEN, S.F., HELFERT, S., HILLIER, J.K., MCBRIDE, N., MCDONNELL, J.A.M., MORAGAS-KLOSTERMEYER, G.,

ROY, M. & GRÜN, E. (2005b). Composition of saturnian stream particles. *Science*, **307**, 1274–1276. 8, 13, 49, 52, 68, 79, 83, 95, 101, 109, 111, 114, 115

KEMPF, S., BECKMANN, U., SRAMA, R., HORANYI, M., AUER, S. & GRÜN, E. (2006). The electrostatic potential of E ring particles. *Planet. Space Sci.*, **54**, 999–1006. 26, 95, 96, 97, 99, 100

KRÜGER, H., GEISSLER, P., HORÁNYI, M., GRAPS, A., KEMPF, S., SRAMA, R., MORAGAS-KLOSTERMEYER, G., MOISSL, R., JOHNSON, T. & GRÜN, E. (2003). Jovian dust streams: A monitor of io's volcanic plume activity. *Geophys. Res. Let.*, **30**, 3–1. 14, 30, 31, 78

KRÜGER, H., HORÁNYI, M. & GRÜN, E. (2003). Jovian dust streams: Probes of the Io plasma torus. *Geophys. Res. Lett.*, **30**, 020000–1. 48, 68, 69, 73, 77

KRÜGER, H., GRAPS, A.L., HAMILTON, D.P., FLANDES, A., FORSYTH, R.J., HORÁNYI, M. & GRÜN, E. (2006). Ulysses jovian latitude scan of high-velocity dust streams originating from the jovian system. *Planet. Space Sci.*, **54**, 919–931. 48, 62, 64

MARTENS, H.R., REISENFELD, D.B., WILLIAMS, J.D., JOHNSON, R.E. & SMITH, H.T. (2008). Observations of molecular oxygen ions in Saturn's inner magnetosphere. *Geophys. Res. Lett.*, **35**, 20103. 33, 34, 117, 118

MELIN, H., SHEMANSKY, D.E. & LIU, X. (2009). The distribution of atomic hydrogen and oxygen in the magnetosphere of Saturn. *Planet. Space Sci.*, **57**, 1743–1753. 34, 35, 96, 117

MEYER-VERNET, N. (1982). "flip-flop" of electric potential of dust grains in space. *Astron. Astrophys.*, **105**, 98–106. 101

MONCUQUET, M., LECACHEUX, A., MEYER-VERNET, N., CECCONI, B. & KURTH, W.S. (2005). Quasi thermal noise spectroscopy in the inner magnetosphere of Saturn with Cassini/RPWS: Electron temperatures and density. *Geophys. Res. Lett.*, **32**, 20. 97

ORLANDO, T. & SIEGER, M.T. (2003). The role of electron-stimulated production of O2 from water ice in the radiation processing of outer solar system surfaces. *Surface Science*, **528**, 1–7. 34, 118

PERSOON, A.M., GURNETT, D.A., KURTH, W.S. & GROENE, J.B. (2006). A simple scale height model of the electron density in Saturn's plasma disk. *Geophys. Res. Lett.*, **33**, 18106. 97

PERSOON, A.M., GURNETT, D.A., SANTOLIK, O., KURTH, W.S., FADEN, J.B., GROENE, J.B., LEWIS, G.R., COATES, A.J., WILSON, R.J., TOKAR, R.L., WAHLUND, J. & MONCUQUET, M. (2009). A diffusive equilibrium model for the plasma density in Saturn's magnetosphere. *Journal of Geophysical Research (Space Physics)*, **114**, 4211. 97

REFERENCES

PILCHER, C.B., CHAPMAN, C.R., LEBOFSKY, L.A. & KIEFFER, H.H. (1970). Saturu's Rings: Identification of Water Frost. *Science*, **167**, 1372–1373. 8, 79

POSTBERG, F., KEMPF, S., SRAMA, R., GREEN, S.F., HILLIER, J.K., MCBRIDE, N. & GRÜN, E. (2006). Composition of jovian dust stream particles. *Icarus*, **183**, 122–134. 7, 13, 49, 68, 73, 78, 81, 111

POSTBERG, F., KEMPF, S., HILLIER, J.K., SRAMA, R., GREEN, S.F., MCBRIDE, N. & GRÜN, E. (2008). The E-ring in the vicinity of Enceladus II: Signatures of Enceladus in the elemental composition of E-ring particles. *Icarus*, **193**, 438–454. 26, 49, 95, 115

POSTBERG, F., KEMPF, S., ROST, D., STEPHAN, T., SRAMA, R., TRIELOFF, M., MOCKER, A. & GOERLICH, M. (2009a). Discriminating contamination from particle components in spectra of Cassini's dust detector CDA. *Planet. Space Sci.*, **57**, 1359–1374. 8, 82, 109, 111, 112, 114, 115

POSTBERG, F., KEMPF, S., SCHMIDT, J., BRILLIANTOV, N., BEINSEN, A., ABEL, B., BUCK, U. & SRAMA, R. (2009b). Sodium salts in E-ring ice grains from an ocean below the surface of Enceladus. *Nature*, **459**, 1098–1101. 26, 81, 112

ROSENBERG, M. & MENDIS, D.A. (1992). A note on dust grain charging in space plasmas. *J. Geophys. Res.*, **97**, 14773. 100

RYMER, A.M., MAUK, B.H., HILL, T.W., PARANICAS, C., MITCHELL, D.G., COATES, A.J. & YOUNG, D.T. (2008). Electron circulation in Saturn's magnetosphere. *Journal of Geophysical Research (Space Physics)*, **113**, 1201. 76

SCHIPPERS, P., BLANC, M., ANDRÉ, N., DANDOURAS, I., LEWIS, G.R., GILBERT, L.K., PERSOON, A.M., KRUPP, N., GURNETT, D.A., COATES, A.J., KRIMIGIS, S.M., YOUNG, D.T. & DOUGHERTY, M.K. (2008). Multi-instrument analysis of electron populations in Saturn's magnetosphere. *Journal of Geophysical Research (Space Physics)*, **113**, 7208. 97, 99

SHOWALTER, M.R., CUZZI, J.N. & LARSON, S.M. (1991). Structure and particle properties of Saturn's E ring. *Icarus*, **94**, 451–473. 22, 76

SIEGER, M.T., SIMPSON, W.C. & ORLANDO, T.M. (1998). Production of O_2 on icy satellites by electronic excitation of low-temperature water ice. *Nature*, **394**, 554–556. 33, 117

SITTLER, E.C., ANDRE, N., BLANC, M., BURGER, M., JOHNSON, R.E., COATES, A., RYMER, A., REISENFELD, D., THOMSEN, M.F., PERSOON, A., DOUGHERTY, M., SMITH, H.T., BARAGIOLA, R.A., HARTLE, R.E., CHORNAY, D., SHAPPIRIO, M.D., SIMPSON, D., MCCOMAS, D.J. & YOUNG, D.T. (2008). Ion and neutral sources and sinks within Saturn's inner magnetosphere: Cassini results. *Planet. Space Sci.*, **56**, 3–18. 23, 96

SITTLER, E.C., JR., OGILVIE, K.W. & SCUDDER, J.D. (1983). Survey of low-energy plasma electrons in Saturn's magnetosphere - Voyagers 1 and 2. *J. Geophys. Res.*, **88**, 8847–8870. 76

SPAHN, F., KRIVOV, A.V., SREMČEVIĆ, M., SCHWARZ, U. & KURTHS, J. (2003). Stochastic forces in circumplanetary dust dynamics. *Journal of Geophysical Research (Planets)*, **108**, 5021. 117

SRAMA, R., AHRENS, T.J., ALTOBELLI, N., AUER, S., BRADLEY, J.G., BURTON, M., DIKAREV, V.V., ECONOMOU, T., FECHTIG, H., GÖRLICH, M., GRANDE, M., GRAPS, A., GRÜN, E., HAVNES, O., HELFERT, S., HORANYI, M., IGENBERGS, E., JESSBERGER, E.K., JOHNSON, T.V., KEMPF, S., KRIVOV, A.V., KRÜGER, H., MOCKER-AHLREEP, A., MORAGAS-KLOSTERMEYER, G., LAMY, P., LANDGRAF, M., LINKERT, D., LINKERT, G., LURA, F., MCDONNELL, J.A.M., MÖHLMANN, D., MORFILL, G.E., MÜLLER, M., ROY, M., SCHÄFER, G., SCHLOTZHAUER, G., SCHWEHM, G.H., SPAHN, F., STÜBIG, M., SVESTKA, J., TSCHERNJAWSKI, V., TUZZOLINO, A.J., WÄSCH, R. & ZOOK, H.A. (2004). The Cassini Cosmic Dust Analyzer. *Space Science Reviews*, **114**, 465–518. 7, 28, 51, 76

SRAMA, R., KEMPF, S., MORAGAS-KLOSTERMEYER, G., HELFERT, S., AHRENS, T.J., ALTOBELLI, N., AUER, S., BECKMANN, U., BRADLEY, J.G., BURTON, M., DIKAREV, V.V., ECONOMOU, T., FECHTIG, H., GREEN, S.F., GRANDE, M., HAVNES, O., HILLIER, J.K., HORANYI, M., IGENBERGS, E., JESSBERGER, E.K., JOHNSON, T.V., KRÜGER, H., MATT, G., MCBRIDE, N., MOCKER, A., LAMY, P., LINKERT, D., LINKERT, G., LURA, F., MCDONNELL, J.A.M., MÖHLMANN, D., MORFILL, G.E., POSTBERG, F., ROY, M., SCHWEHM, G.H., SPAHN, F., SVESTKA, J., TSCHERNJAWSKI, V., TUZZOLINO, A.J., WÄSCH, R. & GRÜN, E. (2006). In situ dust measurements in the inner Saturnian system. *Planet. Space Sci.*, **54**, 967–987. 26, 34, 76

STERNGLASS, E.J. (1954). *A Experimental Investigation of Electron Back - and Secondary Emission from Solids*. Ph.D. thesis, Cornell University. 101

TIELENS, A.G.G.M., MCKEE, C.F., SEAB, C.G. & HOLLENBACH, D.J. (1994). The physics of grain-grain collisions and gas-grain sputtering in interstellar shocks. *Astrophys. J.*, **431**, 321–340. 16, 115

TOKAR, R.L., WILSON, R.J., JOHNSON, R.E., HENDERSON, M.G., THOMSEN, M.F., COWEE, M.M., SITTLER, E.C., YOUNG, D.T., CRARY, F.J., MCANDREWS, H.J. & SMITH, H.T. (2008). Cassini detection of water-group pick-up ions in the Enceladus torus. *Geophys. Res. Lett.*, **35**, 14202. 97

TSENG, W.L., IP, W.H., JOHNSON, R., CASSIDY, T. & ELROD, M. (2009). The structure and time variability of the ring atmosphere and ionosphere. *Icarus*, **In Press, Corrected Proof**, –. 118

WAHLUND, J., ANDRÉ, M., ERIKSSON, A.I.E., LUNDBERG, M., MOROOKA, M.W., SHAFIQ, M., AVERKAMP, T.F., GURNETT, D.A., HOSPODARSKY, G.B., KURTH, W.S.,

JACOBSEN, K.S., PEDERSEN, A., FARRELL, W., RATYNSKAIA, S. & PISKUNOV, N. (2009). Detection of dusty plasma near the E-ring of Saturn. *Planet. Space Sci.*, **57**, 1795–1806. 96

WHIPPLE, E.C. (1981). Potentials of surfaces in space. *Reports on Progress in Physics*, **44**, 1197–1250. 96

WILSON, R.J., TOKAR, R.L., HENDERSON, M.G., HILL, T.W., THOMSEN, M.F. & PONTIUS, D.H. (2008). Cassini plasma spectrometer thermal ion measurements in Saturn's inner magnetosphere. *Journal of Geophysical Research (Space Physics)*, **113**, 12218. 97

WILSON, R.J., TOKAR, R.L. & HENDERSON, M.G. (2009). Thermal ion flow in Saturn's inner magnetosphere measured by the Cassini plasma spectrometer: A signature of the Enceladus torus? *Geophys. Res. Lett.,* **36**, 23104. 97

YOUNG, D.T., BERTHELIER, J.J., BLANC, M., BURCH, J.L., BOLTON, S., COATES, A.J., CRARY, F.J., GOLDSTEIN, R., GRANDE, M., HILL, T.W., JOHNSON, R.E., BARAGIOLA, R.A., KELHA, V., MCCOMAS, D.J., MURSULA, K., SITTLER, E.C., SVENES, K.R., SZEGÖ, K., TANSKANEN, P., THOMSEN, M.F., BAKSHI, S., BARRACLOUGH, B.L., BEBESI, Z., DELAPP, D., DUNLOP, M.W., GOSLING, J.T., FURMAN, J.D., GILBERT, L.K., GLENN, D., HOLMLUND, C., ILLIANO, J.M., LEWIS, G.R., LINDER, D.R., MAURICE, S., MCANDREWS, H.J., NARHEIM, B.T., PALLIER, E., REISENFELD, D., RYMER, A.M., SMITH, H.T., TOKAR, R.L., VILPPOLA, J. & ZINSMEYER, C. (2005). Composition and Dynamics of Plasma in Saturn's Magnetosphere. *Science*, **307**, 1262–1266. 97

ZOOK, H., GRÜN, E., BAGUHL, M., HAMILTON, D., LINKERT, G., LIOU, J.C., FORSYTH, R. & PHILLIPS, J. (1996). Solar wind magnetic field bending of jovian dust trajectories. *Science*, **274**, 1501–1503. 4, 5, 9, 47, 48, 67, 77, 78, 87, 90